学位論文

Fluid distribution along the Nankai-trough megathrust fault off the Kii Peninsula inferred from receiver function analysis; from seismogenic to transition zones

（レシーバ関数から推定される
紀伊半島沖南海トラフ巨大地震断層近傍の流体分布
―巨大地震発生域からゆっくり滑り域まで―）

平成 27 年 12 月　博士（理学）申請

東京大学大学院理学系研究科

地球惑星科学専攻

悪原　岳

Abstract

Exploring fluid distribution around megathrust faults on subducting oceanic plates is intriguing because fluid is considered to reduce the strength of megathrust faults to cause various types of fault slip including regular earthquakes. To date, many studies have revealed hydrous state of the subducting oceanic crust beneath onshore region by conducting receiver function (RF) analysis; the method has high sensitivity to the contrast of the elastic properties, especially to S-wave velocity. However, the RF analysis has rarely been applied to data recorded by ocean-bottom seismometers (OBSs).

The difficulty of RF analysis using OBS data is attributed to P-wave multiple reflections within the sea water column, or water reverberations, which appear prominently on vertical component records. That is because the water reverberations alter vertical component records from source wavelets. We developed a method to remove the water reverberations from OBS vertical component records, where we treated water reverberations as a frequency filter, i.e., a water-layer filter (WLF). By assuming vertical incidence of P-wave, we can describe the WLF with only two parameters, reflection coefficient on the sea floor and two-way traveltime within the water layer. We determined these parameters by non-linear inversion analysis, making use of the advantages of OBS array.

We created RF image of subsurface structure around the Kii Peninsula at the southwestern Japan, by applying the above WLF method to OBSs and ordinary method to on-land permanent stations. Resultant image elucidated the 3-D geometry of the subducting Philippine Sea plate, where the top of subducting plate and the oceanic Moho exhibit negative and positive RF peaks, respectively. The negative RF peaks along the plate interface extended to seaward, suggesting the existence of low-velocity zone (LVZ) even beneath the offshore region.

We found that the magnitudes of RF amplitudes along the oceanic Moho and the plate interface gradually decrease beneath the Kii Peninsula as the slab subducts deeper. We interpret this amplitude reduction was caused by two factors related to the metamorphic phase changes of the oceanic crust: (1) the velocity increase of the oceanic crust and (2) fracturing of the oceanic crust due to densification which allow fluid to escape from the oceanic crust. According to this interpretation, non-volcanic tremors beneath the Kii Peninsula are characterized by permeable plate interface. This feature contrasts to long-term slow slip events, which are believed to occur along sealed plate interface.

RF amplitudes at offshore region show significant along-strike variation, which may be associated with the subduction of the Kinan Seamount chain. However, in the case of OBS data with low-frequency band, P-to-S conversion phases may be contaminated by sediment reverberations, which makes interpretation of RF amplitudes difficult. In addition, thickness of the LVZ would not be evaluated correctly by the above imaging method due to the simplistic reference velocity model. To investigate more detailed feature of the LVZ located at the top of the plate interface, we conducted RF inversion including high frequency content using several OBSs with good data quality. We first estimated structures of the sediment layer beneath the seafloor by stacking analysis and then constrained deeper structure by performing waveform inversion analysis. As a result, we revealed the existence of a thin LVZ (~2-3 km thick) at the depth of the plate interface. We interpret this as a fluid-rich layer. The LVZ we identified is located at seismogenic zone depth, but its location is complimentary to the strong patch that experienced large seismic slip during the 1946 Nankai earthquake. We consider that excess pore fluid pressure on the megathrust fault prohibited further coseismic slip to occur.

Our inversion analysis on RFs provides well-constrained thickness and velocities around the plate interface, which we could not obtain form the results of the imaging

method. Although the number of sites where we conducted the inversion analysis is limited so far, further expanding the analysis to the other stations in our future work would reveal the spatial variation of the velocities and thickness of the LVZ. This, in turn, will lead to better understanding of the fluid distribution and its influence on future megathrust earthquakes.

Contents

Abstract i

Contents v

1. General Introduction 1

1.1. Introduction 1

1.2. Tectonic setting of study area 8

1.3. Data 12

1.3.1. Seismic stations 12

1.3.2. Event records 13

2. Inverse Water-layer Filter Method 17

2.1. Definition of water-layer filter (WLF) 17

2.2. Synthetic test 23

2.2.1. Method 23

2.2.2. Results and discussion 24

3. Application of Inverse Water-layer Filter Method 33

3.1. Inversion analysis for water-layer filter 33

3.1.1. Overview of inversion analysis 33

3.1.2. Selection criteria of event records 35

3.1.3. Inversion scheme 36

3.1.4. Results and discussions 38

3.2. Quantitative assessment of inverse water-layer filter 48

3.3. Application to receiver function estimation 52

4. Receiver function image of the subducting Philippine Sea plate 55

4.1. Common conversion point stacking 55

4.2. Results 62

4.2.1. 3-D geometry of the subducting Philippine Sea plate 62

4.2.2. Receiver function amplitudes along the subducting plate 64
4.3. Discussion 70
4.3.1. Forward modeling of amplitude reduction beneath the Kii Peninsula 70
4.3.2. Uncertainty estimates for the relative depth of hypocenters to the oceanic Moho 72
4.3.3. Hydrous state of the subducting oceanic crust 73
4.3.4. Permeability difference in source area of long-term slow slip events and tremors 77
5. High-frequency receiver function inversion analysis to reveal fine structure around the plate interface 85
5.1. Receiver function data 86
5.2. Estimation of sediment property by H-κ stacking method 92
5.2.1. Method 92
5.2.2. Results and discussion 93
5.3. Receiver function inversion 100
5.3.1. Model parameters 100
5.3.2. Inversion scheme 102
5.3.3. Results 102
5.4. Discussion 111
5.4.1. How does inversion analysis constrain parameters of low-velocity zone? 111
5.4.2. Possible interpretations of low-velocity zone 112
6. General Discussion 119
6.1. Variation in low-velocity zone thickness along-dip direction 110
6.2. Along-strike variation of fluid distribution 123
6.3. Suggestions for future studies 126
7. Conclusion 129
Acknowledgment 131

Appendix A. Error estimation for receiver function stacking 133
References 135

1. General Introduction

1.1. Introduction

Subduction zones are characterized by the occurrence of megathrust earthquakes that occasionally left tens of thousands of fatalities by strong ground motion and tsunami. Megathrust earthquakes have wide rupture area on the megathrust faults, but the spatial extent in the along-dip direction is limited to the region of high seismic coupling. Such area is often defined as seismogenic zone, typically ranging from 10 to 40 km depth, although its updip limit is still controversial. Aseismic slip occurs on the plate interface at deeper depths with almost no mechanical coupling between the subducting and overriding plates. The middle part between the seismogenic and aseismic zones is known as transition zone, where various types of slow earthquakes, including non-volcanic tremors, low-frequency earthquakes (LFEs), and slow slip events (SSEs), occur.

Subduction zones also play a role in the transportation of water into the Earth's deep interior. Fluid is released from the subducting plates during the subduction via compaction and metamorphic dehydration of incoming material [e.g., *Peacock and Wang*, 1999; *Saffer and Tobin*, 2011]. It is considered that some of the fluid is trapped along the plate interface, reducing fault strength [*Scholz*, 1998] and causing non-volcanic tremors [e.g., *Shelly et al.*, 2006; *Fagereng and Diener*, 2011] and slow slip events (SSEs) [e.g., *Kodaira et al.*, 2004; *Song et al.*, 2009; *Kato et al.*, 2010]. Such fluid might control even the rupture zone of megathrust earthquakes [e.g., *Zhao et al.*, 2011; *Kimura et al.*, 2012]. However, the detailed fluid distribution along the megathrust and its relationship to interplate slips remain unclear.

To date, a number of seismological studies have directed their efforts to reveal physical properties of subducting plates using both active and passive seismic sources.

These studies have detected low-velocity zones (LVZ) and/or high-reflectivity zones along subducting plate boundaries of many subduction zones around the world (Table 1.1). Both LVZ and high-reflectivity zone are often considered as the evidence of abundant fluid along the plate interface. That is because fluid reduces seismic velocities compared with surrounding rocks and yields strong impedance contrast leading to intense reflection phases. One of the prominent contributions to this interpretation has been brought by *Audet et al.* [2009], who investigated the LVZ property beneath the northern Cascadia subduction zone using teleseismic scattered waves. Their estimation of anomalously high Poisson's ratio (~0.4) for the LVZ strongly suggests that the LVZ reflects overpressured oceanic crust. In addition, waveform modeling study for reflection phases have revealed that highly-reflectivity zones have low velocity to be interpreted as fluid-rich zone [e.g., *Kodaira et al.*, 2002; *Bangs et al.*, 2009; *Li et al.*, 2015]. It should be noted that in both cases of LVZ and reflective zone, the other geophysical observations, such as low resistivity, support this interpretation.

Each of active and passive source explorations has both advantages and disadvantages as a tool for investigating fluid distribution. Active source surveys usually have been performed along straight survey lines with densely-deployed seismic stations. They have elucidated P-wave velocity structure at shallow depths, or seismogenic zones, using P-to-P reflection and/or P refraction phases. The high-frequency content in source wavelets and close separation distance of receivers enable to produce fine-scale (<1 km) image of subsurface structures. Trapped fluid around the plate interface has been reported based on intense P-to-P reflection phases [e.g., *Kodaira et al.*, 2002; *Nedimović et al.*, 2003; *Mochizuki et al.*, 2005; *Bangs et al.*, 2009; *Bell et al.*, 2010; *Li et al.*, 2015]. The drawbacks of the active source surveys are insensitivity to S-wave velocity, poor resolution to deep structure, and difficulty in performing 3-D analysis. Especially, the knowledge of S-wave velocity, or Poisson's ratio, is essential to discussing rock types and fluid content [e.g., *Christensen*, 1984,

1996]. Exceptionally, full-waveform inversion can provide fine S-wave velocity structure [e.g., *Kamei et al.*, 2012], but studies employing such a sophisticated method is very limited in number so far.

On the other hand, passive source surveys have revealed the hydrous state of subducting plates at deeper depths, mostly deeper than the seismogenic zone, through tomographic or receiver function (RF) analyses. A number of tomographic analyses have identified LVZ (for both P- and S-wave velocities) with high Poisson's ratio along subducting plates, which are often interpreted as hydrated oceanic crust [e.g., *Husen and Kissling*, 2001; *Hirose et al.*, 2008; *Tsuji et al.*, 2008; *Reyners and Eberhart-Phillips*, 2009]. In general, however, the spatial resolution of these tomographic analysis is much lower than that of active source surveys because of sparse distribution of seismic stations. Moreover, smoothing constraint incorporated in tomographic analysis causes the underestimation of the magnitudes of velocity anomalies [*Song and Helmberger*, 2007]. These drawbacks make it somewhat difficult to evaluate correct thickness and velocity of the LVZ.

RF studies have also identified LVZ by detecting P-to-S conversion phases at both sides of the LVZ [e.g., *Kawakatsu and Watada*, 2007; *Audet et al.*, 2009; *Kim et al.*, 2010; *Hansen et al.*, 2012; *Abe et al.*, 2013]. In principle, RF analysis has potential to achieve finer spatial and vertical resolutions than tomographic analysis, although many RF analyses may fail to estimate correct LVZ thickness due to simplistic velocity models used in time-to-depth conversion of RFs as pointed out by *Bostock* [2013]. The RF amplitudes of P-to-S conversion phases provide information about S-wave velocity In addition, P-wave velocity and density can be constrained by employing reflection phases as analysis targets. In spite of these promising features, RF analysis have been rarely applied to shallow subduction zones so far mainly because of the lack of offshore observations and difficulties in analyzing offshore data.

As we have seen above, previous active and passive source surveys have different

features in terms of the main target depth, sensitivity, and spatial resolution. These differences prohibit making a unified or seamless interpretation about fluid distribution from seismogenic to transition zones. One way to fill up the gap is conducting RF analysis using OBS data. In this thesis, we first aim to develop a RF method applicable to ocean-bottom seismometers (OBSs) and demonstrate the possibility of RF analysis with even complicated OBS data. The other aim of this thesis is to investigate fluid distribution along the Nankai-trough megathrust fault off the Kii Peninsula, southwestern Japan, and to discuss its relationship to slip behavior on the megathrust fault.

A problem specific to OBS records is the presence of the seawater. In general, a RF is estimated by deconvolving a horizontal component record with its source wavelet, which is usually approximated by its vertical component record. This approximation, however, is unsatisfactory for OBS data because strong water reverberations appear on the vertical component records (Figure 1.1). In Chapter 2, we introduce water-layer filter (WLF) method, in which we take a series of reverberations in the water column as a linear filter. With its inverse filter, we can therefore eliminate water reverberations. In Chapter 3, we apply this method to observed data to demonstrate the efficiency of our method and also introduce a method to estimate parameters required by the WLF.

In Chapter 4, we investigate subduction zone structure and its hydrous state beneath the onshore and offshore regions around the Kii Peninsula, southwestern Japan. We perform common-convergence point stacking method to create RF image of subsurface structure. From the image, we first estimate the 3-D geometry of the subducting Philippine Sea (PHS) plate and then estimate fluid content along the subducting plate. Although this method cannot evaluate accurate thickness of the LVZ, we can still obtain useful information from RF amplitudes to acquire intuitive understanding of fluid distribution along the subducting plate. We make interpretation of dehydration process of the subducting oceanic crust based on RF amplitudes,

seismicity, and a previous tomography model.

Chapter 5 aims to quantitatively assess the detailed feature of LVZ beneath the offshore region around the Kii Peninsula. For the purpose, we calculate RFs using higher-frequency range (< 4.0 Hz). We first evaluate the properties of the sediment layer beneath the seafloor by a simple stacking method and then investigate deeper structure by performing RF inversion analysis. Our results shows that the LVZ forms an extremely thin layer, which probably reflects trapped fluid along the plate interface.

In Chapter 6, we briefly provide general discussion derived from this thesis. First, we roughly estimated the spatial variation in LVZ thickness and speculate the dehydration process and fluid distribution along the subducting plate from seismogenic to transition zones. Then we discuss the spatial relationship between fluid distribution and rupture propagation of the 1946 Nankai megathrust earthquake. Finally, we compare what we learn from our study with that from other subduction zones and discuss what future studies of subduction zones should be to better understand relationship between fluid distribution and slip behavior on megathrust faults.

Table 1.1. Low-velocity and highly-reflectivity zones along the subducting plates.

Region	Thickness (km)	Vp (km/s)	Vs (km/s)	Depth (km)	Key observation	Reference
SW Japan	-	3	-	15-30	Reflection phase of active source	*Kodaira et al.* [2002]
	-	-	-	20-35	Reflection phase of active source	*Kurashimo et al.* [2013]
	1-2	-	-	<8	Reflection phase of active source	*Bangs et al.* [2009]
NE Japan	0.1-0.4	<4	-	10-20	Reflection phase of active source	[*Mochizuki et al.*, 2005]
	-	-	~-10%	40-90	Receiver function	[*Kawakatsu and Watada*, 2007]
Cascadia	2-4	2.0-3.5 (Vp/Vs)		20-40	Receiver function	*Hansen et al.* [2012]
	<2	-	-	15-20	Reflection phase of active source	*Nedimović et al.* [2003]
	4>	-	-	20-40	Reflection phase of active source	
Mexico	3-5	-	2.0-2.7	20-45	Reflection phase of passive source	*Song et al.* [2009]
Alaska	0.10-0.25	-	-	13-20	Reflection phase of active source	*Li et al.* [2015]
	3-5	-	-	25-55	Reflection phase of active source	
Nazca	-	-	2.5-4.0	50-150	Receiver function	*Kim and Clayton* [2015]
Southern Ecuador	1	2.7	-	5-7	Reflection and refraction phases of active source	[*Calahorrano et al.*, 2008]
Costa Rica	3-5	1.9-2.9 (Vp/Vs)		15-30	Receiver function	[*Audet and Schwartz*, 2013]
SW Japan (this study)	-	-	2.9-4.2	20-35	Receiver function	This study (Chap. 4)
	~2	~3	~2	15-20	Receiver function	This study (Chap. 5)

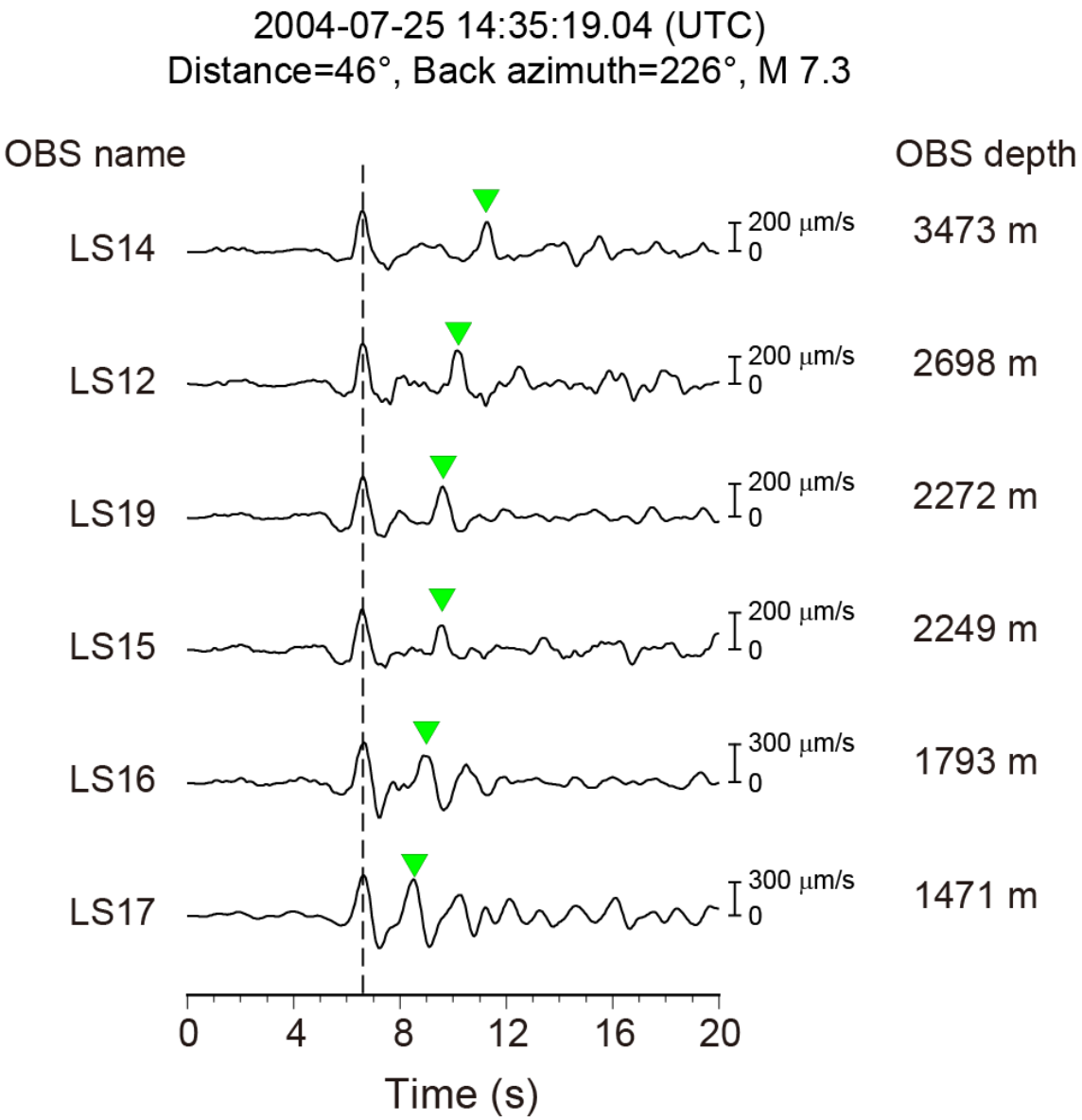

Figure 1.1. Teleseismic waveforms recorded by vertical component sensors of OBSs. Wave forms are aligned with their largest amplitudes (dashed line). Green triangles indicate the expected timings of water reverberations, which were calculated by the twice of OBS depth divided by P-wave velocity in the water layer (1.5 km/s).

1.2. Tectonic setting of study area

Our study area extends from the onshore to offshore regions around the Kii Peninsula and the eastern Shikoku Island, which is located in the central part of southwestern Japan (Figure 1.2). Here the PHS plate subducts along the N55°W direction at a convergence rate of 63–68 mm/yr relative to the Amurian plate along the Nankai Trough [*Miyazaki and Heki*, 2001]. The PHS plate was formed by the back-arc opening of the Sikoku Basin between 27 and 15 Ma [*Okino et al.*, 1999]. For its young age, the temperature of the PHS plate is relatively high in comparison with other subduction zones in the world. Along the fossil spreading axis, the Kinan Seamount chain is located. Its northern part has been already subducted beneath the Kii Channel.

Megathrust earthquakes have occurred on the plate interface in the cycle of 100-150 year beneath southwestern Japan [*Ando*, 1975]. The latest two events were the 1944 Tonankai and 1946 Nankai earthquakes. A number of studies have shown that the rupture area boundary of these two events was located at the southern tip of the Kii Peninsula [e.g., *Baba et al.*, 2002, 2006]. Historical records suggest that some of more previous events are also characterized by almost the same rupture area boundary [*Ando*, 1975]. A number of candidates have been suggested for the cause of the rupture area boundary such as change in the thickness of the oceanic crust [*Mochizuki et al.*, 1998], vertical load from dense rock body embedded in the overriding plate [*Kodaira et al.*, 2006], and lateral variation in pore fluid pressure [*Kurashimo et al.*, 2013]. A subducted seamount (brown area in Figure 1.2) has also been considered to affect the rupture propagation [*Kodaira et al.*, 2000]. More recently, *Murotani et al.* [2015] has revealed complex rupture process of the 1946 Nankai earthquake using abundant observation data, including far- and near-filed seismograms, geodetic leveling, and tide gauges.

Non-volcanic tremors occur on the plate interface beneath southwestern Japan along a belt zone. The focal depths of the tremors are limited, but what controls their

distribution is still controversial (e.g., dehydration location within the oceanic crust, intersection between the subducting plate and the island-arc Moho, etc.). These tremors are considered to be composed of low-frequency earthquakes (LFEs) [e.g., *Shelly et al.*, 2007] and simultaneously occur with short-term SSEs at the same location [e.g., *Obara et al.*, 2004]. A large gap of the tremor belt exists in the Kii Channel, where a recent study has revealed that a long-term SSE occurred from 1996 to 1997 [*Kobayashi*, 2014]. The reason for the tremor gap and the occurrence of the long-term SSE there has not fully understood yet.

Passive seismic monitoring with a large number of OBSs were conducted from November 2004 to November 2007 in this region (circles in Figure 1.2). *Mochizuki et al.* [2010] and *Akuhara et al.* [2013] have revealed along-strike variation of seismicity and seismic velocity structure, respectively, using these OBS data. They have inferred that such heterogeneities may related to the opening history of the Shikoku Basin. Similar along-strike variation has been reported across onshore and offshore regions involved with various kinds of geophysical observations [*Shiomi and Park*, 2008; *Ishise et al.*, 2009; *Ide et al.*, 2010; *Park et al.*, 2014]. Although the cause of the along-strike variation is still open question, these observations invoke the necessity of 3-D analysis for this region.

A number of studies have focused on fluid content along the plate interface in this region, especially for shallow depth near the trench. Borehole experiments operated by Ocean Drilling Program have provided quantitative constraints on properties of décollement (e.g., permeability, and pore fluid pressure). For example, porosity profiles of the boreholes have suggested overpressured décollement at the sites [*Screaton et al.*, 2002]. Furthermore, results of numerical modeling have reported that such an overpressured décollement zone extends from the trench to 40 km landward, corresponding to ~5 km depth beneath the seafloor [*Skarbek and Saffer*, 2009]. The excess pore fluid pressure is considered to be caused by clay dehydration [e.g., *Saffer*

and Tobin, 2011]. A difficulty in these studies based on borehole measurements lies in the sparseness of sampling sites, which hampers investigation into lateral heterogeneities in detail. *Park et al.* [2014] have investigated along-trench variation of décollement reflectivity by conducting active source surveys and inferred that the décollement is segmented along trench into fluid-rich and fluid-poor zones.

In contrast to the shallow part, fluid distribution at the seismogenic zone depth of this region has not been investigated well. One of the exceptional works is *Kodaira et al.* [2002] who has reported the presence of fluid-rich sediment layer along the plate interface off the Shikoku Island based on the intense P-to-P reflection phases. The lateral extent of the fluid-rich interface remains unclear, which is to be a goal of this study. Especially, how fluid distribution is related to complex rupture process of the megathrust earthquake is of interest for academic science the risk assessment of the future megathrust earthquakes.

On the Kii Peninsula, active and passive source surveys with densely aligned seismic stations has been conducted. *Kurashimo et al.* [2013] has identified high reflectivity band and interpreted it as excess pore fluid pressure along the plate interface. *Kato et al.* [2014] has also inferred that the top of subducting plate is hydrated based on the results of tomography analysis. Both studies consider that the fluid originates from the dehydration reaction of the subducting plate.

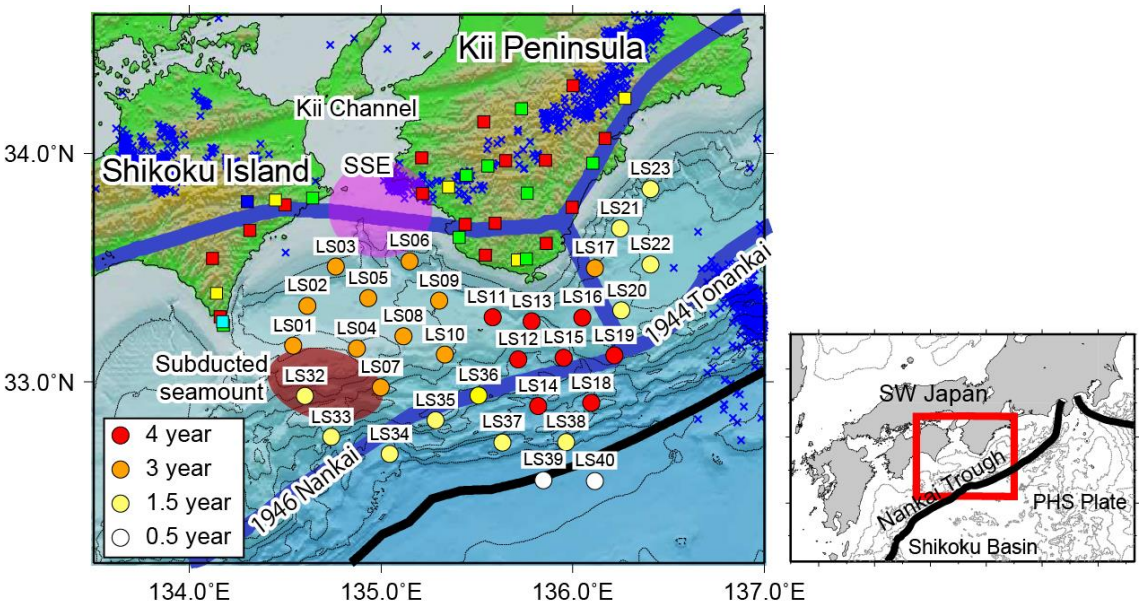

Figure 1.2. Tectonic setting and station distribution of our study area. Circles denote ocean-bottom seismometers (color denotes observational period). Squares are on-land permanent stations operated by the National Research Institute for Earth Science and Disaster Prevention (red), Japan Meteorological Agency (yellow), University of Tokyo (light-green), Kyoto University (blue), and Kochi University (sky-blue). Thick black curve represents the Nankai Trough. Brown and pink shaded areas represent a subducted seamount [Kodaira et al., 2002] and major slip zone of the 1996–1997 slow slip event [Kobayashi, 2014], respectively. Blue crosses show non-volcanic tremors that occurred from January 1, 2004 to December 31, 2004 [Idehara et al., 2014]. Thick blue curves roughly encloses the rupture area of the 1944 Tonankai and 1946 Nankai earthquakes [e.g., Baba et al., 2002, 2006]. The lower-right insert indicates the regional tectonic setting.

1.3. Data

1.3.1. Seismic stations

In this study, we used waveform data obtained by OBSs deployed between Shikoku Island and the Kii Peninsula from November 2003 to November 2007 (circles in Figure 1.2). These OBSs were equipped with three-component velocity sensors with a natural frequency of 1 Hz (Lennartz LE-3Dlite seismometers) and they recorded continuous waveform data. Because their battery capacity was limited to about one year, short-term observations spanning several months to a year were repeated. In total, OBSs were deployed at 32 sites on the seafloor, although the durations of the observational records varied among the sites [*Mochizuki et al.*, 2010]. The close proximity of the OBSs, long observational periods, and large number of observational sites have made this study area one of the best places in the world to demonstrate the potential of RF analysis with OBS data.

When installed, OBSs were released at near the sea surface and sank freely to the seafloor. The direction of vertical component sensor were adjusted automatically by gimbal system, while the direction of two horizontal component sensors remain unknown. We determined the orientations of the horizontal component sensors based on the polarities of Rayleigh waves, using a method similar to that of *Baker and Stevens* [2004]. The averaged and maximum 1σ standard errors of the estimated orientations among all OBSs were 2° and 6°, respectively, which is reasonably small for RF analysis. We determined the sensor orientations for each reinstallation of OBS. Technically, the positions of OBSs (latitude, longitude, and depth) also differ after the reinstallation in order of several hundred meters. We, however, ignored this difference and used averaged positions in this study. We confirmed that the estimated RFs indicate no significant difference due to the reinstallation.

In addition to the OBS data, we also used continuous waveform data obtained at

on-land permanent seismic stations operated by the National Research Institute for Earth Science and Disaster Prevention (Hi-net stations), the Japan Meteorological Agency (JMA), and several universities (squares in Figure 1.2). Although the instrumental responses of these stations differed slightly, their natural frequencies were 1.0 Hz.

1.3.2. Event records

We extracted event records from the continuous waveform data based on two earthquake catalogs: the International Seismological Centre-Global Earthquake Model (ISC-GEM) catalog and the JMA catalog. Referring to the ISC-GEM catalog, we selected 377 teleseismic events of Mw ≥ 6.0 that occurred at distances of 30°–90° from our study area between November 1, 2003 and December 31, 2007. From the JMA catalog, we chose 209 deep local events of Mj ≥ 5.0 that occurred at a depth of > 300 km depth within the distance range of 3°–10° between November 1, 2003 and December 31, 2007. We calculated a synthetic P-wave travel time for each selected event to extract event records, based on the IASP91 Earth structure model [*Kennett and Engdahl*, 1991]. We then rotated these event records to be aligned with the vertical, radial, and transverse coordinates and resampled them at a 20-Hz sampling rate after the application of a 9.0-Hz low-pass filter to avoid aliasing.

Among these preprocessed event records, we selected ones with signal-to-noise ratio (SNR) > 3.0 on vertical components. The SNR was defined by root mean square amplitude ratio calculated with 30 s long time windows before and after the synthetic arrival times. We refer to this criteria as “prerequisite criteria”, hereafter. Throughout this thesis, we further impose additional criterion if necessary. The number of event records satisfying the prerequisite criteria differs among stations. Roughly speaking, the number at on-land stations is as 5-10 times large as that at OBSs (Figure 1.3).

Figure 1.4 shows the frequency-dependent SNR of the event records satisfying

the prerequisite criteria. To produce this figure, we first calculated the Fourier amplitude spectrum of all event records satisfying the prerequisite criteria using 30 s long time windows before and after the theoretical arrival time (the same time windows as described in the last paragraph). We then calculated the Fourier amplitude spectrum ratio of the signal to noise time windows. The consequent frequency-dependent SNR were divided into 50 bins with even interval in logarithmic scale in response to their magnitudes. Finally, we counted the numbers of event records included these bins and presented it in percentage term for each discretized frequency (Figure 1.4). We can see that high SNR is obtained between ~0.5 Hz and ~3.5 Hz for both on-land stations and OBSs.

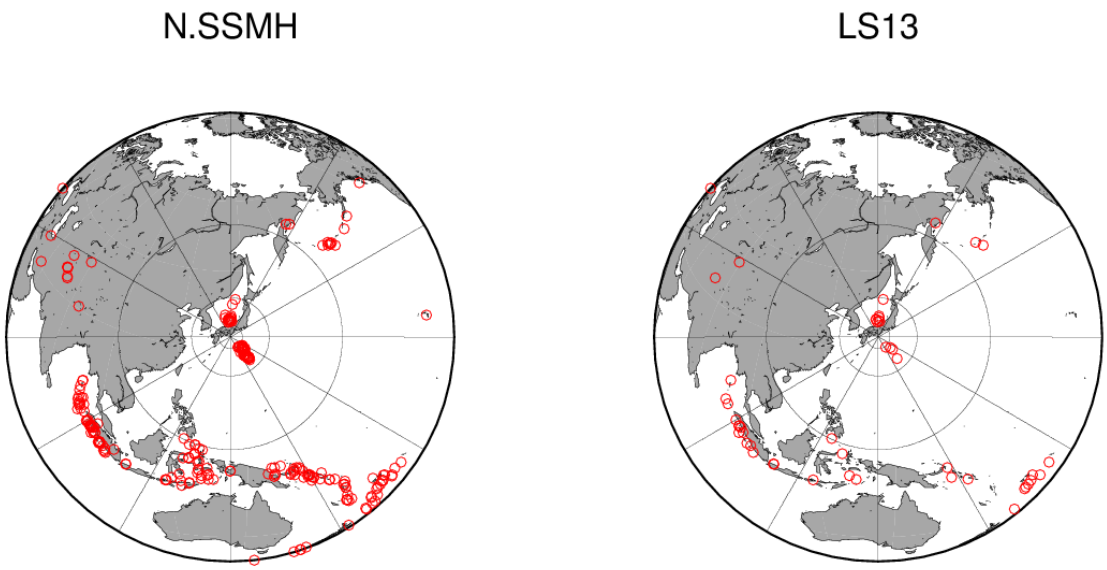

Figure 1.3. Locations of teleseismic and deep events satisfying prerequisite criteria (see Section 1.3.2) for a typical on-land station (left) and an ocean-bottom seismometer (right). Great circles of 3°, 10°, and 30° distance from our study area are depicted.

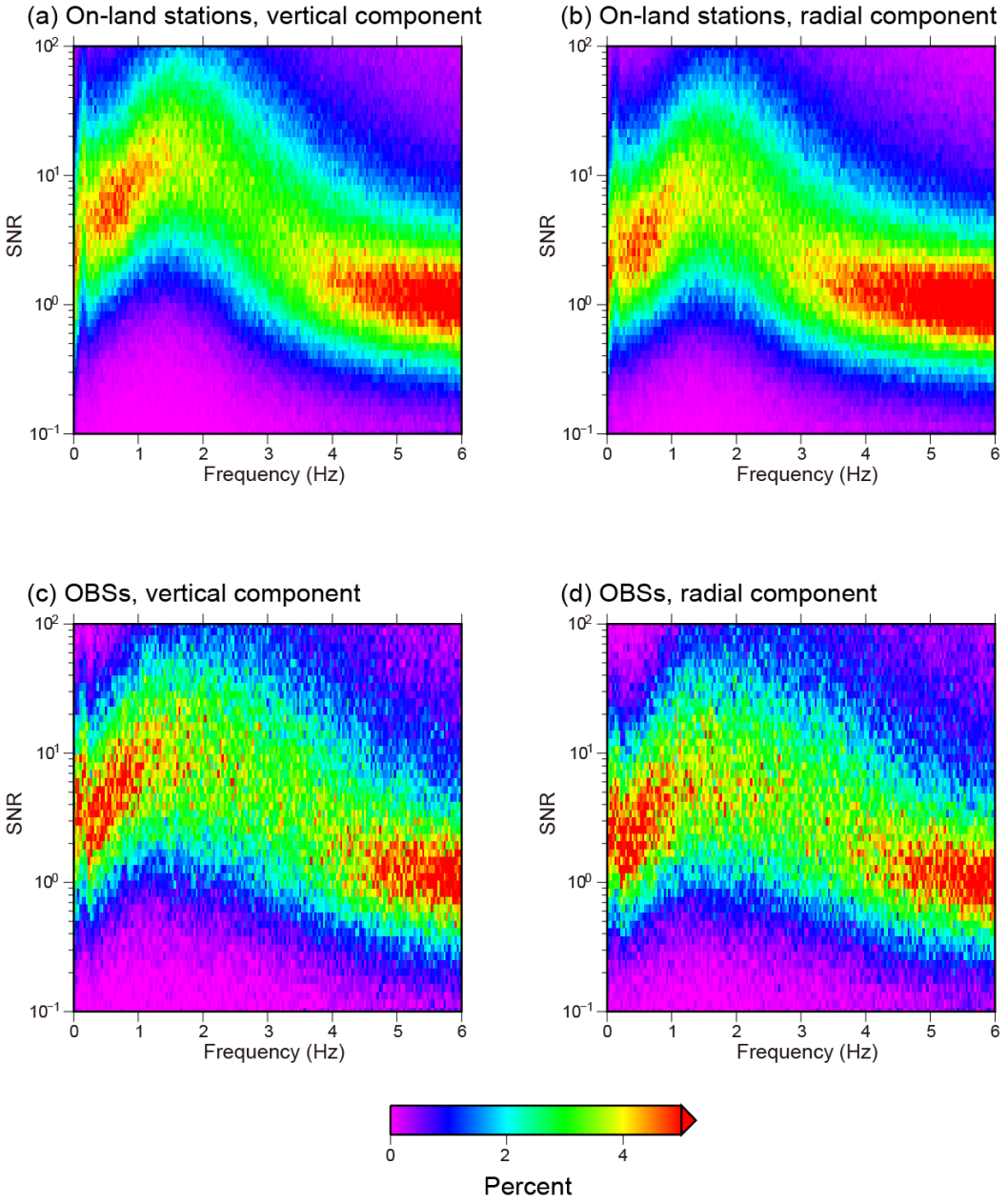

Figure 1.4. Probability density functions of the frequency dependent signal-to-noise ratio (SNR) calculated using all event records from (a, b) on-land stations and (c, d) OBSs of (a, c) vertical and (b, d) radial components. All event records used here satisfy the prerequisite criteria introduced in Section 1.3.2.

2. Inverse Water-layer Filter Method

The seawater column traps seismic waves while they are reflected at both the sea surface and the seafloor; this is referred to as water reverberation. In the case of teleseismic and deep local events, water reverberations strongly affect the vertical component records of the OBSs because these seismic waves propagate vertically to the seafloor as compressional waves in the water layer. Therefore, the waveforms of the vertical component records are altered from their source wavelets. In such a situation, the deconvolution of the horizontal component by the vertical component fails to estimate the RFs correctly.

In this chapter, at first, we propose a method for removing water reverberations from the vertical component records. The key point of our strategy is to treat the water reverberation as a linear filter that acts on the incident wave to the water column from below the sea floor. We refer to this filter as a water-layer filter (WLF). The same concept can be found in marine reflection seismology and to the best of our knowledge, it first appeared in the 1950s [e.g., *Backus*, 1959]. In the latter half of this chapter, we demonstrate how our method can improve RF estimation by conducting synthetic tests.

2.1. Definition of water-layer filter (WLF)

Let us consider an infinite half-space overridden by a water layer with an OBS on the seafloor (Figure 2.1a). If an impulsive plane P-wave with unit amplitude enters the water layer from below, the wave reflects repeatedly on the liquid–solid boundary and at the top of the water layer. In such situation, we may express the OBS vertical component record, $w(t)$, as follows:

$$w(t) = \{(1+R)\cos\theta_P - R_{PSV}\sin\theta_S\}\delta(t) - \sum_{n=1}^{\infty}(-1)^n T(T'\cos\theta_P - T'_{PSV}\sin\theta_S)R^{n-1}\delta(t-n\tau) \quad (1)$$

and

$$\tau = \frac{2h}{c}\sqrt{1-c^2p^2}\,, \quad (2)$$

where R and R_{PSV} represent P-to-P and P-to-SV reflection coefficients, respectively, at the liquid–solid boundary of the seafloor. The upward P-to-P, downward P-to-P, and downward P-to-SV transmission coefficients at the boundary are denoted by T, T', and T'_{PSV}, respectively. Moreover, incident angle of P-wave and reflection angle of S-wave below the seafloor are represented by θ_P and θ_S, respectively. Here we formulated Eq. (1) so that the signs of all reflection and transmission coefficients are positive. The first term on the right-hand side of Eq. (1) corresponds to the direct arrival, including the downward reflection on the seafloor, and the second term denotes the successive nth reverberations. In Eq. (2), τ represents the two-way travel time within the water layer, which is expressed by the wave speed in water, c, water-layer thickness, h, and ray parameter, p. If we assume the ray parameter to be zero, which is equivalent to the case of vertical incidence, we can obtain approximate forms of Eqs. (1) and (2):

$$w(t;\tau,R) = (1+R)\delta(t) - \sum_{n=1}^{\infty}(-1)^n(1-R^2)R^{n-1}\delta(t-n\tau) \quad (3)$$

and

$$\tau = \frac{2h}{c}. \tag{4}$$

Here we employed the following five approximations derived from the assumption of the near vertical incidence: $c^2p^2 \sim 0$, $R_{PSV}\sin\theta_S \sim 0$, $T'_{\mathrm{PSV}}\sin\theta_S \sim 0$, $\cos\theta_P \sim 1$, and $TT' \sim 1 - R^2$. Beneath the actual sea floor, unconsolidated sediment layer with slow seismic velocity allows the incident angle to be almost zero, so these approximations are reasonable. We demonstrated this validity by theoretical calculations based on the Zoeppritz equation, assuming typical physical properties for the sediment (Vp=2.0 km/s, Vs=0.5 km/s, and the density of 1.8 g/cm^3 [*Hamilton*, 1978, 1979]) and water layer (c=1.5 km/s and the density of 1.5 g/cm^3), and the ray parameter (p=0.06 s/km). Table 2.1 shows the resultant theoretical values for the terms included in the above five approximations. It can be seen that the approximations hold well.

Now, we can rewrite Eq. (3) in the frequency domain:

$$W(\omega;\tau,R) = \left(R - \frac{1}{R}\right)\frac{1}{1 + Rexp(-i\omega\tau)} + \frac{1+R}{R}. \tag{5}$$

We define the WLF using Eqs. (3) or (5), which corresponds to a transfer function producing water reverberations. Therefore, the application of the inverse WLF (IWLF), or deconvolution by WLF, eliminates water reverberations. As derived from Eq. (5), the amplitude spectrum of the WLF falls strictly to zero, irrespective of τ and R values, at each constant frequency interval of $1/\tau$ Hz (Figure 2.1c). In practice, these zeros make the deconvolution operation unstable, which requires damping factors such as water-level damping [*e.g., Clayton and Wiggins*, 1976]. Hereafter, in this thesis, the application of IWLF means spectral division by Eq. (5) with water-level damping of 0.05. This damping value was chosen by trial and error, where we visually inspected the deconvolution results from both synthetic (Section 2.2) and real observed data (Section

3.2).

Alternative methods to remove water reverberations have been developed based on the wave field decomposition methods, which decompose observed wave fields into upgoing and downgoing P- and S-wave components [e.g., *Thorwart and Dahm*, 2005; *Bostock and Trehu*, 2012]. Although their early methods require hydro-pressure records as well as displacement data, the recent method proposed by *Bostock and Trehu* [2012] requires only displacement data. Their method enables the treatment of non-zero ray parameters unlike our method, which allows one to tune unknown parameters (e.g., density, seismic velocity and the water depths) so that no acausal energy appears at the beginning of up-going S-wave records. Our method corresponds to the special case of their method with zero ray parameters, though the derivation processes are different. Remarkable advantages of our method are easy implementation and reduced number of unknown parameters: our method demands only a single operation by a filter expressed with two unknown parameters, τ and R.

Table 2.1. Quantitative verification of approximations used in Eqs (3) and (4).

	c^2p^2	$R_{PSV}\sin\theta_S$	$T'_{\mathrm{PSV}}\sin\theta_S$	$1-R^2-TT'$	$\cos\theta_P$
Approximated value	0	0	0	0	1
Theoretical value	8×10^{-3}	2×10^{-3}	1×10^{-3}	2×10^{-2}	0.993

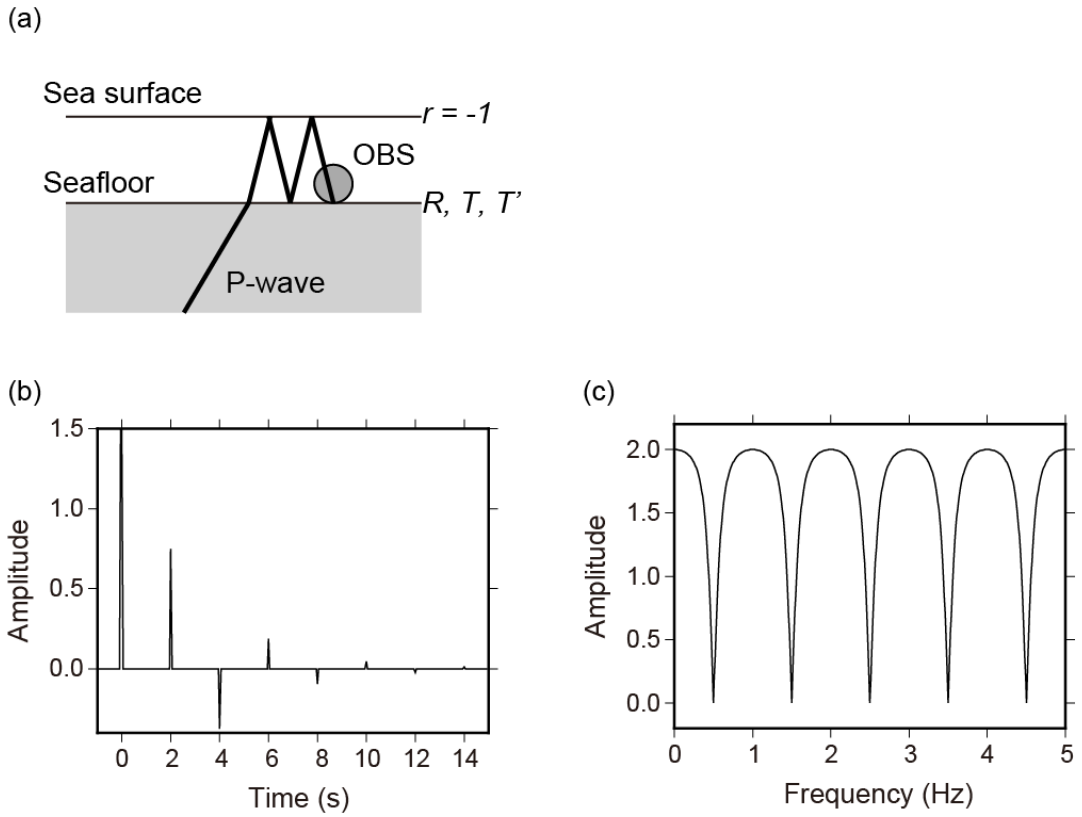

Figure 2.1. (a) Schematic illustration of water reverberations. (b) Time domain representation and (c) amplitude spectrum of water-layer filter (τ=1.0 s and R=0.5).

2.2. Synthetic test

2.2.1. Method

To confirm the efficiency of the WLF method, we conducted synthetic tests with different two 1-D layered models (Table 2.2). The first model, Model A, is composed of water, crust, and mantle layers. The second model, Model B, possesses an additional thin sediment layer beneath the water layer, so is more realistic than Model A. In our synthetic test, at first, both vertical and radial component records were computed by a propagator matrix method [*Haskell*, 1953; *Kumar et al.*, 2011]. We simulated non-vertical incidence with a typical ray parameter of 0.06 s/km. Then, we applied IWLF to the vertical component record to remove water reverberations. Finally, we estimated radial RF by deconvolving the radial component record with the filtered vertical component record. We performed this deconvolution using the extended-time multitaper correlation (ETMTC) method [*Shibutani et al.*, 2008]. Resultant RFs were low-pass filtered to 4.0 Hz, roughly corresponding to the upper limit of frequency range in which we obtained high SNR (Figure 1.4).

For the application of IWLF, we used theoretical τ and R values, which we calculated as follows by assuming vertical incidence:

$$\tau = \frac{2h_1}{\alpha_1}, \tag{6}$$

and

$$R = \frac{\rho_1\alpha_1 - \rho_2\alpha_2}{\rho_1\alpha_1 + \rho_2\alpha_2}. \tag{7}$$

In these equations, α_1, ρ_1, and h_1 represent P-wave velocity, density, and thickness of the water layer, respectively. Similarly, α_2, and ρ_2 represent P-wave velocity and density of the topmost layer beneath the seafloor, respectively. In addition to these theoretical values, we also tested the slightly shifted values to understand how the poorly-constrained parameters influence RF estimation in practical applications. The shift amounts we employed were 0.2 for R and 0.05 s for τ.

2.2.2. Results and discussion

Gray traces in Figure 2.2 show the synthetic vertical component records. In both cases of Model A and B, the first water reverberations appear 2.1 s after the direct P arrivals. The amplitude of this first water reverberation is much larger for Model B than Model A. In Model B, small impedance contrast across the seafloor allows more energy to enter the sea water, making the first water reverberation stronger. The second water reverberation of Model B, which arrives 4.2 s after the direct P phase with negative polarity, is much weaker than the first reverberation. That is because downward wave from water layer passes through, rather than reflected on, the seafloor due to the small impedance contrast.

The waveform of Model B contains a dominant negative arrival around 3 s after the direct P arrival. This phase is first reflected on the sea surface and then on the bottom of the sediment layer. Although this phase has as much potential to distort RFs as water reverberation does, such a phase is less dominant in actual observation data than expected here (see Figure 1.1, where only the first water reverberation seems prominent).

Red traces in Figure 2.2 represent the vertical component records processed with IWLF. Note that they are normalized so that the amplitudes of the direct P arrivals can be equal to those of original waveforms for comparison. We find that water reverberations are successfully removed or, at least effectively suppressed, by the IWLF,

even if we shift τ and R from their theoretical values (Figures 2.2b-c and e-f). We also notice that the application of IWLF produce acausal signals before the P-wave arrival, but these signals are trivial compared with dominant water reverberations on the original waveforms.

Gray and red traces in Figure 2.3 show the synthetic RFs from original and inverse water-layer filtered vertical components, respectively. Note that the RFs processed with IWLF are normalized so that the amplitudes of the direct P arrivals can be equal to those of original RFs. In the case of Model A, the original RF exhibits a positive P-to-S conversion phase from the Moho (Ps_M in Figure 2.4) at 2.5 s after the direct P arrival, and artificial peaks due to water reverberations at 2.1 s and 4.3 s. These artificial peaks are successfully removed or, at least reduced after the application of IWLF.

More drastic improvement can be seen in the case of Model B. The original RF shows many meaningless peaks throughout the records, where 'meaningless' means that the peak cannot be explained from the model. For example, there is no reasonable explanation for positive phase at ~0.6 s and negative phase at ~2.7 s. These artificial peaks are considered to be generated by strong water reverberations on vertical component. The RF processed with IWLF, on the other hand, shows isolated six phases after the direct P arrival. At this stage, we can interpret all the phases as P-to-S conversion phase at the Moho (Ps_M) and the bottom of the sediment layer (Ps), and sediment-related reverberations (PpPs, PpSs, PsSs, and PpPs+w, see Figure 2.4b). We also notice that the filtered RF reproduces impulse response of radial component well (Figure 2.5).

For both models, the artificial peaks on RFs are suppressed even if we employ shifted τ and R values (Figures 2.3b-c and e-f). Determining the thresholds of acceptable shift amount is difficult because it depends on structural model and frequency range of low- or band-pass filter. From our experience, roughly speaking, the

acceptable shift amounts are about 0.1, and 0.3, for τ and R, respectively.

Table 2.2. Two types of layered models used in synthetic tests.

	Layer type	Thickness (km)	Vp (km/s)	Vs (km/s)	Density (g/cm^3)	Ray parameter (s/km)
Model A	Water	1.6	1.5	-	1.0	0.06
	Crust	20.0	6.0	3.5	2.7	
	Mantle	-	8.1	4.7	3.4	
Model B	Water	1.6	1.5	-	1.0	0.06
	Sediment	0.7	1.7	0.4	1.8	
	Crust	20.0	6.0	3.5	2.7	
	Mantle	-	8.1	4.7	3.4	

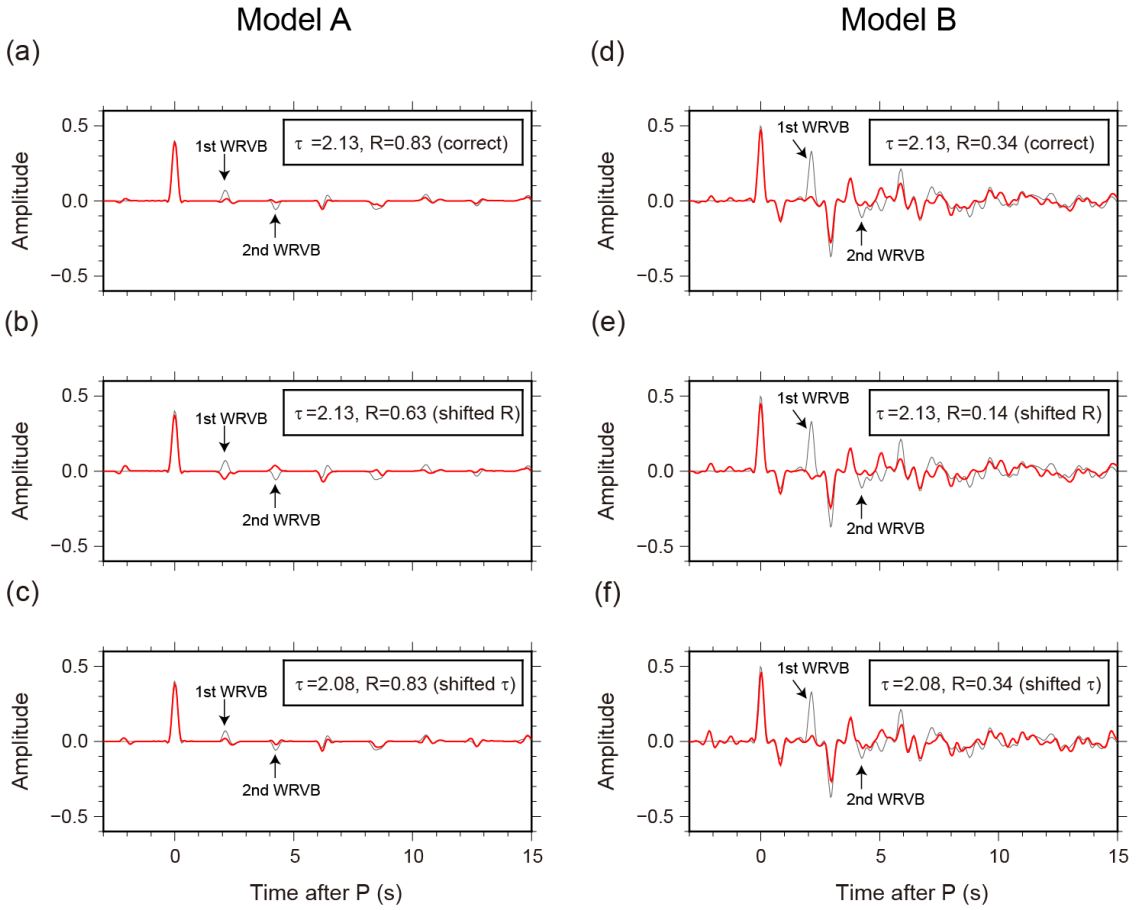

Figure 2.2. Synthetic vertical component records calculated with (a-c) Model A and (d-f) Model B. Gray waveforms represent vertical component records before the application of inverse water-layer filters. Red waveforms are the filtered waveforms with (a, d) the correct parameters, and slightly shifted (b, e) R and (c, f) τ values. All waveforms are low-pass filtered below 4.0 Hz. Note that the amplitudes of the inverse water-layer filtered waveforms are magnified to componsate for the amplitude of downward reflection on the seafloor, which has already removed by inverse water-layer filter. WRVB represents water reverberation.

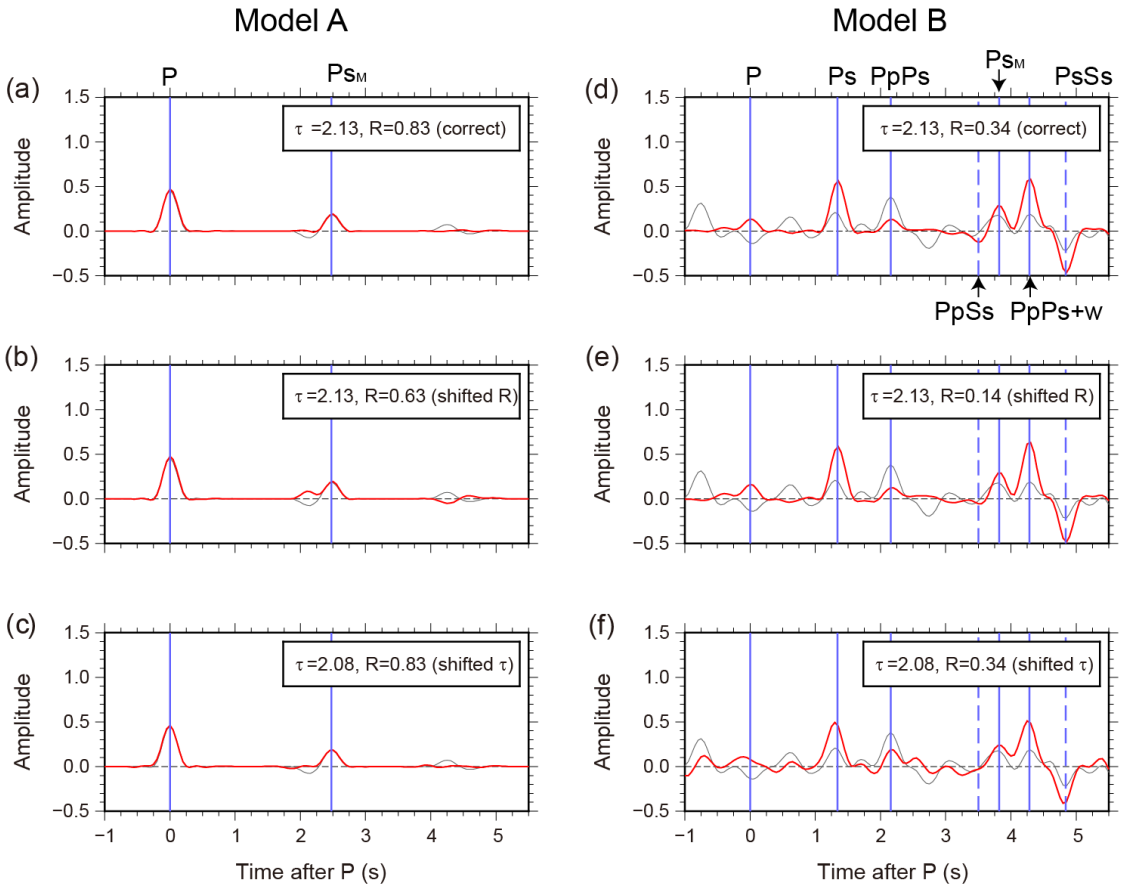

Figure 2.3. Synthetic receiver functions (RFs) calculated with (a-c) Model A and (d-f) Model B. In each panel, red and gray traces are synthetic RFs calculated with and without removal of water reverberations, respectively. Note that the red traces are normalized so that the amplitudes of the direct P arrivals are equal to those of gray traces. The all RFs are low-pass filtered to 4.0 Hz. Solid and dashed blue lines show expected timings of positive and negative phases, respectively. The definition of the phases appearing in this figure are illustrated in Figure 2.4.

(a) Common in Model A and B

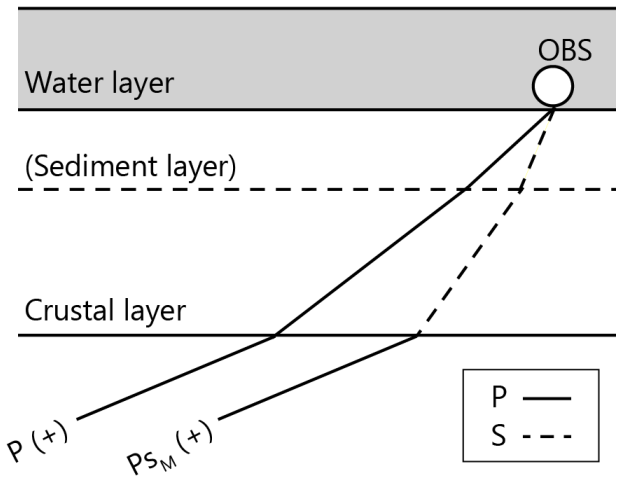

(b) Model B only

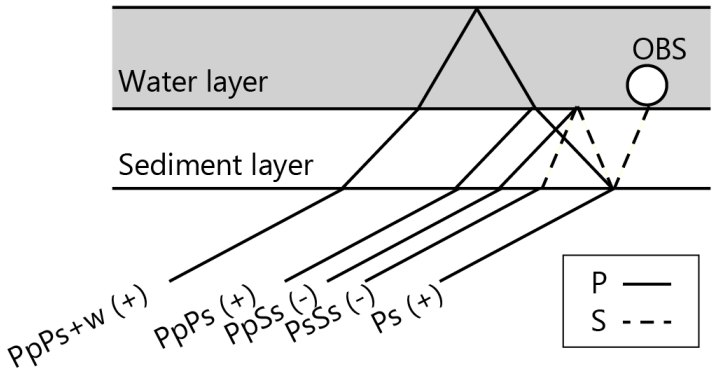

Figure 2.4. Schematic illustration of major phases appearing in synthetic receiver functions (Figure 2.3). The sign following the phase names represent their polarity on radial receiver function.

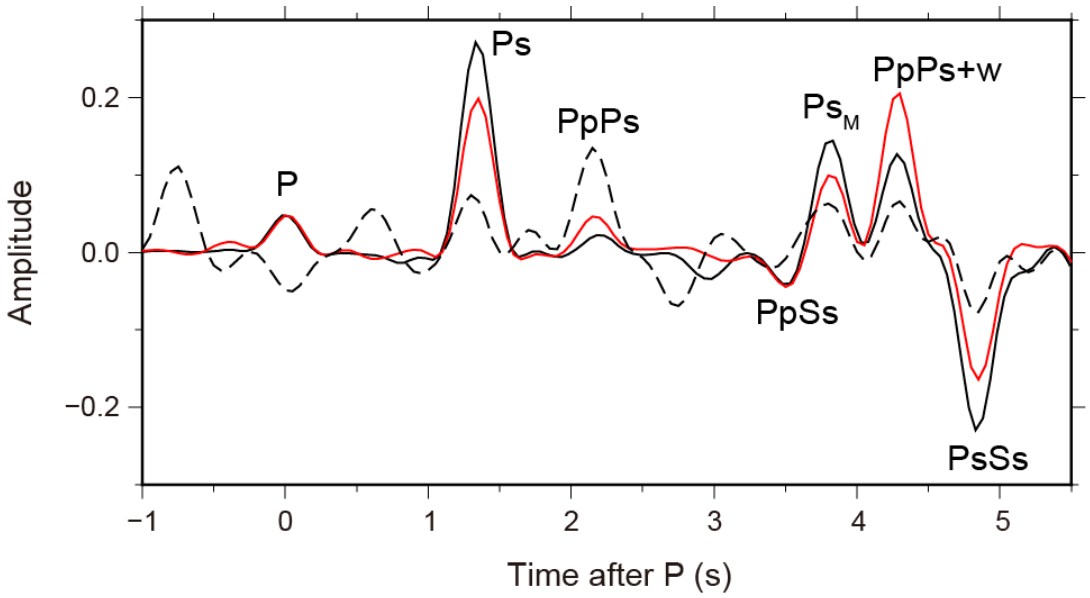

Figure 2.5. Comparison among impulse response of radial component (solid black line), radial RF estimated with the removal of water reverberations (red line), and radial RF estimated by an ordinary method (dashed black line), which all are calculated with the Model B. All waveforms are low-pass filtered to 4.0 Hz. The red trace is normalized so that the amplitude of direct P arrival is equal to that of the solid black line. The dashed black line is also normalized using the same normalization factor.

3. Application of Inverse Water-layer Filter Method

In the previous chapter, we introduced the IWLF method to remove water reverberations and demonstrated its effectiveness in RF estimation with synthetic experiments. In this chapter, we address several tasks for the practical application with real observation data.

The first compulsory task is the determination of IWLF parameters, τ and R, from observed data. Although there should be various ways to achieve this goal, we introduce a method involved with non-linear waveform inversion in Section 3.1. A major advantage of this inversion method is that no additional data is required other than OBS vertical component records.

The second task we should address is evaluating the effectiveness of IWLF method for real data (Section 3.2). Our formulation of WLF depends on some assumptions, the vertical incidence of seismic waves and flat seafloor. We, therefore, must pay careful attention to whether IWLF works well with real data. In the end of this chapter, we briefly show the example of radial RFs estimated with the removal of water reverberations (Section 3.3). Resultant RFs exhibit more distinct phases than those calculated by an ordinary method.

3.1. Inversion analysis for water-layer filter

3.1.1. Overview of inversion analysis

Let us consider a situation where teleseismic P-wave propagates a long distance to a densely-deployed OBS array. In such a case, we can neglect radiation pattern difference among all OBS records. We may express the vertical component records of the ith OBS, $u^i(t)$, as the convolution of a source wavelet, $s(t)$, and the vertical component of the Earth's impulse responses, $G_V^i(t)$, after correcting instrumental respopnse:

$$u^i(t) = s(t) * G_V^i(t). \quad (8)$$

If we further assume that the vertical component of the Earth's impulse response is equal to the response of water layer, namely $w^i(t; \tau^i, R^i)$, we can rewrite Eq. (8) as follows:

$$u^i(t) = s(t) * w^i(t; \tau^i, R^i). \quad (9)$$

.

Separating the two terms in the right-hand side of Eq. (9) from a single event record is difficult in general; there is a tradeoff between estimation of a source wavelet and deciding of the WLF. Fortunately, we can resolve this tradeoff by using multiple OBS records because the source wavelet appears as a common factor among all OBS records. To achieve this separation, we perform a non-linear waveform inversion, where we searches an optimum parameter set using simulated annealing (SA) algorithm [*Kirkpatrick et al.*, 1983]. Such inversion analyses using the SA algorithm has been conducted in order to extract source wavelets and/or relative arrival times [*Chevrot*, 2002; *Iritani et al.*, 2010, 2014; *Tonegawa et al.*, 2013]. The application of the SA method to our case is highly motivated by *Iritani et al.* [2010, 2014], who successfully identified core phases even if their onsets were overlapped by long-tail of the earlier phases. *Tonegawa et al.* [2013] estimated source wavelets using the SA algorithm and computed RFs using the estimated source wavelets. Their method can be an alternative to our IWLF method. We, however, prefer our IWLF method because there is no necessity to estimate source wavelets of all events. This is a distinct average in the case of OBSs, because their relatively noisy data does not allow us to estimate source wavelets of all events successfully.

Our inversion problem includes multiple OBS vertical component records of a

single teleseismic or deep event. Parameters to be estimated are the source wavelet, $s(t)$, arrival times of P-wave, t_p^i, normalization factor, a^i, and the two parameters of WLF, τ^i and R^i. The superscript of these parameters, i, represents indices discriminating OBSs, which we omit if obvious. Now, synthetic waveforms of the ith station, $u_{syn}^i(t)$, can be represented as follows:

$$u_{syn}^i(t) = a^i \cdot s(t) * \delta\left(t_p^i\right) * w\left(t; \tau^i, R^i\right) \tag{10}$$

If we have N_{sta} stations and N_{smp} samples for a source wavelet, then total number of model parameters amounts to $N_{smp} + N_{sta} \times 4$.

3.1.2. Selection criteria of event records

Cycle skipping, due to false determination of t_p by a few multiples of wave period, is one of the major factors which makes the inversion problem unsuccessful. A good strategy to avoid this problem is to make the best guess on t_p initially and limiting the search range of t_p during inversion. For the purpose, we performed automatic phase picking by short-term average to long-term average ratio algorithm [*Abt et al.*, 2010] for the initial estimation of t_p. We briefly introduce the method below.

We first applied band-pass filter of 0.1-2.0 Hz to vertical component of teleseismic or deep event records satisfying the prerequisite condition described in Section 1.3.2 (Figure 3.1a). Then, we calculated envelope functions of them using Hilbert transform (Figure 3.1b). We moved 1-s-long and 4-s-long time windows on the envelope functions to evaluate the signal-to-noise ratio (SNR) function (Figure 3.1c). The SNR function was calculated as RMS amplitude ratio of the 1-s-long to 4-s-long time windows. The moving range was $\pm$10 s around the theoretical P-wave arrival times based on the IASP91 model. Finally, we picked the time point with the maximum SNR value as the initial guess of t_p.

For the following inversion analysis, we selected the band-pass filtered waveforms with the maximum SNR value > 3.0 and extracted waveforms from 3 s before to 10 s after the time picks (t_p).

3.1.3. Inversion scheme

For each event, if the above criteria was satisfied at eight or more OBSs, we performed the waveform inversion. We used the waveforms extracted in the last section as input data, but they were normalized by the maximum amplitude among all OBS records. Our inversion involved 2000 iterations to determine an optimum solution, where single iteration included sample generation, misfit calculation, and evaluation processes as follows.

At each iteration, we randomly generated trial parameters so that they can demand the following conditions:

$$
\begin{gathered}
0.3 \leq a^i \leq 1.0, \\
0.1 \leq R^i \leq 0.7, \\
t_p^{i\prime} - 0.5\ (\mathrm{s}) \leq t_p^i \leq t_p^{i\prime} + 0.5\ (\mathrm{s}), \\
\tau^{i\prime} - 0.25\ (\mathrm{s}) \leq \tau^i \leq \tau^{i\prime} + 0.25\ (\mathrm{s}), \\
\text{and} \\
s_j = s_j{}' \pm 0.01 \\
(i = 1 \cdots N_{sta},\ \ j = 1 \cdots N_{smp}),
\end{gathered}
\tag{11}
$$

where s_j means jth discrete time sample of source wavelets, $s(t)$, and prime notations (such as $t_p^{i\prime}$, $\tau^{i\prime}$, and $s_j{}'$) represent optimum parameters after the previous iteration. At the initial iteration, t_p^i, τ^i, and s_j were fixed to the phase pick time (see Section 3.1.2), the expected value from OBS depth, and zero, respectively. The OBS depths were previously measured by acoustic ranging on installing or recovering OBSs.

We set the source duration to 10 s for all events, which corresponds to N_{smp} = 200 in our case of 20 Hz sampling rate.

Each time generating a trial parameter, we calculated the misfit between observed and synthetic waveforms, m, as the summation of L1-norm difference over all records:

$$m = \sum_{i=1}^{N_{sta}} \sum_{j} \left| u_{syn}^{i}(j\Delta t) - u_{obs}^{i}(j\Delta t) \right|, \tag{12}$$

where u_{obs}^{i} represents observed waveform at ith station, and Δt represents sampling interval. The newly generated parameter was accepted as optimum solution if the misfit value decreases successfully. For t_p and τ, we accepted the trial parameter with a certain probability even if the misfit became larger. This probability was supposed to become smaller as iteration number increases as follows

$$probability = \exp\left(-\frac{m - m'}{T_0 \cdot \gamma^k} \right), \tag{13}$$

where k represent the iteration number, and the prime notations have the same meaning as Eq. (11). In addition, T_0 and γ are tuning parameters of the simulated annealing algorithm referred to as initial temperature and cooling schedule, respectively. We fixed T_0 at three times of the initial misfit value and γ at 0.99 in accordance with *Iritani et al.* [2010].

After 2000 iterations, we evaluated the quality of the final solutions by calculating cross-correlation coefficients (CCs) between synthetic and observed waveforms at each OBS (Figure 3.2), and discarded ill-fit seismograms whose CC was below 0.8. Furthermore, if the inversion failed to produce eight or more seismograms whose CC exceeded 0.8, we discarded all results from the inversion (Figure 3.3).

To confirm the robustness, we repeated this inversion eight times for each event using different random seeds. We then calculated averages and standard deviations of τ and R over these eight inversions. As a results, the standard deviations were below 0.05 s for τ and 0.1 for R for most events (Figure 3.4). These amounts were considerably small compared with the search ranges, suggesting that our inversion was stable. In the following section, we show the averaged τ^i and R^i values of the eight estimations instead of individual results.

3.1.4. Results and discussions

As we can see in Figure 3.2, our inversion produced τ^i values which were mostly consistent with the expected values from OBS depths. Observed waveforms were well reproduced by synthetic waveforms even if the arrival of water reverberations were overlapped by the coda of source wavelet. Figure 3.5 shows the resultant τ and R values estimated from different events at three OBS, LS11, LS12, and LS20. In all cases, individual τ and R values were scattered within ± 0.05 s and ± 0.2, respectively, around their averaged values. If this scattering comes from the dipping seafloor, there should be some correlation between individual τ (or R) values and the locations of the incident point where P-wave enters into the water column. However, we could not find such a correlation (Figures 3.5b and c). We therefore conjectured that the scattered τ and R distributions mainly reflected random errors and decided to use the averaged τ and R values of all events as parameters of IWLFs (i.e., stars in Figure 3.5a).

Next we investigated the correlation between the averaged τ values and the OBS depths. As expected, τ values were consistent with the water depth (Figure 3.6a). In the figure, we also show a reference line that indicates the expectations from OBS depth and constant P-wave velocity of 1.5 km/s in the seawater. We can see the small but significant deviations between the plots of the inversion results and the reference line. Figure 3.6b shows the histogram of such differences. Although the peak is located at the

center, we can see relatively large difference (> 0.15 s) at several OBSs. Our previous synthetic tests (Section 2.2) demonstrated such a large difference in τ values could disable the IWLF method. Thus we conclude estimating τ values only from OBS depths would be problematic in some cases.

Averaged R values for each OBS vary between 0.1 and 0.5, where smaller value represent softer material with small P-wave velocity beneath the seafloor (Figure 3.7). The averaged value of all OBSs is 0.30, which is reasonable for typical sediments (recall the Model B in Section 2.2, possessing a typical sediment layer, exhibits reflection coefficient of 0.34). Weak positive correlation can be seen between reflection coefficients and the OBS depths: smaller R values at shallower depths and larger R values at deeper depths. This tendency may represent some regionality of the sediment properties, but we avoid further interpretation about it in this thesis.

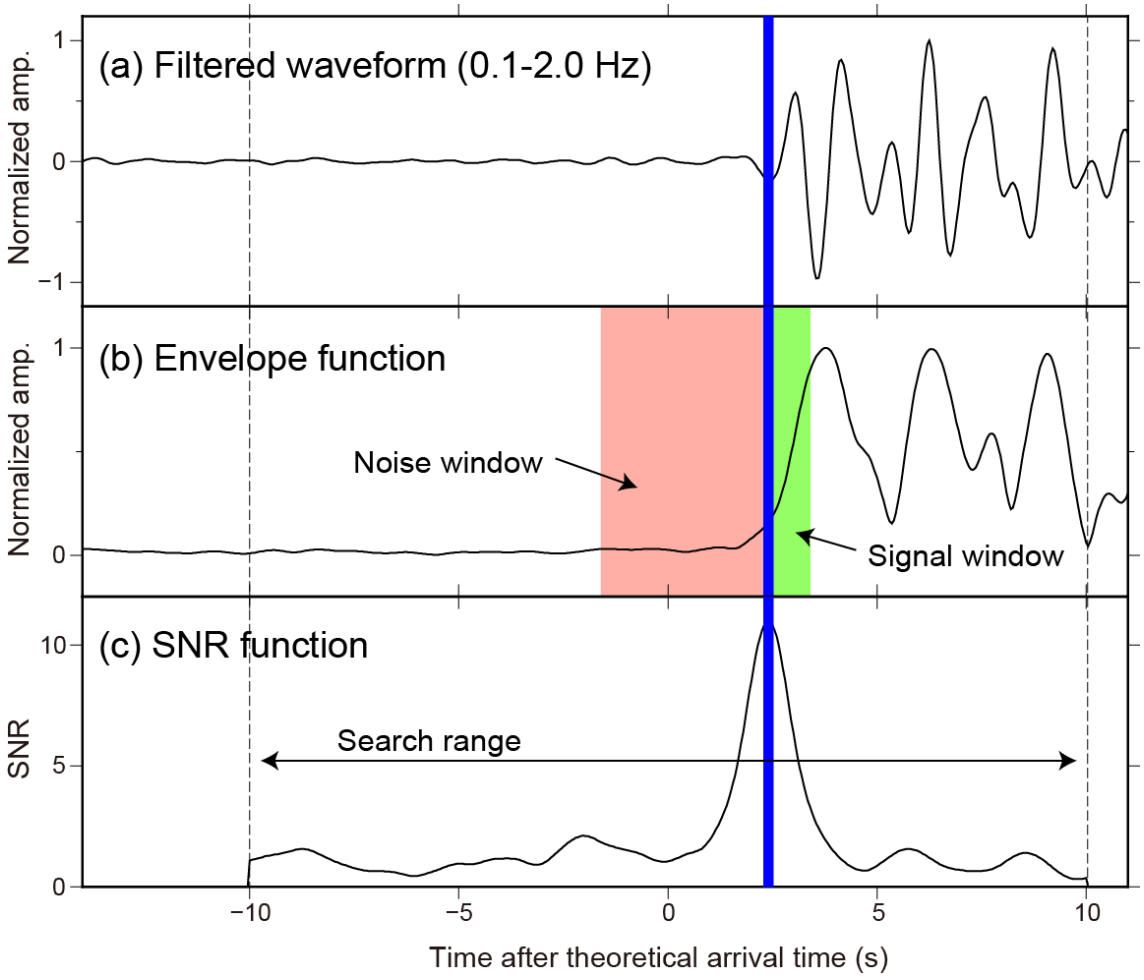

Figure 3.1. Process of automatic arrival time picking. We first (a) applied a band pass filter (0.1-2.0 Hz) to vertical component event record, then (b) calculated envelope function, and finally (c) searched for the maximum of signal-to-noise ratio (SNR) function by moving the time window. The SNR function were computed using the envelope function. Blue vertical bar represents the resultant arrival time pick. Pink and light-green areas denote the time windows for noise and signal, respectively, to compute SNR function.

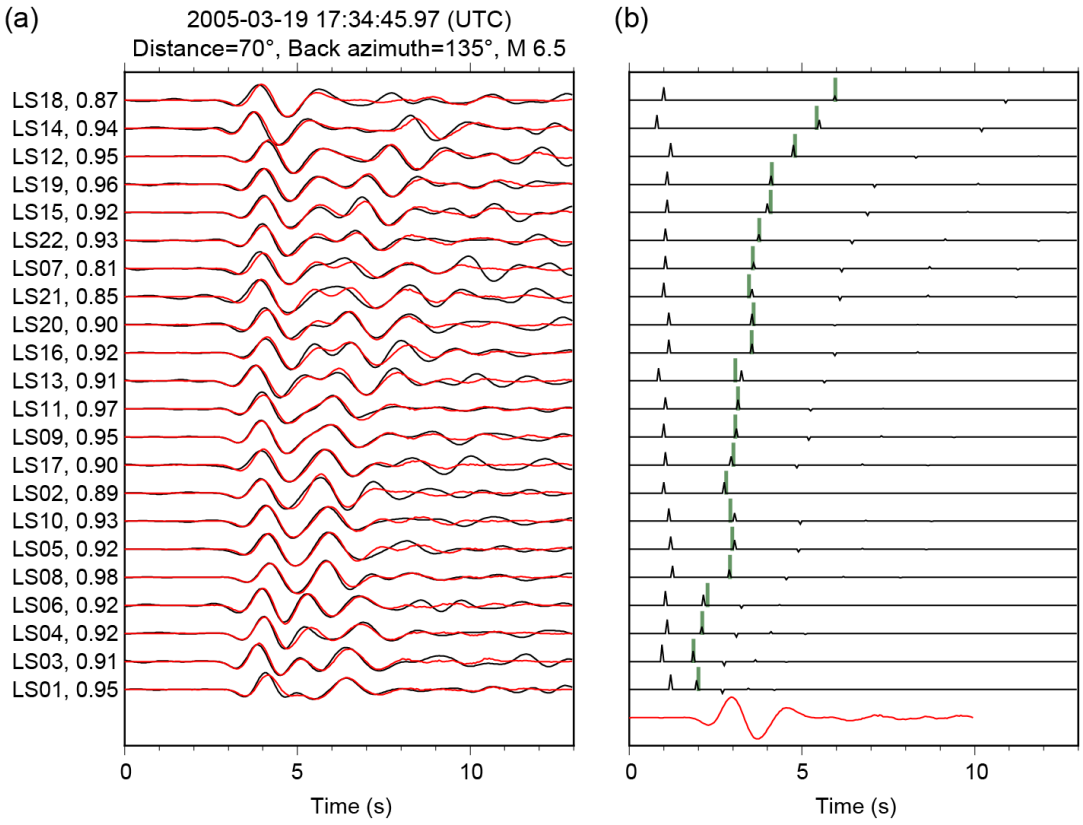
(a)
2005-03-19 17:34:45.97 (UTC)
Distance=70°, Back azimuth=135°, M 6.5
LS18, 0.87
LS14, 0.94
LS12, 0.95
LS19, 0.96
LS15, 0.92
LS22, 0.93
LS07, 0.81
LS21, 0.85
LS20, 0.90
LS16, 0.92
LS13, 0.91
LS11, 0.97
LS09, 0.95
LS17, 0.90
LS02, 0.89
LS10, 0.93
LS05, 0.92
LS08, 0.98
LS06, 0.92
LS04, 0.92
LS03, 0.91
LS01, 0.95
0
5
10
Time (s)
(b)
0
5
10
Time (s)

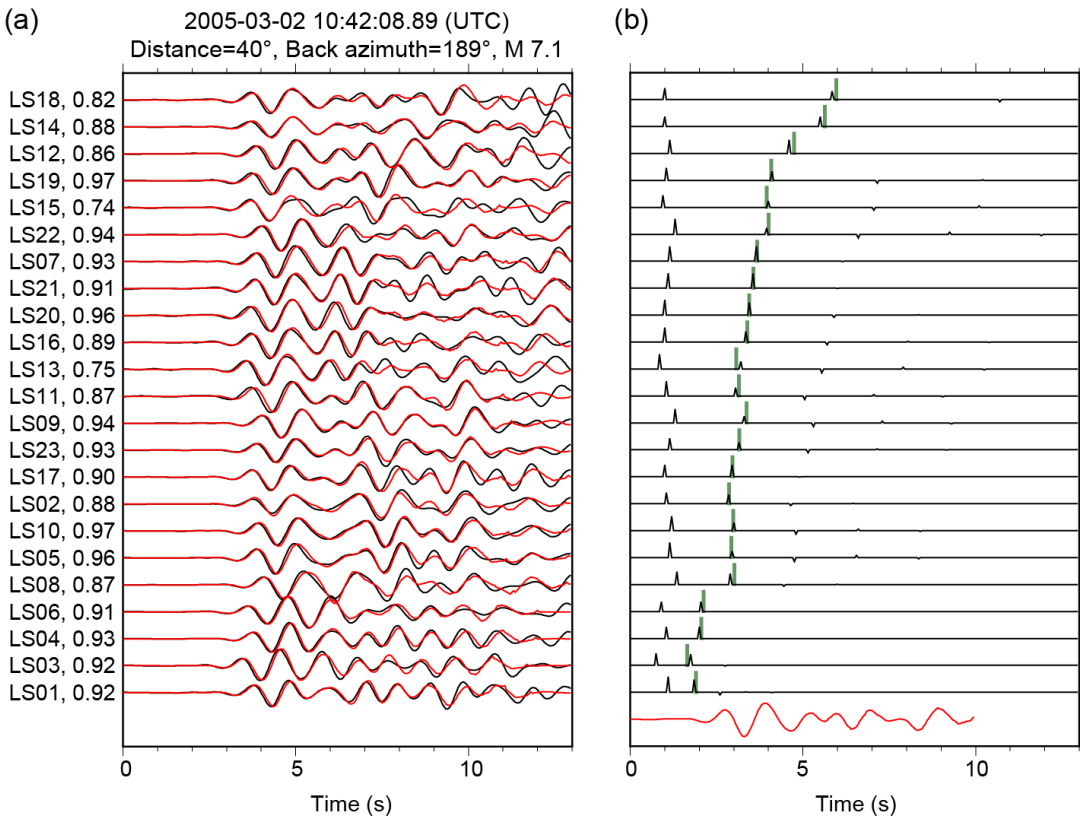
(a)
2005-03-02 10:42:08.89 (UTC)
Distance=40°, Back azimuth=189°, M 7.1
LS18, 0.82
LS14, 0.88
LS12, 0.86
LS19, 0.97
LS15, 0.74
LS22, 0.94
LS07, 0.93
LS21, 0.91
LS20, 0.96
LS16, 0.89
LS13, 0.75
LS11, 0.87
LS09, 0.94
LS23, 0.93
LS17, 0.90
LS02, 0.88
LS10, 0.97
LS05, 0.96
LS08, 0.87
LS06, 0.91
LS04, 0.93
LS03, 0.92
LS01, 0.92
0
5
10
Time (s)
(b)
0
5
10
Time (s)

Figure 3.2. (opposite) Two examples of waveform inversion. (a) Black and red traces show observed and synthetic waveforms, respectively. OBS names and cross-correlation coefficients between the observed and synthetic waveforms are listed on the vertical axis. (b) Red waveform at the bottom shows a source wavelet, $s(t)$, determined by the inversion. Black pulses show WLFs convolved with $a^i \delta\left(t_p^i\right)$ in Eq. (10). Green bars represent the expected timing of the first reverberation inferred from the OBS depths.

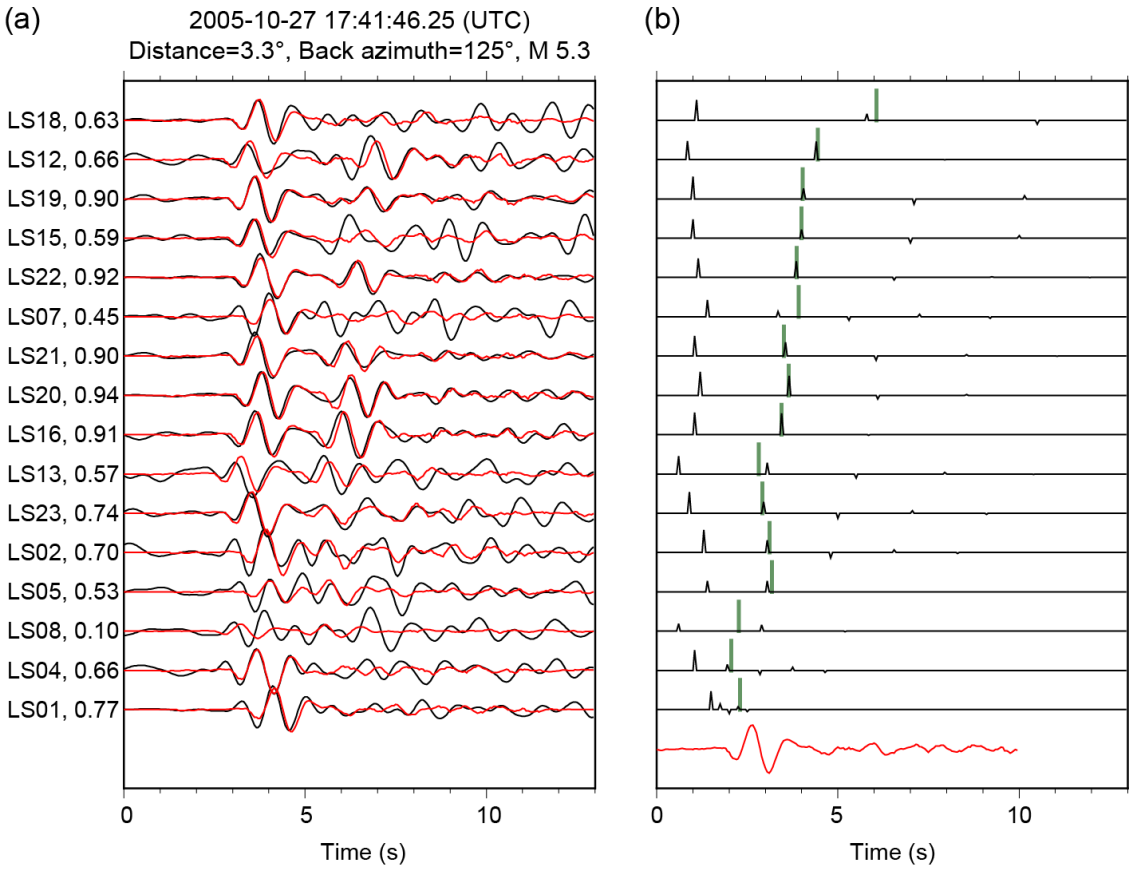

Figure 3.3. An example of waveform inversion showing erroneous results. Note that all results from this inversion were discarded. All notations are the same as Figure 3.2.

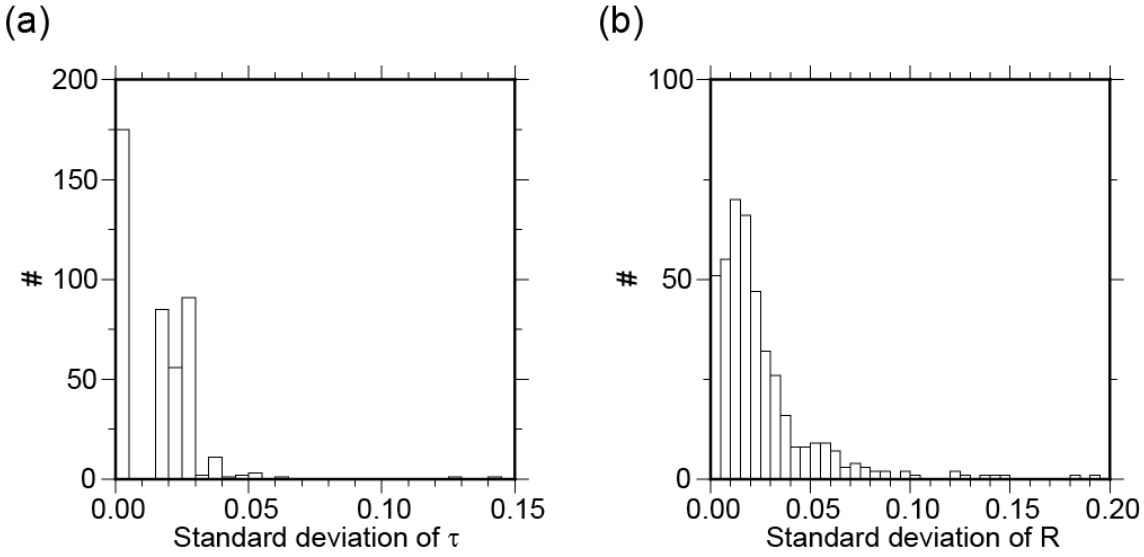

Figure 3.4. Histograms of standard deviation of (a) τ and (b) R over eight inversions using different random seeds.

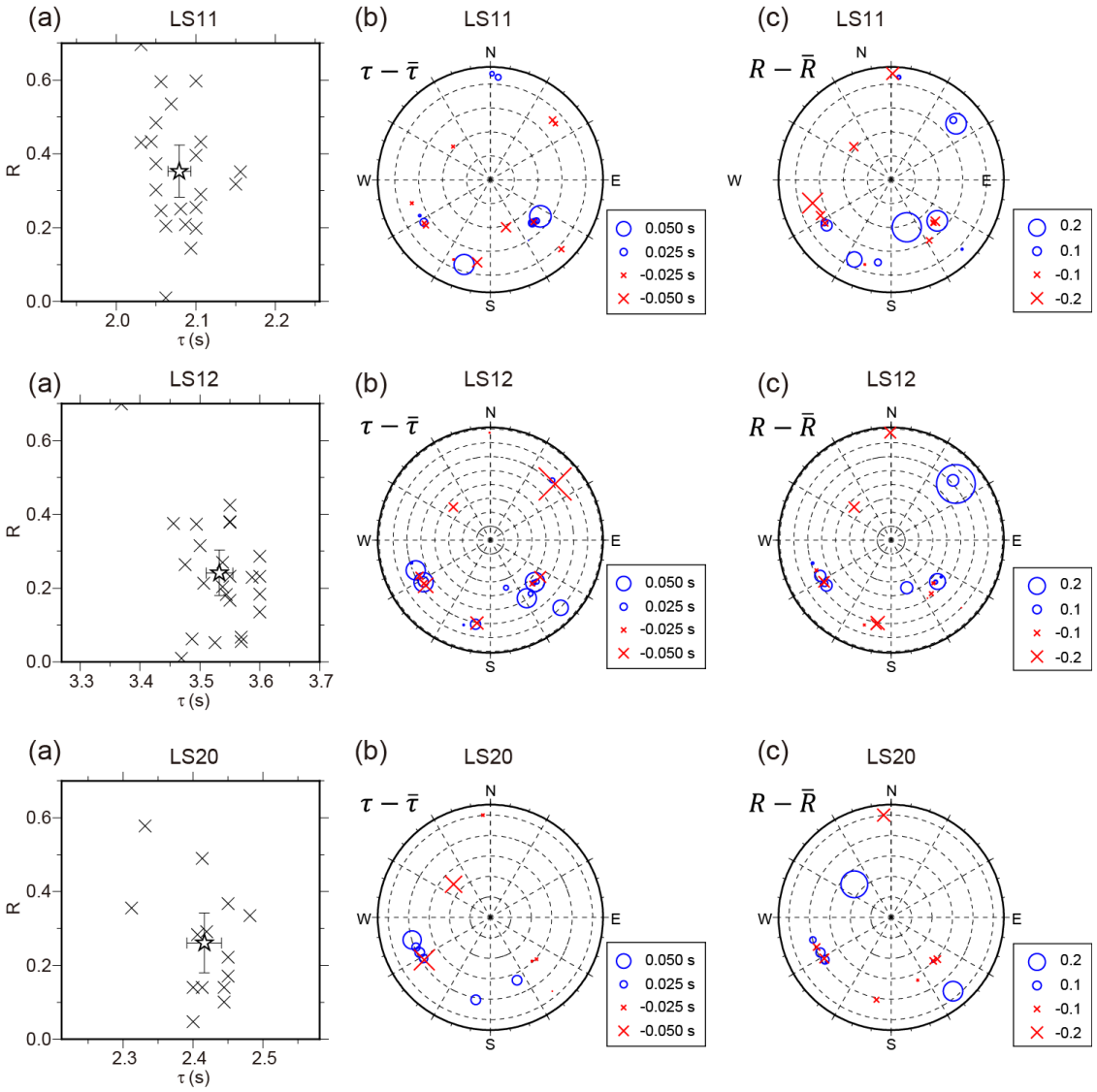

Figure 3.5. Results of waveform inversion for three OBSs, LS11, LS12, and LS20. (a) Crosses represent τ and R values estimated from different events. Stars are their averaged values with 2σ standard errors. (b, c) Deviations of (b) τ and (c) R values from their average values against their back azimuths and horizontal propagation distances of the first water reverberation in the water column. The size of crosses and circles show the amount of the deviations, and their locations represent the incident points of the first water reverberation into the seawater. Center of each polar coordinate is identical to the OBS location, and dashed circles denote intervals of 100 meters.

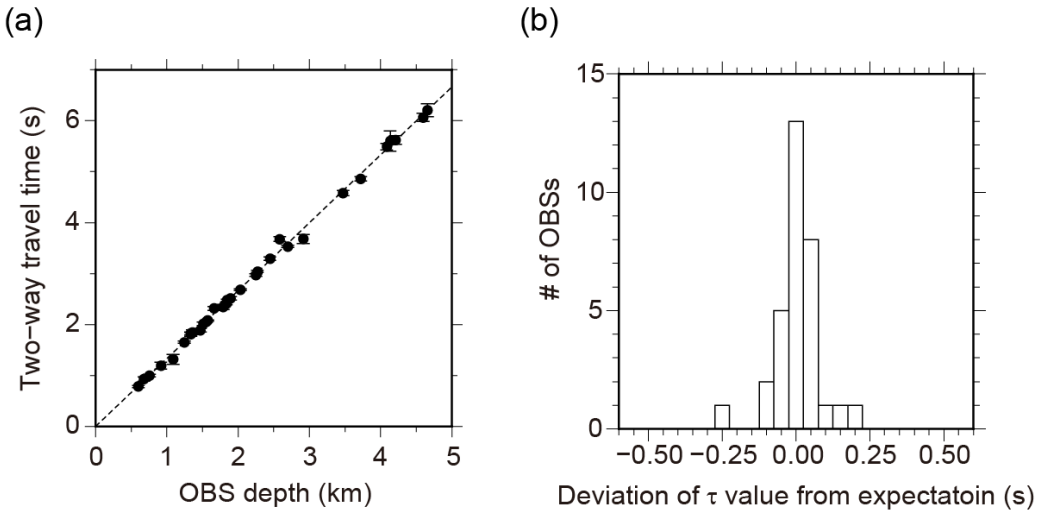

Figure 3.6. (a) Correlation diagram between OBS depth and averaged τ value for each OBS. Error bars denote 2σ confidence region of standard errors. Dashed line represents expected two-way traveltime from OBS depth, where we assumed constant P-wave speed of 1.5 km/s within the water layer and vertical incidence of seismic waves. (b) Histogram of difference amount between an expected τ values from OBS depth and the estimated τ values from the inversion analysis.

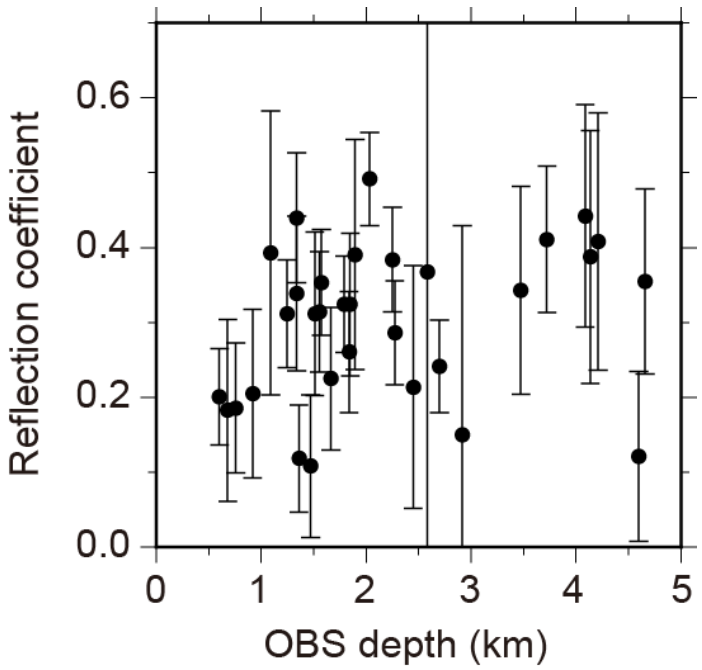

Figure 3.7. Correlation diagram between OBS depth and averaged R value for each OBS. Error bars denote 2σ confidence region of standard errors.

3.2. Quantitative assessment of inverse water-layer filter

Seismograms with a short source duration help us confirm the efficiency of our WLF method, because their water reverberations are clearly separated from the direct P wave arrivals. Figure 3.8 shows an example of such seismograms of OBS vertical component (black curves) compared with those after application of the inverse WLFs (red curves). In these examples, it can be seen that water reverberations are effectively reduced or completely removed. The amplitudes of the direct arrivals are also slightly reduced, which is resultant from the removal of the downward reflection at the sea floor.

In more general cases, water reverberations are contaminated by coda of direct P-wave arrivals, so we cannot check the efficiency of IWLF visually. Nevertheless, we can confirm the effectiveness by inspecting auto-correlation functions (ACFs) of vertical component records. Figure 3.9a shows ACFs of vertical component records at LS11, LS12, and LS20. All event records processed here satisfy the prerequisite criteria described in Section 1.3. Clear and consistent positive peaks appear around 2-4 s, indicating water reverberations (Figure 3.9a). Applying IWLFs, we can successfully suppressed these peaks (Figure 3.9b), suggesting the effectiveness of our method.

To quantify the effectiveness of IWLF for each event records, we measured the difference in root-mean-square amplitude of the ACFs between before and after processing with IWLFs (we refer to this measurements as ΔRMS-ACF, hereafter). Roughly speaking, ΔRMS-ACF tends to be negative for most traces (Figure 3.9c), which we think stems from the reduction of water reverberations. If we use an incorrect τ value which is shifted by 0.15 s from the estimated value, IWLF produces artificial peaks and positive ΔRMS-ACF at a larger number traces (Figure 3.10). Therefore, we decided to use negative ΔRMS-ACF as a criterion to judge whether water reverberations are successfully removed or not in the following analysis. We refer to this criteria as "ΔRMS-ACF criteria", hereafter.

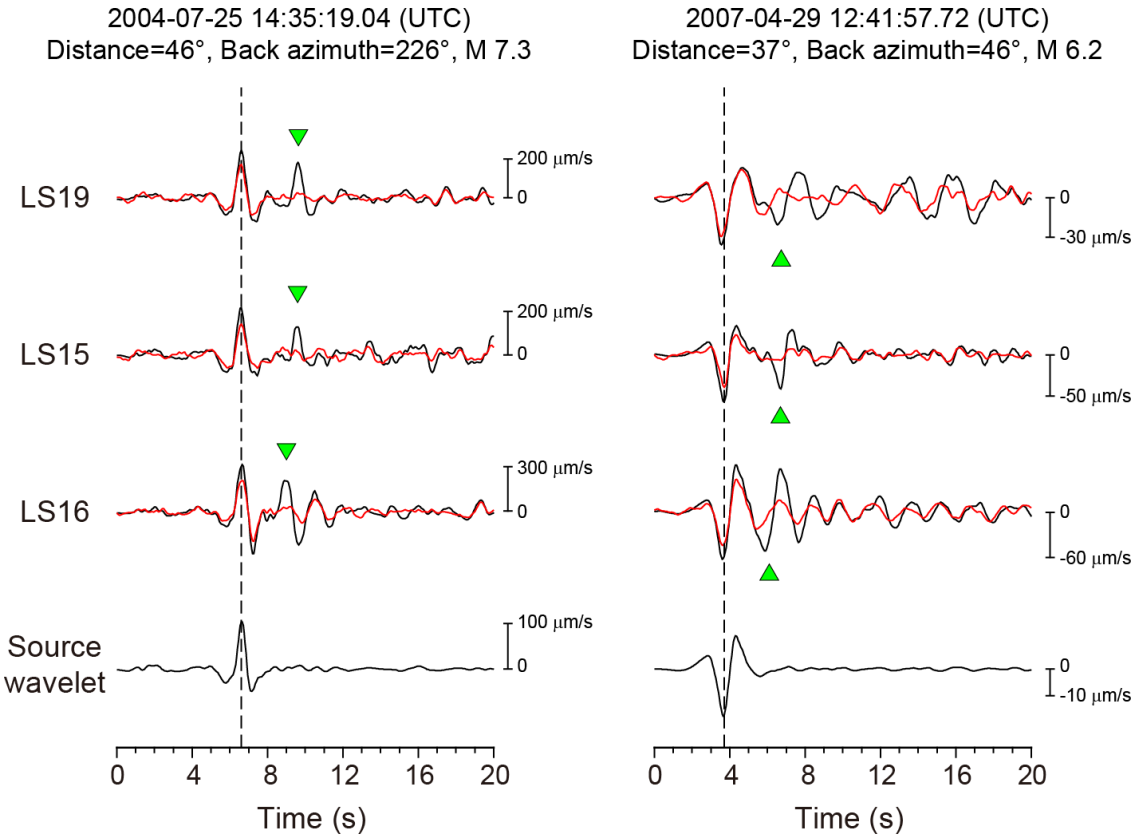

Figure 3.8. Comparisons between original and inverse water-layer filtered seismograms. In the first to third rows, black and red waveforms show original and inverse water-layer filtered ocean-bottom seismometer vertical component records, respectively. Waveforms in the fourth row indicate stacked traces of on-land records, which we regard as source wavelets. Dashed vertical lines denote the arrival times of large amplitudes, which were aligned by the maximum amplitude of the cross-correlation function. Green triangles represent the expected arrival times of the first water reverberations corresponding to the large amplitudes.

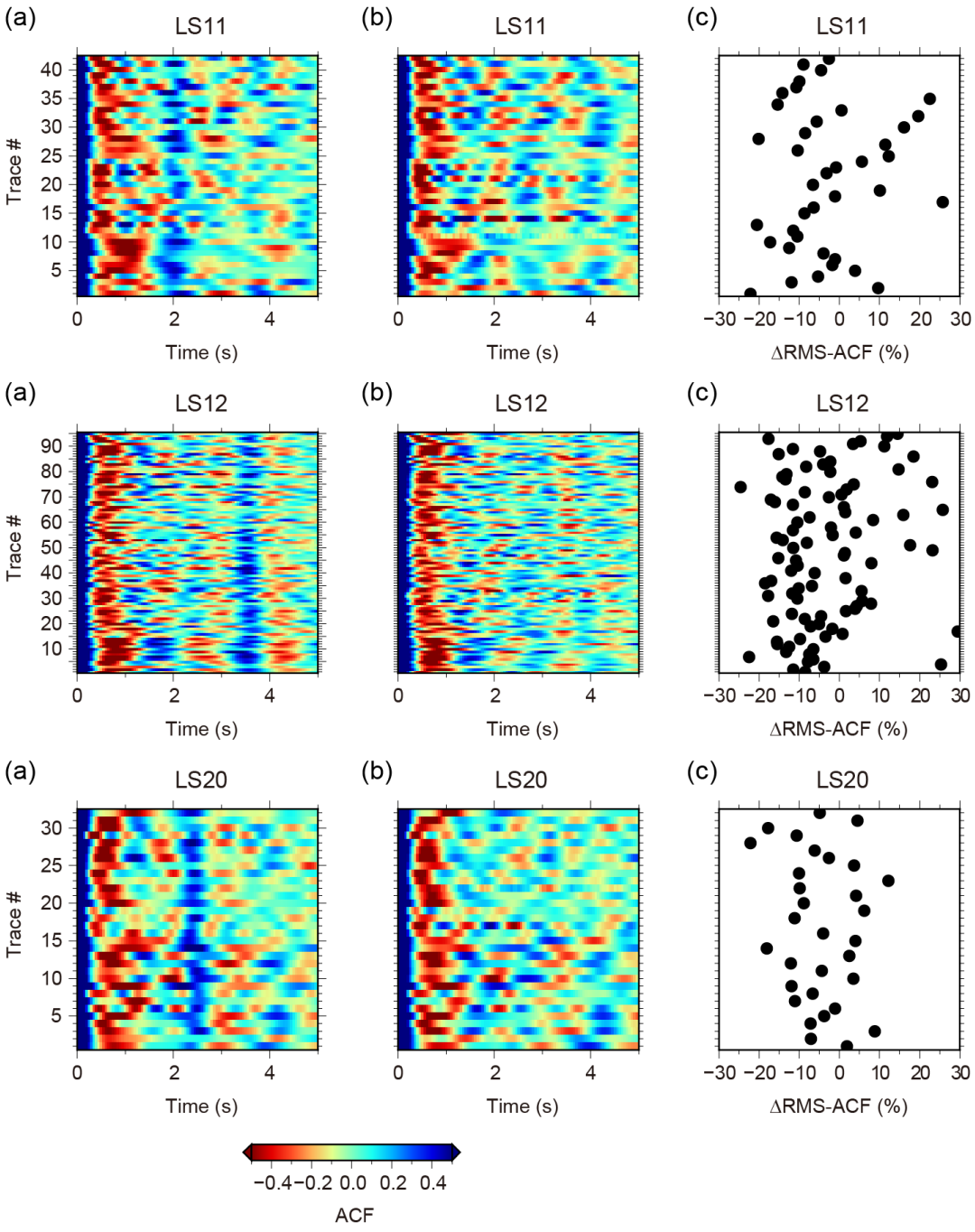

Figure 3.9. Auto-correlation functions of vertical component records (a) before and (b) after the application of inverse water-layer filters. (c) Differences in RMS amplitudes of the auto-correlation functions between before and after the aplication of the inverse water-layer filter (ΔRMS-ACF).

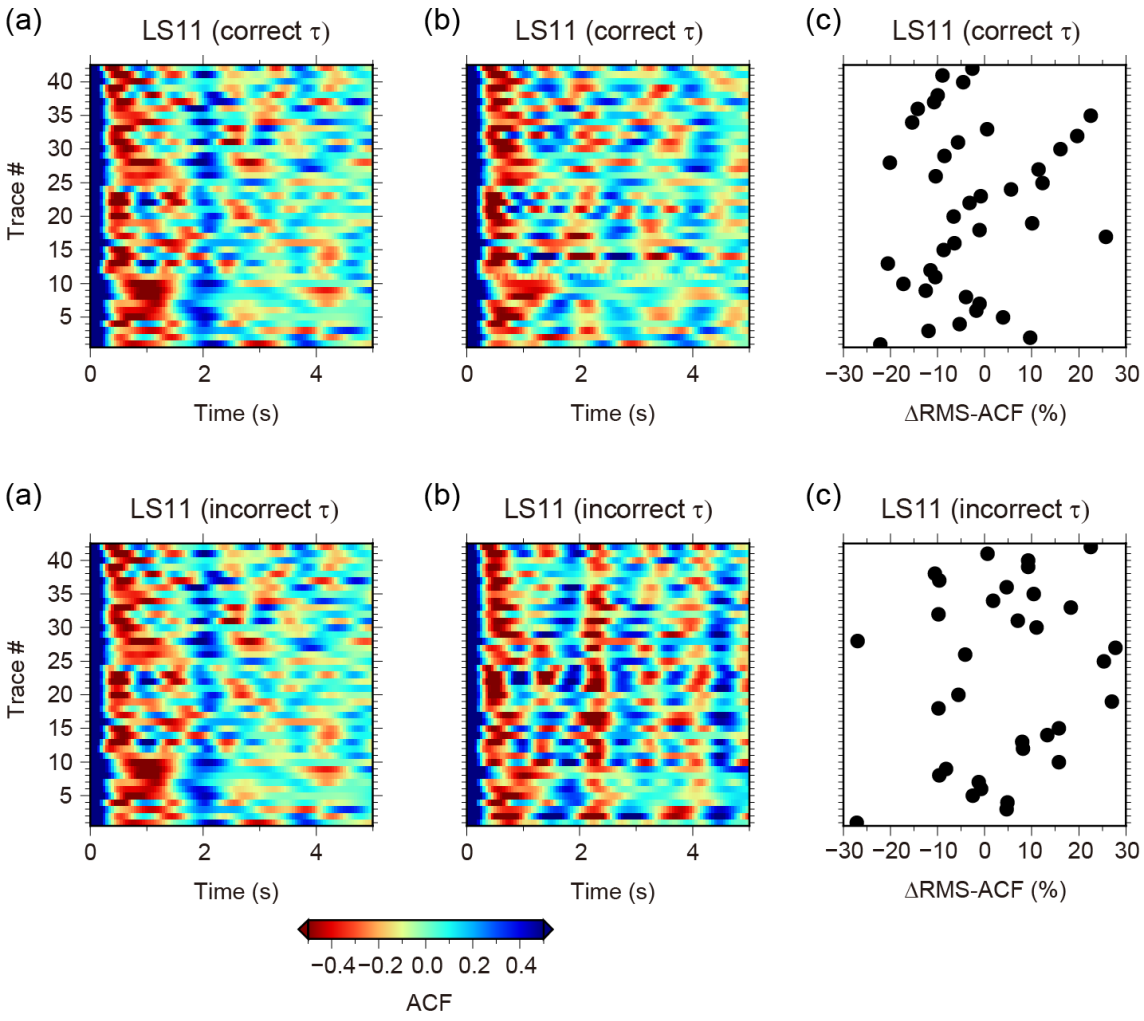

Figure 3.10. The same as Figure 3.9, but in the lower column, we show how inverse water-layer filter using an incorrect τ value affects ACF and ΔRMS-ACF. The upper column indicate the results from the correct τ value.

3.3. Application to receiver function estimation

In Figure 3.11, we show radial RFs calculated at a single OBS station (LS11) by two different methods: the deconvolution of radial component records (1) with original vertical component records (Figure 3.11a) and (2) with vertical component processed with IWLF (Figure 3.11b). In both cases, the ETMTC method was employed to compute the RFs, and the resultant RFs were band-pass filtered between 0.1 and 1.0 Hz. The latter method employs twice deconvolutions: first to remove water reverberations and second to calculate RFs, which seems to make the estimation unstable. Alternative method to avoid the second deconvolution is applying WLF to radial component instead of IWLF to vertical component, but we found that the results did not change significantly after this modified method. Note that we only show RFs whose vertical component records satisfying ΔRMS-ACF criteria (Section 3.2) in Figure 3.11.

Compared with the conventional method, our method produced clearer positive phases at around 4 s on RFs with their back azimuths between 120° and 300° (pale blue arrows in Figure 3.11). We interpreted these enhanced phases as the P-to-S conversion phases from the oceanic Moho of the subducting PHS plate based on a comparison with the tomography model [*Akuhara et al.*, 2013]. In addition, we can identify the P-to-S conversion phases from the top of the PHS plate and the bottom of the sediment layer (pink and gray arrows in Figure 3.11, respectively). The arrivals of the P-to-S conversion phases from the oceanic Moho and the plate interface seem delayed for other back azimuth ranges due to the dipping subducting slab, though the small number of events to the north makes it difficult to identify such moveout with confidence. Unlike usual RFs from on-land station data, RFs from OBS data have less dominant signal at zero delay time corresponding to direct P-wave arrivals. This is because significantly reduced velocity in the unconsolidated sediment beneath the seafloor leads to nearly vertical incidence angle of the incoming P-waves.

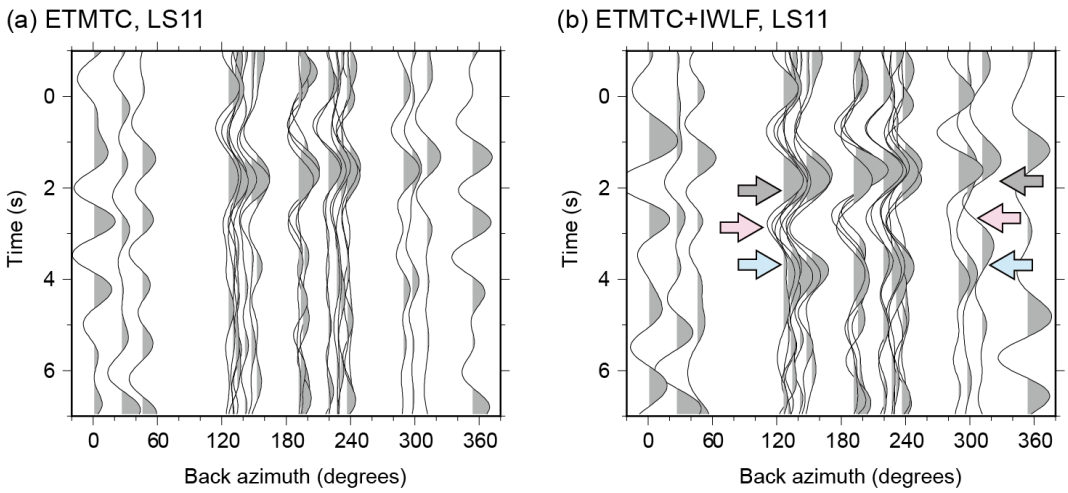

Figure 3.11. Radial receiver functions (RFs) calculated at a single ocean-bottom seismometer (LS11): (a) without removal of water reverberations and (b) after removal of water reverberations. Positive amplitudes of RFs are shaded with dark gray. Gray, pink, and pale blue arrows indicate major RF peaks, which we interpret as P-to-S conversion phases from the bottom of the sediment layer, plate interface, and oceanic Moho, respectively. All RFs are band-pass filtered between 0.1 and 1.0 Hz.

4. Receiver function image of the subducting Philippine Sea plate

In the last two chapters, we introduced the IWLF method to better estimate RFs using OBS data. For the first application, in this chapter, we perform RF imaging to reveal the 3-D geometry of the subducting plate and evaluate the hydrous state of the subducting plate from RF amplitudes.

4.1. Common conversion point stacking

This section describes the method for constructing RF images of subsurface structures. We first calculated radial RFs for all the stations, including the on-land stations (Figure 1.2), using the ETMTC method with band-pass filters of 0.1–1.0 Hz. For OBS data, we applied IWLFs to the vertical component records prior to the RF calculations, where we discarded event records which show positive ΔRMS-ACF value. For the IWLF parameter, we used station-specific values that were estimated in Section 3.1 (i.e., stars in Figure 3.5a).

Amplitudes of resultant radial RFs at the OBSs were significantly larger than those at the on-land stations by a factor of 3–8. We believe that this amplification originates from the unconsolidated sediment layer beneath the seafloor and the removal of downward P-wave reflection at the seafloor from OBS vertical component records. Note that the latter effect produces relative amplification by factor of $\sim 1 + R$, that is still insufficient to explain the observed amplification. The large amplification by the soft sediment seems reasonable, considering its extremely high Vp/Vs ratio, which is ~2 at 1 km depth from the seafloor and increases up to ~13 at the seafloor [*Hamilton*, 1979]. Such more reduced S-wave velocity than P-wave velocity would lead to more amplified horizontal ground motion than vertical motion. In Figure 4.1, we show teleseismic waveforms of the same event recorded at different sites. We can confirm significant

variation in amplitudes among sties even before the application of IWLF. We interpret this as due to amplification by different site responses. To reduce this amplification, we calculated the averaged energy ratio of radial component event records to vertical component records for each station (Figure 4.2) and normalized all radial RFs using these ratios (empirical correction of RF amplitudes). The averaged energy ratio was calculated as follows:

$$Energy\ ratio = \sum_{j} \sqrt{\frac{\int \{u_r^{(j)}(t)\}^2 dt}{\int \{u_v^{(j)}(t)\}^2 dt}}, \tag{14}$$

where, $u_r^{(j)}(t)$ and $u_v^{(j)}(t)$ represent radial and vertical component records of the jth event.

We then applied time-to-depth conversions to these RFs by referring to 1-D station-specific velocity structures extracted from the 3-D tomography model [*Akuhara et al.*, 2013]. As the tomography model employed station correction values that compensated for arrival time delays due to thin sediment layers beneath the seafloor, we shifted the time series of RFs in accordance with the correction values. We applied a uniform shift throughout the entire time series. The station correction values are ~0.0 s and ~-0.8 s for P- and S-wave arrivals, respectively, at offshore sties on average (Figures 4.3a and b), where a negative value means that observed arrival times are delayed with respect to the synthetic arrival times. After application of the time shift, we can directly compare the RF and the tomographic image.

We finally performed common-conversion-point stacking [*Dueker and Sheehan*, 1997] along trough-parallel and trough-normal profiles (X- and Y-axes, respectively) with a separation distance of 10 km (Figure 4.4a). Each profile contains grid points spaced 2.5 km horizontally and 0.25 km vertically. First, we calculated ray paths for all event records based on station-specific 1-D velocity structures, event back azimuths,

and ray parameters. The 1-D velocity structures were extracted from the 3-D tomography model [*Akuhara et al.*, 2013]. These calculated ray paths were then discretized vertically with 0.25 km spacing and projected onto profiles within 10 km distance. Finally, the RF amplitudes were stacked at the grid point closest to the projected points. The same amount was also added to the neighboring four grid points to obtain a smoothed RF image. This process is schematically shown in Figure 4.4b.

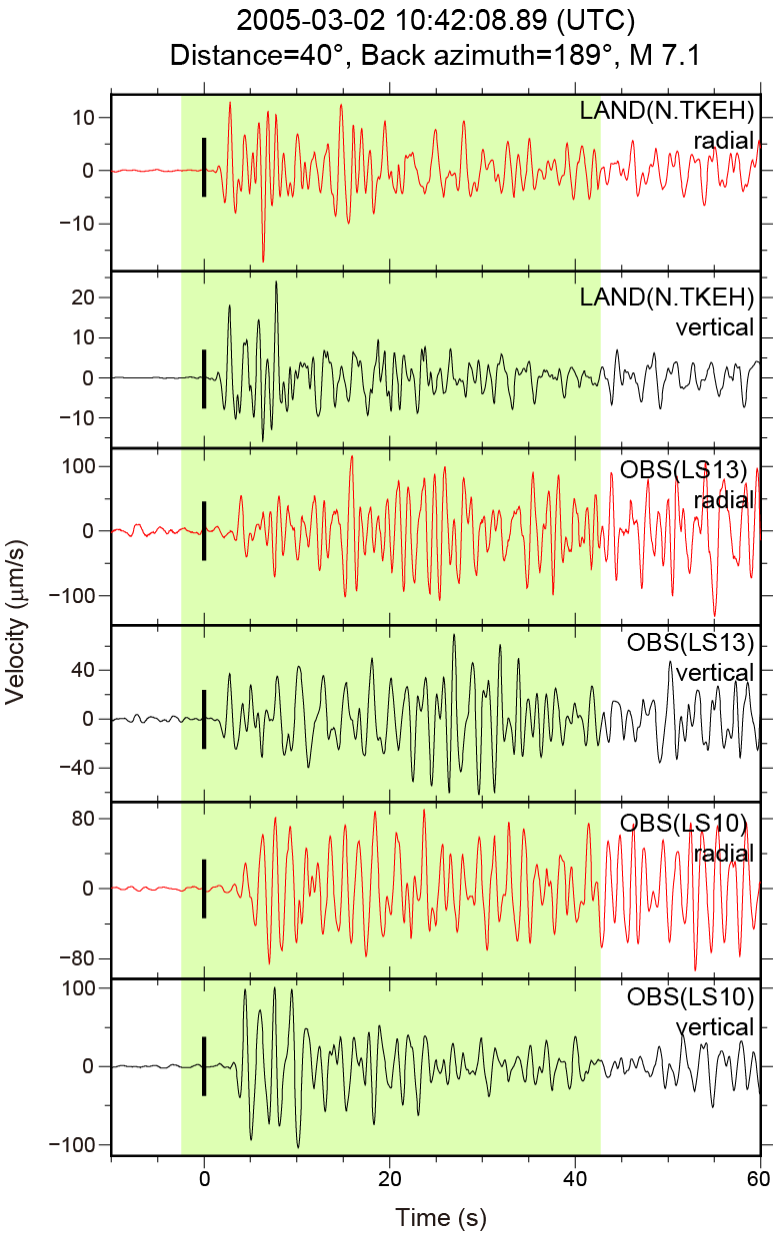

Figure 4.1. Teleseimic waveforms recorded by radial (red trace) and vertical component sensors (black traces) at several stations. Thick bars represent theoretical P-wave arrival times. Light-green shaded area shows time windows used to calculate average energy ratio of radial to vertical component records. Instrumental responses are already removed at all waveforms, but water reverberations are not. Station names are represented in the upper right corner of each panel, and the station locations are indicated in Figure 4.2.

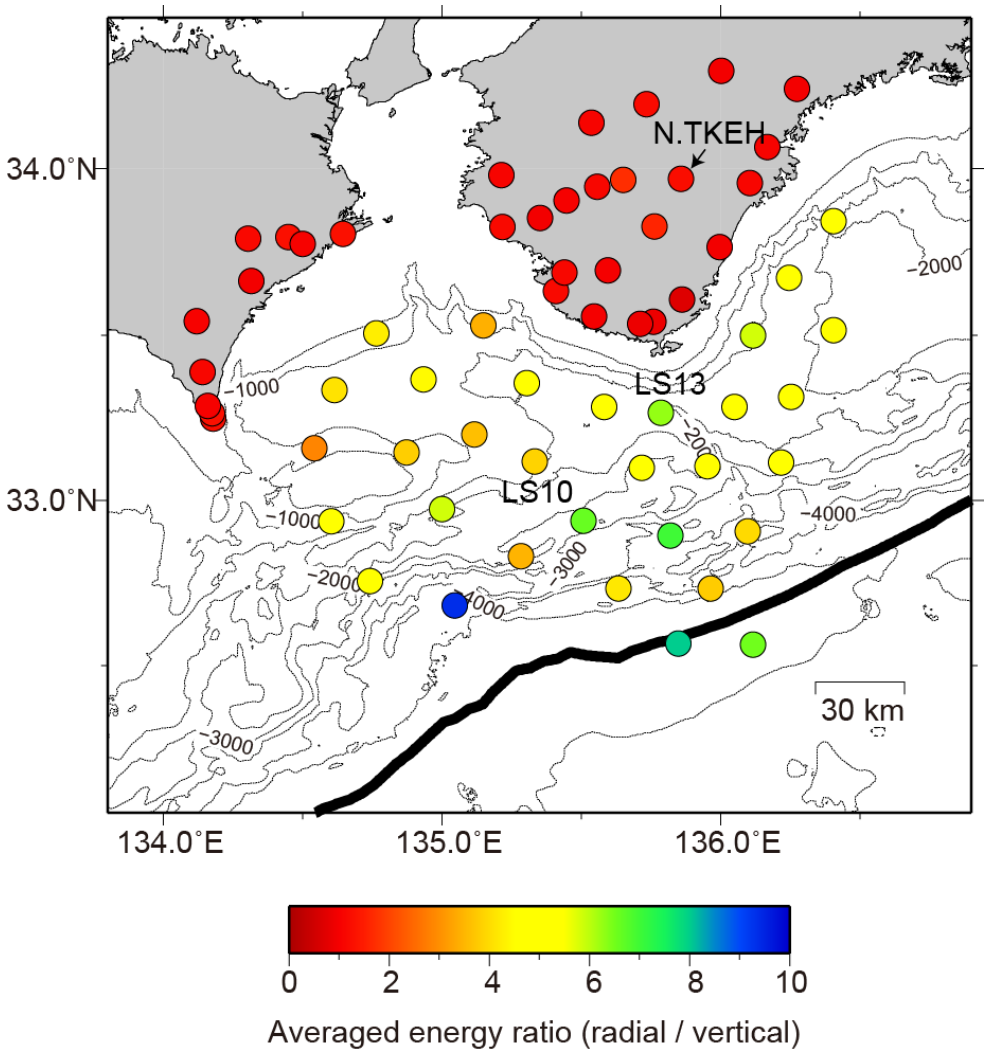

Figure 4.2. Averaged energy ratio of radial to vertical component event records for each station (circles). Note that the energy ratio shown here is normalized so that the averaged value of on-land stations becomes one.

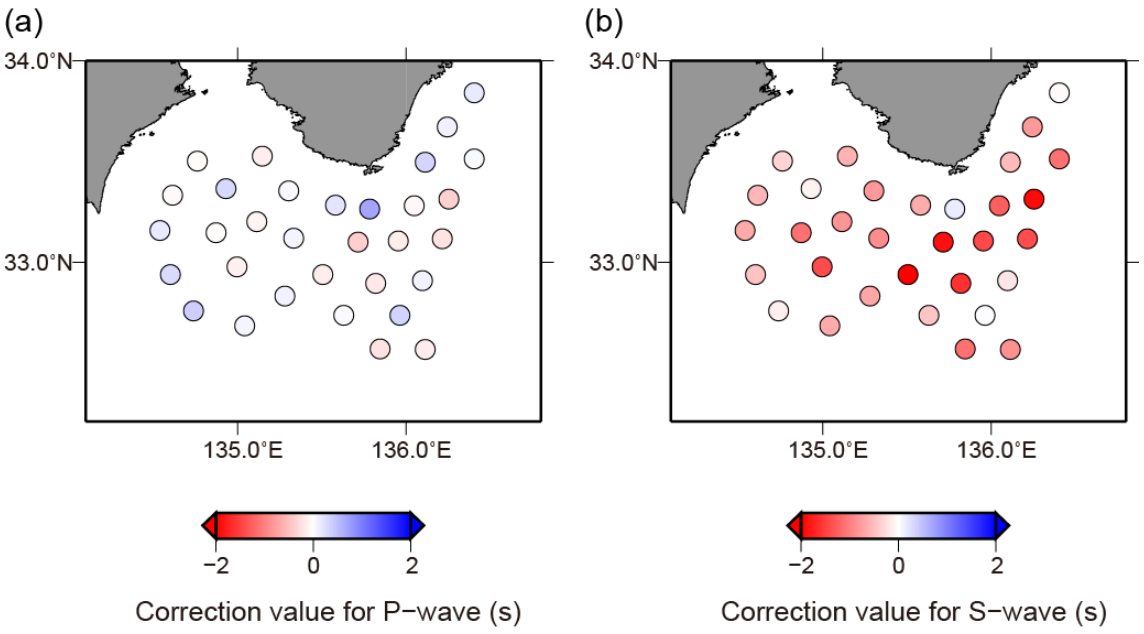

Figure 4.3. Station correction values for each OBS obtained by *Akuhara et al*. [2013] for (a) P- and (b) S-wave arrival times.

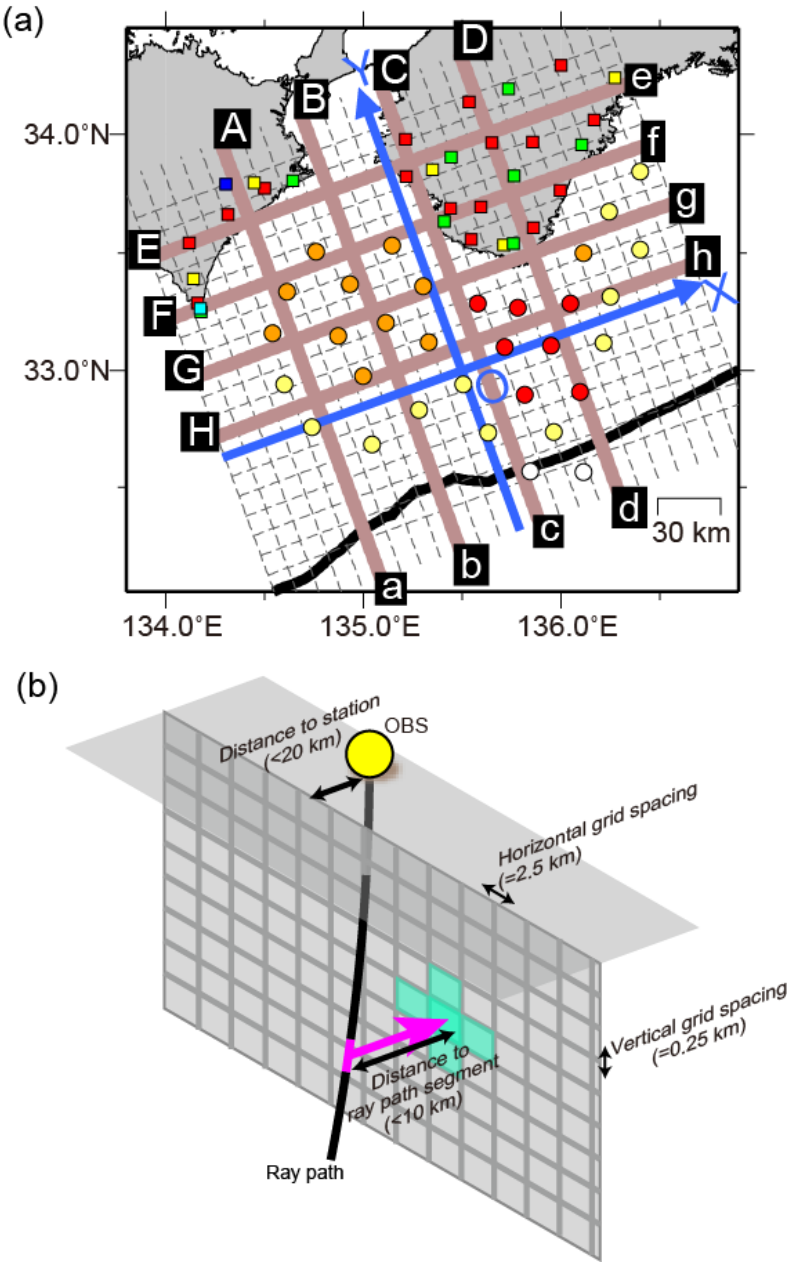

Figure 4.4. (a) Location map of cross sections for common-conversion-point (CCP) stacking. Gray dashed and brown thick lines represent cross sections used in the CCP stacking. On-land stations and ocean-bottom seismometers are shown with the same notation as in (Figure 1.2). (b) Schematic illustration of CCP stacking. Note vertical exaggeration. Ray path segment highlighted with pink is projected to five adjoining grids highlighted with green.

4.2. Results

4.2.1. 3-D geometry of the subducting Philippine Sea plate

Figures 4.5 and 4.6 show the common-conversion-point stacking profiles and the P-wave tomography model, respectively. Dominant positive amplitudes appear just above the high-velocity zone of the tomography model (Vp $\gtrsim$ 7.5 km/s), which can be traced as landward descending curves. We interpret these as the subducting oceanic Moho. To construct the 3D geometry model of the oceanic Moho, we measured the depths of these RF peaks at as many horizontal grid points as possible and fitted a minimum-curvature surface with tension [*Smith and Wessel*, 1990] to their depths (Figure 4.7a).

The model obtained in this way resolves the geometry of the subducting oceanic Moho from 20-35 km depth in the western region (X < 0 km) and from 15–50 km depth in the eastern region (X > 0 km). Because of poor velocity constraint on the tomography model, we did not include marginal regions in our model. The modeled region is outlined by the light-blue line in Figure 4.7. The depth of the oceanic Moho monotonously increases along the trough-normal direction except at Y = 15–55 km along the A-a profile. We consider that this portion represents a subducting seamount identified by a previous active-source survey [*Kodaira et al.*, 2000, 2002]. Our model mostly agrees with the results of previous active-source seismic surveys in offshore regions [*Mochizuki et al.*, 1998; *Kodaira et al.*, 2002, 2006] and RF analyses of onshore regions [*Shiomi et al.*, 2008; *Kato et al.*, 2014].

Ide et al. [2010] proposed the existence of a tear in the subducting PHS plate along the eastern edge of the subducted Kinan Seamount Chain (almost coinciding with the X = 0 km line) based on the on-land RFs, seismicity, and focal mechanisms of local earthquakes. Our RF image depicts abrupt depth change of the oceanic Moho with eastward dip at around X = 0 km along the E–e profile (Figure 4.5). Also the

tomography model shows similar depth change and eastward dip of high velocity zone (> 7.5 km/s) which is considered as the oceanic mantle (Figure 4.6). Whether the eastward dipping structures in these figures are true or not is of interest to confirm the existence of the tear. However, we must pay careful attention to spatial resolution and smoothing constraint for these figure before making a conclusion, which we left for our future study. Further investigation at more landward region should be helpful to resolve this question.

We also recognize that negative amplitudes of RFs can be traced subparallel to and above the oceanic Moho. This implies the existence of a low-velocity zone (LVZ) beneath the negative amplitudes. We can trace this area of negative RF amplitudes in the shallow part, even beneath the offshore region. We interpret the negative amplitudes as the top of the oceanic crust (i.e., the plate interface). Referring to these negative RFs, we estimated the thickness of the oceanic crust to be 8 km. This thickness is consistent with the results of previous active-source seismic surveys [*Mochizuki et al.*, 1998; *Kodaira et al.*, 2002, 2006], except near the seamount. Low-frequency earthquakes occur near the plate interface, as interpreted from the negative amplitudes (Figure 4.6), which is consistent with the widely accepted idea that low-frequency earthquakes occur on plate interfaces [*e.g., Shelly et al.*, 2006].

Beneath the Kii Peninsula, we can see that positive RF amplitudes form a plane with gentle northward dip whose depth varies from 20 to 30 km (dotted curves in Figure 4.5 and Figure 4.6). We interpret this plane as the island-arc Moho. Such a dipping Moho interface in this region has been reported by [*Kato et al.*, 2014], who performed RF and tomographic analyses along a dense seismic linear array. The location of intersection between the island-arc Moho and the subducting plate was not resolved from our results. Below the island-arc Moho interface, the tomography model shows high velocity (> 8.0 km/s) at the most northern part beyond the tremor zone, whereas the southward part exhibits lower velocity (~7 km/s) (Figure 4.6). Although this high

velocity zone is located on the northern edge of the resolvable area, similar structure can be seen in another tomography model which were determined from different dataset with better station coverage to the north [*Matsubara et al.*, 2008] (Figure 4.8).

4.2.2. Receiver function amplitudes along the subducting plate

We mapped RF amplitudes along the oceanic Moho and plate interface as follows. First, we evaluated the RF amplitudes at both the oceanic Moho and the plate interface for each ray path by taking an average value within a segment penetrating a $\pm$1-km-thick volume on both sides of the interface along the ray path. Then, these averaged amplitudes were stacked within each half-overlapped 20 $\times$ 20 km square bin across our study area and their averaged amplitudes and uncertainties were evaluated. We employed the bootstrap method with 1000 times resampling to estimate the uncertainties.

Figures 4.7b and c show the resultant RF amplitudes along the oceanic Moho and the plate interface, respectively. Figures 4.7d and e show the same ones but the area whose absolute RF amplitude less than 2σ standard error is masked. In these figures we show the amplitudes outside of the modeled region for reference. The oceanic Moho is characterized by mostly positive RF amplitudes. We can trace the negative amplitudes of the plate interface extending seaward to ~5 km depth south off the Kii Peninsula, which implies that the low-velocity zone exists directly beneath the plate interface. At the central part of the offshore region, we can see that the amplitudes of both the plate interface and the oceanic Moho are reduced.

We can also recognize that the absolute RF amplitudes of both the oceanic Moho and the plate interface are reduced where the top of the PHS slab subducts to $\geq$35 km depth beneath the Kii Peninsula, while the adjacent updip region is characterized by amplitudes that are more intense. The spatial extent of the zone of reduced amplitudes coincides well with that of deep non-volcanic tremors.

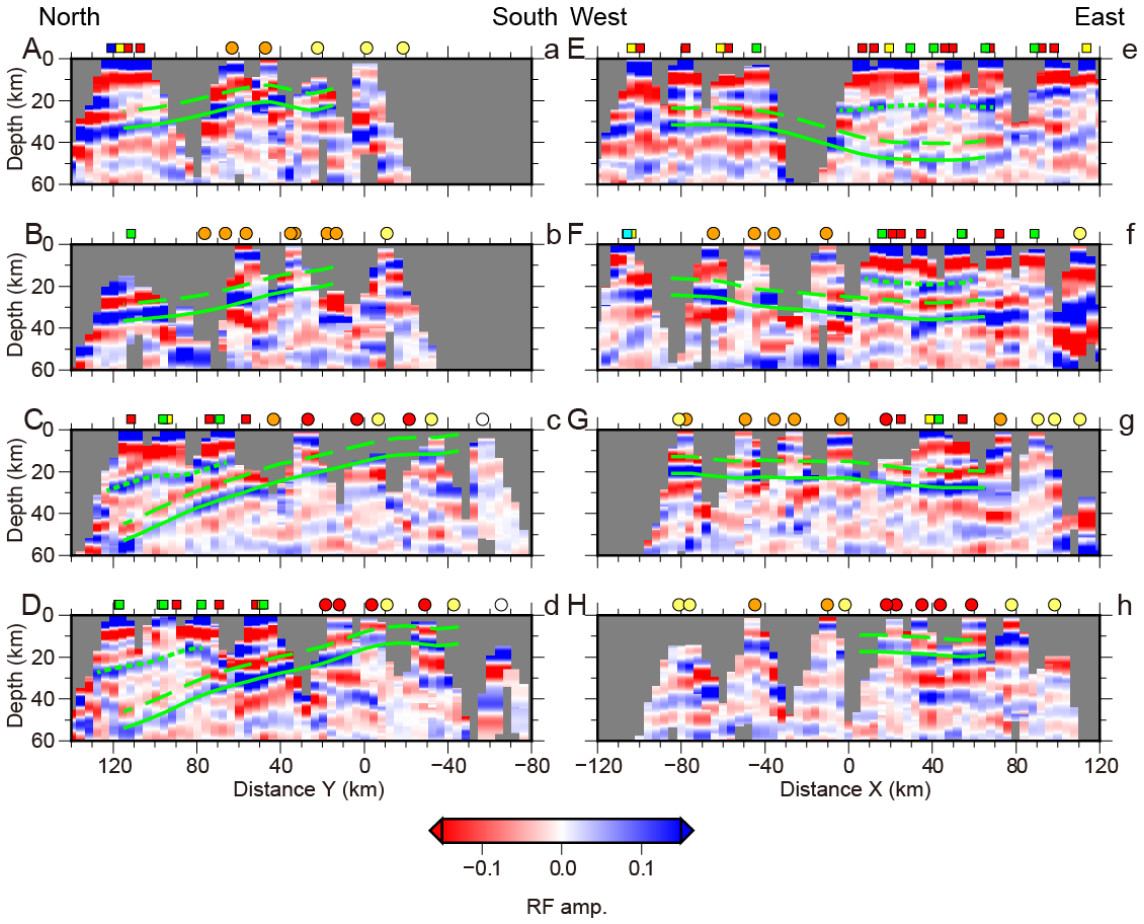

Figure 4.5. Receiver function (RF) image constructed by CCP stacking. Green solid, dashed, and dotted curves depict the 3-D geometry model of the oceanic Moho, the plate interface and the island-arc Moho, respectively. Locations of these cross sections are shown in Figure 4.4.

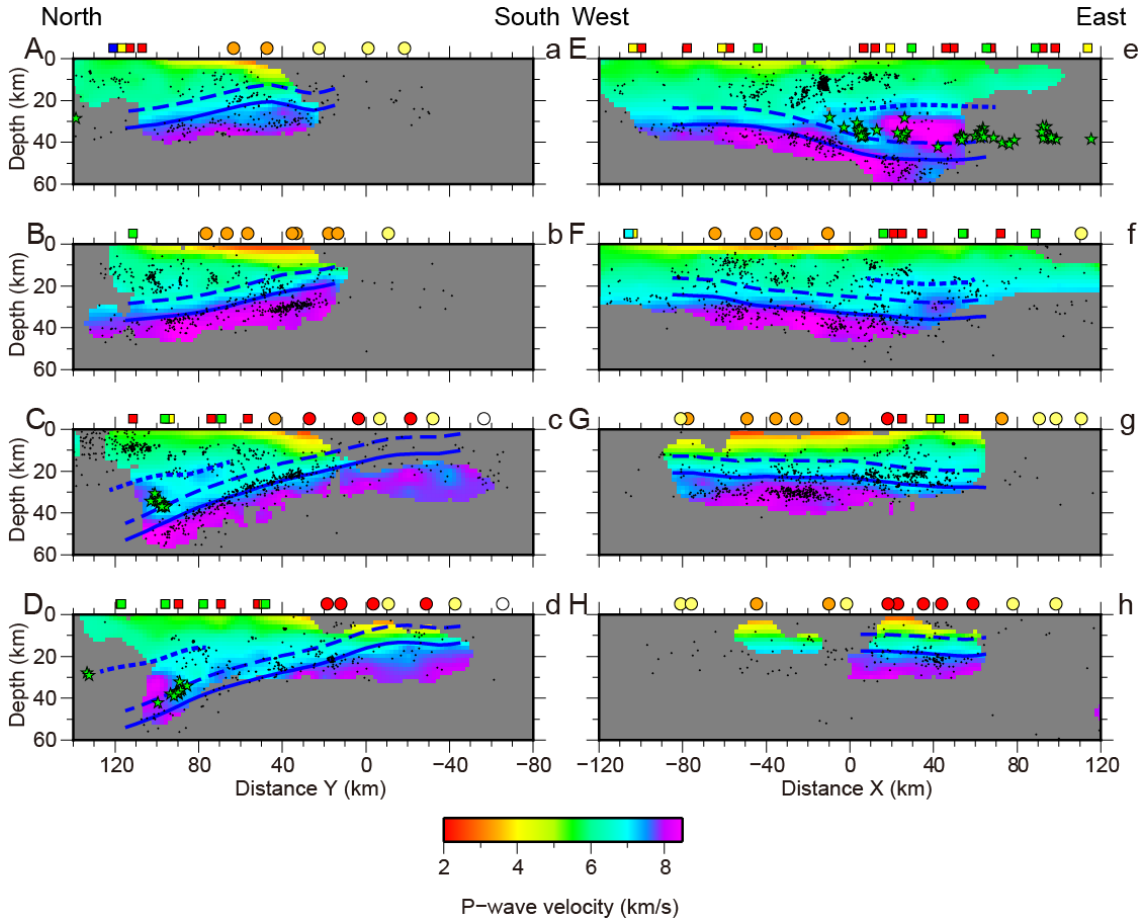

Figure 4.6. 3-D P-wave velocity model from the previous tomographic study [*Akuhara et al*., 2013]. Region where the velocity is not constrained well is masked by gray color. Blue solid, dashed and dotted curves depict the 3-D geometry model of the oceanic Moho, the plate interface, and the island-arc Moho respectively. Green stars and black circles represent low-frequency earthquakes and regular earthquakes relocated by *Akuhara et al*. [2013], respectively, whose locations are within 10 km distance from the profiles. Locations of these cross sections are shown in Figure 4.4.

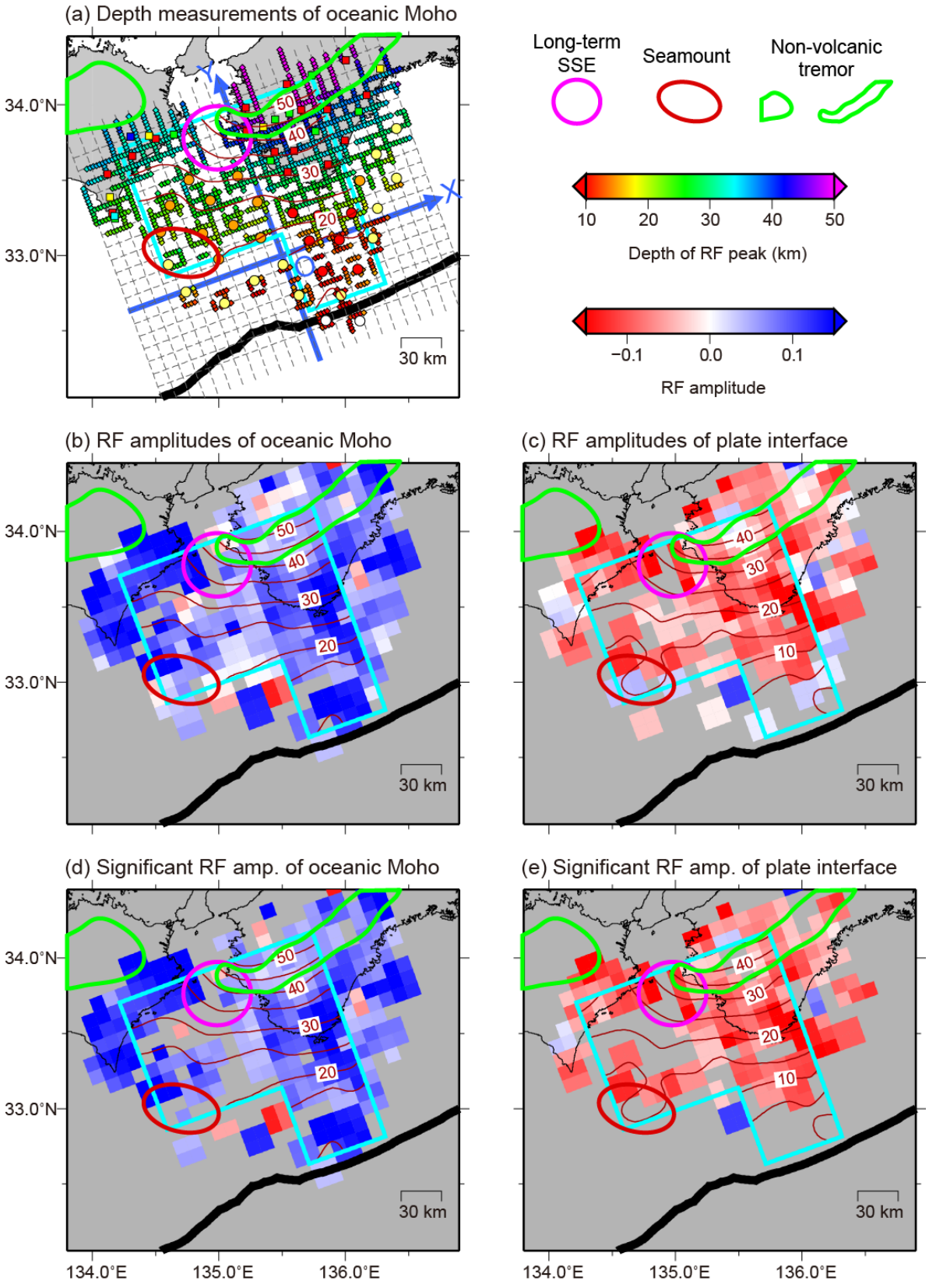
(a) Depth measurements of oceanic Moho
Long-term SSE
Seamount
Non-volcanic tremor
10 20 30 40 50
Depth of RF peak (km)
−0.1 0.0 0.1
RF amplitude
(b) RF amplitudes of oceanic Moho
(c) RF amplitudes of plate interface
(d) Significant RF amp. of oceanic Moho
(e) Significant RF amp. of plate interface
34.0°N
33.0°N
30 km
134.0°E
135.0°E
136.0°E

Figure 4.7. (opposite) (a) The modeled geometry of the subducting oceanic Moho (brown contours). Small diamonds denote depths of receiver function (RF) peak used in the construction of the oceanic Moho model. Circles and squares represent ocean-bottom seismometer and on-land stations, respectively, with the same colors as used in Figure 1.2. Gray dashed lines show the locations of the vertical profiles for common-conversion-point stacking. Light-blue lines enclose the area where the tomography model is well constrained. RF amplitudes of (b) the oceanic Moho and (c) the plate interface. Brown contours in (b) and (c) denote the depths of the oceanic Moho and plate interface, respectively. Brown, pink, and light-green lines depict the subducted seamount [*Kodaira et al.*, 2000], slow slip region [*Kobayashi*, 2014], and the belt zone of non-volcanic tremors, respectively. (d, e) The same as (b, c), respectively, but the area whose absolute RF amplitude is less than 2σ error is masked.

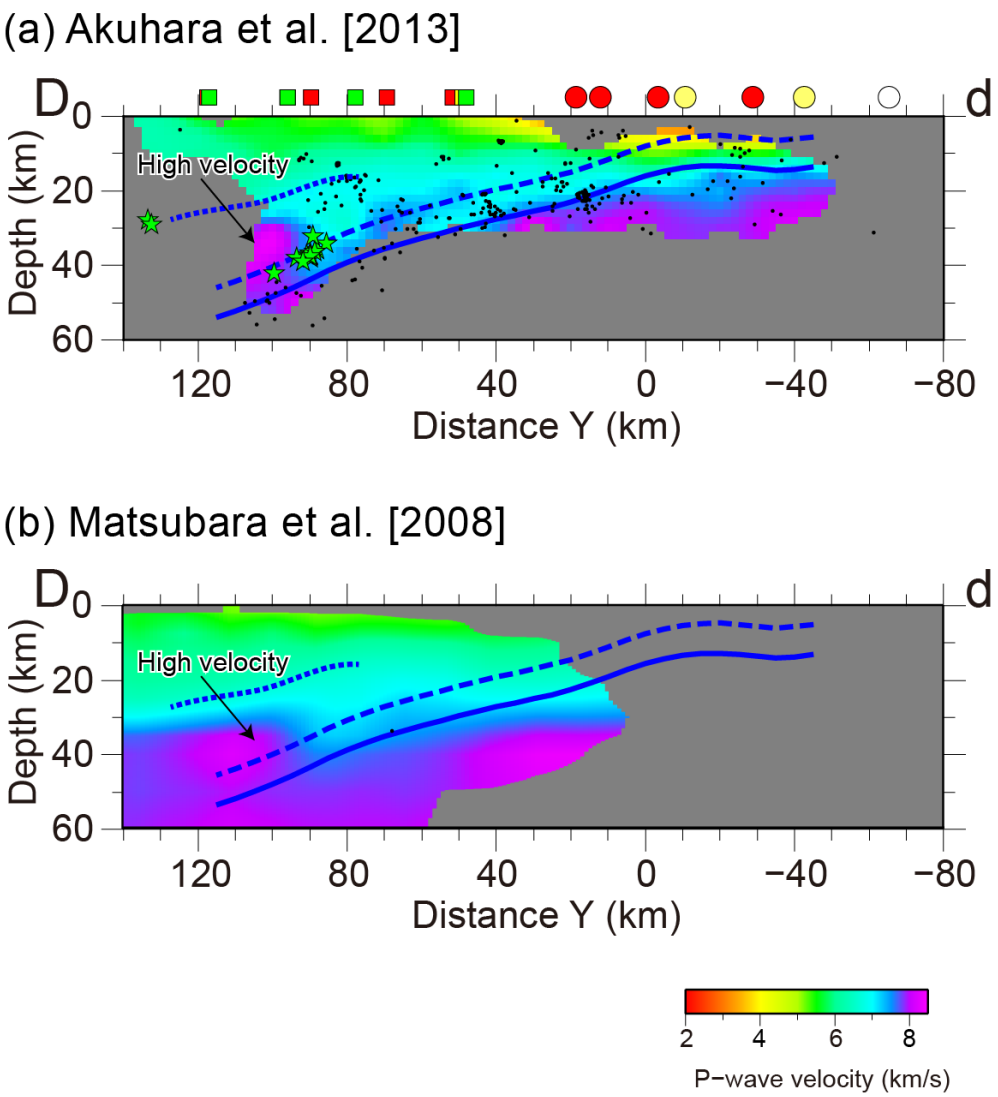

Figure 4.8. Comparison between two tomography models by (a) *Akuhara et al.* [2013] and (b) *Matsubara et al.* [2008]. The locations of these cross sections are exactly identical (D-d profile in Figure 4.4). The island-arc Moho, the oceanic Moho and the plate interface modeled in this study are shown with the same notation as Figure 4.6 on both panels.

4.3. Discussion

4.3.1. Forward modeling of amplitude reduction beneath the Kii Peninsula

We conducted additional tests to confirm whether the reduced amplitudes in the tremor zone truly represented the elastic properties along the interfaces. Our concern is that the observed patterns in the RF amplitudes mainly originate from the change in the dip angle of the slab, and thus, they do not represent elastic properties. The teleseismic events we used are mostly located to the south of the network (Figure 1.3), so their incident angles to the subducting interfaces approach perpendicular to the interfaces as the subduction angle become steeper beneath the Kii Peninsula. This could be a cause of the RF amplitude reduction beneath the Kii Peninsula.

To minimize the effect from the dipping layer, we gathered RFs whose back azimuth is within a $\pm 25°$ range from perpendicular direction to the dip direction of the slab and within epicentral distances between 35°-55°. Then, we stacked these selected RFs for each station and aligned them in an order of depth to the oceanic Moho (Figure 4.9a). The RFs used here were calculated in the same manner as introduced in the Section 4.1 but extending the frequency bandwidth to 0.0-1.0 Hz to reduce ringing feature. We manually picked the P-to-S conversion phases from the plate interface and the oceanic Moho (Figure 4.9a), and measured their amplitudes (Figure 4.9b). The uncertainties of these amplitudes were estimated from the variations of pre-stack RF amplitudes. We discarded results from the stations whose absolute amplitude was less than 1σ standard error at either the oceanic Moho or the plate interface (triangles in Figure 4.9b). In addition, we also discarded results from the two most inland stations (squares in Figure 4.9b), because the assumption of negative phase at the plate interface may not be correct at the depth due to the eclogitization of the oceanic crust [*Kato et al.*, 2014]. Even after minimizing the slab dip effects in this way, we can still see the amplitude reduction with the subduction depth (see fitted lines in Figure 4.9b).

Therefore, we conclude that this amplitude reduction reflects the change of elastic property contrast.

Next, we evaluated the S-wave velocity of the oceanic crust from the observed RF amplitudes along the plate interface. For the purpose, we calculated synthetic RFs using velocity model composed of an overriding plate with velocity gradient along the depth, homogeneous oceanic crust, and oceanic mantle (Figure 4.10c). The method to calculate synthetic RFs is the same as Section 2.2, where ray parameter was set to be the average of the observed RFs. For each station, we adjusted the S-wave velocity of the oceanic crust so that synthetic amplitudes of the P-to-S conversion phases from the plate interface can reproduce the fitted lines of the observed RF amplitudes. P-wave velocity of the oceanic crust and P- and S-wave velocities of the other layers were derived from the tomography model [*Akuhara et al.*, 2013], and density was assumed by an empirical relationship with P-wave velocity [*Birch*, 1961].

As a result, we found that drastic increase in the S-wave velocity from 2.9 to 4.2 km/s with subduction depth was essential to explain the observed amplitude reduction (Figures 4.10a and b). According to a phase diagram of MORB (mid-ocean ridge basalt) [*Peacock*, 1993] and a pressure-temperature path simulated for the subducting PHS plate beneath the Kii Peninsula [*Yamasaki and Seno*, 2003], the oceanic crust at the shallow part (~20 km depth) is considered to correspond to greenschist facies and the deep part (>40 km depth) to eclogite facies (Figure 4.11). The S-wave velocity of 2.9 km/s, however, is about 25% slower than the velocity of greenschist facies expected from laboratory experiments (Figure 4.10b) [*Christensen*, 1996]. We interpret that the oceanic crust therein hosts abundant fluid to realize such slow velocity at the shallow depth. The highest velocity, 4.2 km/s, is close to the shear velocity of eclogite facies, but still 10% slower than laboratory measurements (Figure 4.10b). We also consider that this reduction in S-wave velocity is attributed to fluid, but that the amount of fluid is not as much as that of the shallow part.

4.3.2. Uncertainty estimates for the relative depth of hypocenters to the oceanic Moho

In Figure 4.12, we show the hypocenters relocated by *Akuhara et al.* [2013] and the geometry of the PHS slab obtained in this study, both of which were determined by referring to the same tomography model. Here, we aim to evaluate uncertainties of relative depths of these local earthquakes to the oceanic Moho for the following discussion. We make a rough estimate on the uncertainties using some typical values. In the following discussion, we adopt 6.8 km/s and 3.8 km/s as typical values of P- and S-wave velocities, respectively, which represent the velocities of the oceanic crust. In addition, we use 0.55 Hz, corresponding to the central frequency of our band-pass filter, to estimate typical wavelengths of RFs.

First we need to evaluate the uncertainties of the depths of the oceanic Moho. We considered that these uncertainties originate from two factors: (1) high frequency component removed by our band-pass filtering and (2) biases from the assumption of 1-D velocity models without any dipping structures. The first type of uncertainties, referred to as σ_{m1}, are considered to be an eighth of the wavelength of RFs, which we estimated to be ~2 km. The second type of uncertainties (σ_{m2}) have been well discussed by *Shiomi et al.* [2004], who investigated how depth estimations of a dipping oceanic Moho are affected by the assumption of a horizontal oceanic Moho. In accordance with their work, we adopted ~3 km as the typical values for σ_{m2}, corresponding to the case of the oceanic Moho with 15° dip angle subducted to 30 km depth.

For hypocenter errors (σ_h), we utilized root mean squared residual values between observed and synthetic travel times from the previous tomography analysis [*Akuhara et al.*, 2013]. In average, the values are 0.08 s and 0.12 s for P- and S-waves, respectively. Using the typical values of the oceanic crustal velocity, we estimated the uncertainty of hypocenters to be less than 1 km.

Combining the three types of errors, σ_{m1}, σ_{m2}, and σ_h, into a single composite uncertainty, $\sqrt{\sigma_{m1}^2 + \sigma_{m2}^2 + \sigma_h^2}$, we assumed that relative location error of hypocenters to the oceanic Moho would be ~4 km at most. Other than these three kinds of uncertainties, the uncertainty in the 1–D velocity models themselves and the station correction values should be taken into consideration for error estimations of the absolute depths. However, we could neglect such factors in discussing the relative location errors, because the errors for hypocenters and the oceanic Moho would be canceled out mutually.

4.3.3. Hydrous state of the subducting oceanic crust

To date, many studies have used RFs to infer the hydrous state of subducting slabs in many subduction zones (*Bostock* [2013] and references therein). Generally, based on observations of dominant negative RF amplitudes along the plate interface overlying positive RF amplitudes of the oceanic Moho, these studies support the idea that oceanic crust hosts abundant fluid. The most likely origin of the fluid is dehydration of the subducting slabs, which has been supported by numerous studies [e.g., *Hacker et al.*, 2003].

In accordance with these studies, we interpret that negative RF amplitudes along the plate interface ranging from 5–35 km depth (Figure 4.7e) reflect the existence of fluid below the interface. Although this interpretation lacks quantitative verification, this is in good agreement with other independent observations in this region by *Kodaira et al.* [2002] and *Kurashimo et al.* [2013]. They performed active-source seismic surveys in offshore and onshore regions of this study area, and identified reflective phases characteristic of trapped fluid along the plate interface. The possible sources of the fluid are a series of metamorphic dehydration reactions of the oceanic crust, including zeolite, pumpellyite-actinolite, greenschist, epidote-amphibolite and amphibole-eclogite (Figure 4.11), and porosity collapse of the oceanic crust [*Hyndman*

and Peacock, 2003]. An important implication of this interpretation is that the plate interface must be impermeable, or sealed, in order to trap fluid within the oceanic crust. This permeability barrier might originate from small-grained silicic mudrock, foliations of phyllosilicates formed by coseismic rupture, and hydrothermal precipitation of silicic materials [*Sibson*, 2013 and references therein].

In the following, we infer the hydrous state of the subducting PHS plate, dividing our study area into three regions: the Kii Peninsula, the Southeastern Shikoku Island, and the offshore region. Evidence for the following interpretation is mainly from spatial variation of RF amplitudes, but we will also refer to some independent results from other studies.

<Kii Peninsula>

We first focus on the Kii Peninsula, where the PHS plate subducts to 20-45 km depth and RF amplitudes decrease significantly with the slab subduction. Given the pressure-temperature path of *Yamasaki and Seno* [2003] and the phase diagram of MORB from *Peacock* [1993], metamorphic phase change is considered to occur within the oceanic crust from greenschist to epidote-amphibolite to eclogite facies (Figure 4.11). As we have already stated in Section 4.3.1, the RF amplitude reduction can be explained by the combination of the increase in seismic velocity with metamorphic phase change and the decrease in fluid content within the oceanic crust. We believe this change in the fluid content comes from the change in permeability of the plate interface. At deeper part, successive dehydration reaction toward eclogite would be accompanied by densification. We consider such densification produces fracture within the oceanic crust, which results in the increase in permeability and allows fluid to ascend into overriding plate (Figure 4.13a). The similar interpretation has been made for Cascadia subduction zone [e.g., *Bostock*, 2013].

There are two independent observations that are in good agreement with our

interpretation and are thus worth discussing here. The first support comes from velocity of the overriding plate predicted by the tomography model [*Matsubara et al.*, 2008; *Akuhara et al.*, 2013]. From Figure 4.8, we can see that relatively low P-wave velocity (~ 7 km/s) is located within the island-arc mantle just above the subducting slab top to 30-40 km depth. We interpret this low velocity part as serpentinized mantle in accordance with laboratory experiments [*Christensen*, 2004]. Ascending fluid from the oceanic crust passing through the permeable plate interface is considered to contribute to this serpentinization (Figure 4.13a). Further inland beyond the tremor zone, the velocity of the island-arc mantle is considerably higher (> 8 km/s) and is interpreted to be non-serpentinized mantle. We conjecture that dehydration reaction of the oceanic crust has been completed at the depth, so no fluid would ascend into the island-arc mantle.

The second supportive observation comes from seismicity relocated by *Akuhara et al.* [2013]. Along the dip direction beneath the Kii Peninsula (along C-c and D-d profiles in Figure 4.12), we can recognize that the RF amplitudes tend to be strong at the seismogenic part of the oceanic crust. One possibility is that these earthquakes within the oceanic crust are promoted by elevated pore fluid pressure resulted from metamorphic phase change from greenschist to epidote-amphibolite facies (Figure 4.11). In fact, rapid rate of fluid production has been reported during this phase change [*Kuwatani et al.*, 2011]. The downdip offset of the seismogenic crust may coincide with the offset of this phase change. The aseismic oceanic crust in deeper portions probably is undergoing the next step of the dehydration reaction, from epidote-amphibolite to eclogite, starting with more gentle fluid production. Solid volume reduction due to the dehydration reaction may prevail over fluid volume expansion in this location; net reduction of the pore fluid pressure is considered to prohibit the occurrence of earthquakes as suggested by *Abers et al.* [2013].

Previous studies also reported the existence of LVZ or high-reflectivity zone

along the subducting plate beneath the Kii Peninsula and associated it with the slab dehydration reaction [e.g., *Kurashimo et al.*, 2013; *Kato et al.*, 2014]. The advance of this study over the previous studies is that our discussion is based on the quantified analysis using RF amplitudes. With this feature, we could interpret along-dip change in the fluid content and the permeability of the plate interface. The other advantage is that we conducted 3-D analysis, which allows us to understand that the reduction of RF amplitudes with the slab subduction is robust feature. Not only that, but we can recognize good spatial correlation between the reduced RF amplitudes and the source region of non-volcanic tremors, which we will further discuss in the next section (Section 4.3.4).

<Southeastern Shikoku Island>

Beneath the southeastern edge of Shikoku Island, such a significant RF amplitude reduction as beneath the Kii Peninsula cannot be seen. Because the subduction depth is shallow beneath the region, dehydration of the oceanic crust would not proceed such that at deeper part beneath the Kii Peninsula. We therefore conclude the plate interface is considered to be still impermeable to remain RF amplitude strong (Figure 4.13b). Along the A-a profile of Figure 4.12, we may see that the seismogenic part of the oceanic crust exhibits strong RF amplitudes, but relatively large errors make it difficult to reach any confident conclusion.

<Offshore region>

A striking feature in the RF amplitude pattern at offshore region is the reduced amplitudes of both plate interface and oceanic Moho at the central part, where the fossil spreading axis, or the Kinan Seamount chain has been subducted. Although we have no plausible explanation for this reduced amplitudes, some irregular structure associated with the subducted Kinan Seamount Chain might be responsible. In fact, previous studies have reported that velocity structure and stress filed undergo abrupt change

across the edge the seamount chain, emphasizing that the seamount chain exerts important control on tectonics of this region [*Mochizuki et al.,* 2010; *Akuhara et al.*, 2013]. In addition, *Akuhara and Mochizuki* [2014] have interpreted that earthquakes occur along a number of preexisting faults within the oceanic mantle at the very part of the reduced amplitudes. If the faults cut the oceanic crust, as speculated by *Akuhara and Mochizuki* [2014], it will also affects the fluid behavior and, in turn, RF amplitudes.

In contrast to the central part, the eastern-most part of our resolvable area is characterized by strong amplitudes, which is elongated updip from the southern tip of the Kii Peninsula. We consider this reflects abundant fluid content beneath the plate interface. From Figure 4.6e, we can recognize that this strong amplitude zone extends to 5 km depth, but its updip limit is not constrained. *Park et al.* [2014] has identified fluid-rich décollement at the southern extension of this strong RF amplitude zone from active source seismic surveys along the Nankai trough. We hence infer that the fluid-rich interface extends more seaward to near the trench.

So far, we discussed RF amplitude of the plate interface in the offshore region, by simply assuming that they reflect velocity contrast across the interface. Technically, however, we must pay more attention to the presence of unconsolidated sediment layer beneath the seafloor, because the layer yields reverberation phases on RFs. In Chapter 5, we will address this problem, by conducting receiver function inversion by taking sediment layer into fully consideration.

4.3.4. Permeability difference in source area of long-term slow slip events and tremors

Our results indicates spatial correlation between tremors and the reduced RF amplitudes, where we interpret that plate interface is permeable. This interpretation is in contrast to the relationship between the sealed plate interface and long-term SSEs, which has been well established by previous studies [*Kodaira et al.,* 2004; *Song et al.*,

2009; *Kato et al.*, 2010]. This difference in permeability might be an important factor in distinguishing long-term SSE and tremor zones, i.e., a sealed plate interface enables pore fluid to reduce the effective normal stress along a wide portion of the plate interface such that long-term SSEs can occur. Conversely, along a fractured plate interface, pore fluid pressure would be elevated only within small-scale patches of the fracture pattern. Although we have little constraint on the RF amplitudes of the 1996–1997 long-term SSE patch at the Kii Channel, the patch is most likely to be imaged as intense RF amplitudes based on the amplitudes of the neighboring region at the same depth range (25-30 km depth to the plate interface, see Figures 4.7d and e). We therefore consider it likely that the plate interface at the long-term SSE patch is impermeable, or at least less permeable than within the tremor zone (Figure 4.13c).

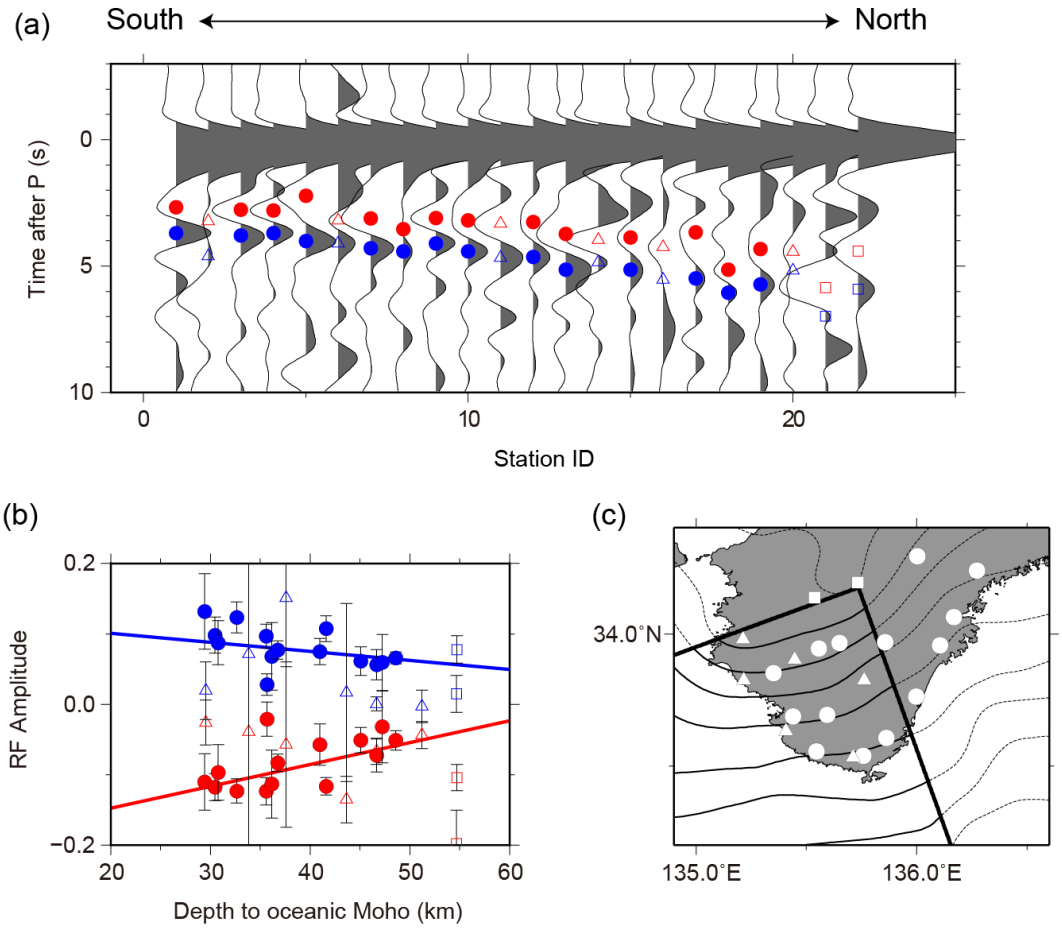

Figure 4.9. (a) Radial receiver functions (RFs) stacked at each station on the Kii Peninsula. Positive polarity is shaded with gray. Red and blue circles denote manual picks of P-to-S conversion phases from the plate interface and the oceanic Moho, respectively. Triangles and squares represent the same picks under but with large uncertainties of their amplitude and with less confidence in their phase identification, respectively. (b) Relationships between RF amplitudes of the P-to-S conversion phases and subduction depth. Error bars represent 1σ confidential regions of standard errors. Red and blue lines denote fitted line to good quality data (circles). (c) Locations of stations. Contour lines represent the oceanic Moho. Thick black lines enclose the area where the tomography model is well constrained.

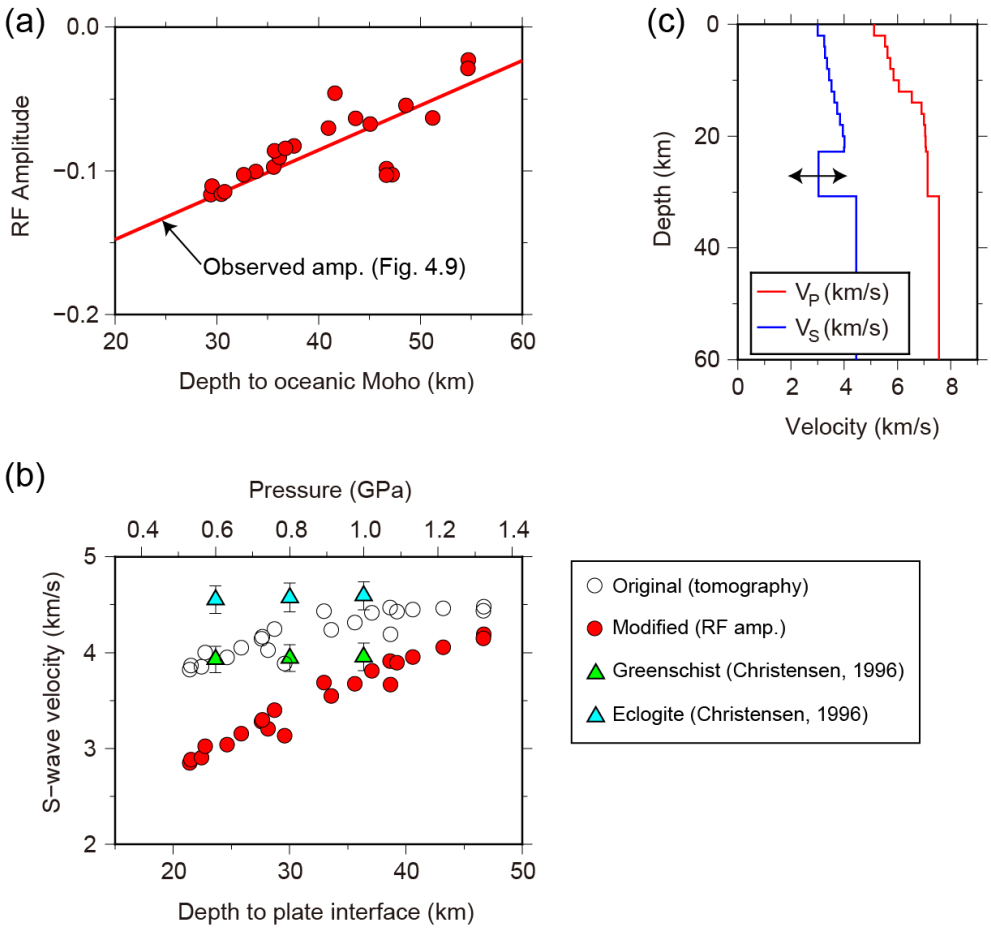

Figure 4.10. (opposite) Simple modeling of S-wave velocity of the oceanic crust beneath the Kii Peninsula using RF amplitudes. (a) Red circles represent synthetic RF amplitudes of the P-to-S conversion phases from the plate interface. Red line roughly indicates the observed amplitude the same as Figure 4.9b. (b) Red circles represent S-wave velocities of the oceanic crust which were modified to explain observed RF amplitudes. Open circles show those of the tomography model [*Akuhara et al.*, 2013] for comparison. Light green and sky blue triangles denote previous laboratory measurements for S-wave velocities of greenschist and eclogite, respectively [*Christensen*, 1996]. Pressure on the upper horizontal axis were calculated for the depth of the plate interface by assuming density to be 2.8 g/cm^3. (c) Typical velocity structure used in the synthetic calculations. We modified only S-wave velocity of the oceanic crust to fit synthetic RF amplitudes to the observed amplitudes.

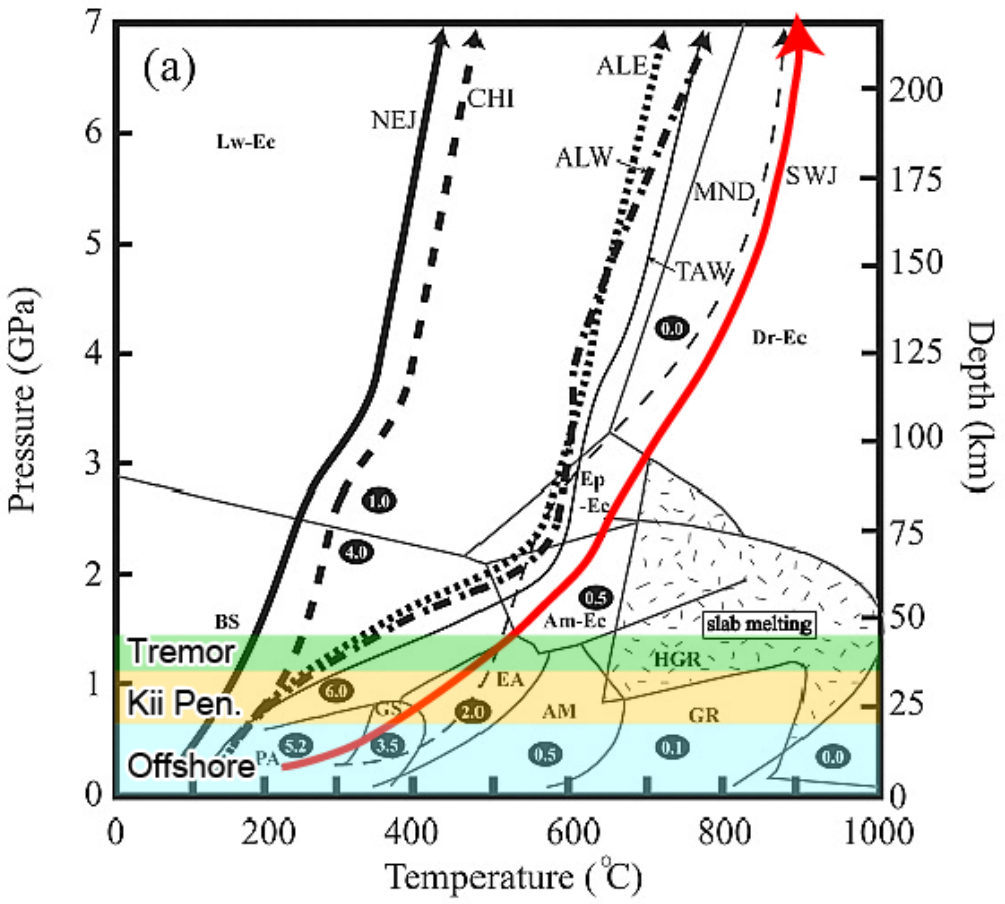

Figure 4.11. Pressure-temperature (P-T) path along subducting Philippine Sea plate beneath the Kii Peninsula (red curve) and phase diagram for water-saturated MORB (modified after *Yamasaki and Seno* [2003]). The P-T path were calculated by *Yamasaki and Seno* [2003], which passes pumpellyite-actinolite (PA), greenschist (GS), epidote-amphibolite (EA), and amphibole-eclogite (Am-Ec) facies. Shallow part of the phase diagram, below the eclogite facies, is based on *Peacock* [1993]. Note that the phase diagram presented here omits some phases which appear at low temperature (e.g., zeolite facies). Outline numbers represent maximum amount of H_2O in wt%. Explanation for the other notations can be seen in the caption of Figure 4a in *Yamasaki and Seno* [2003]. Shaded areas with pale blue, yellow, and light green colors highlight depth ranges of the subducting plate interface inferred from this study beneath the offshore region, the Kii Peninsula, and tremor belt, respectively.

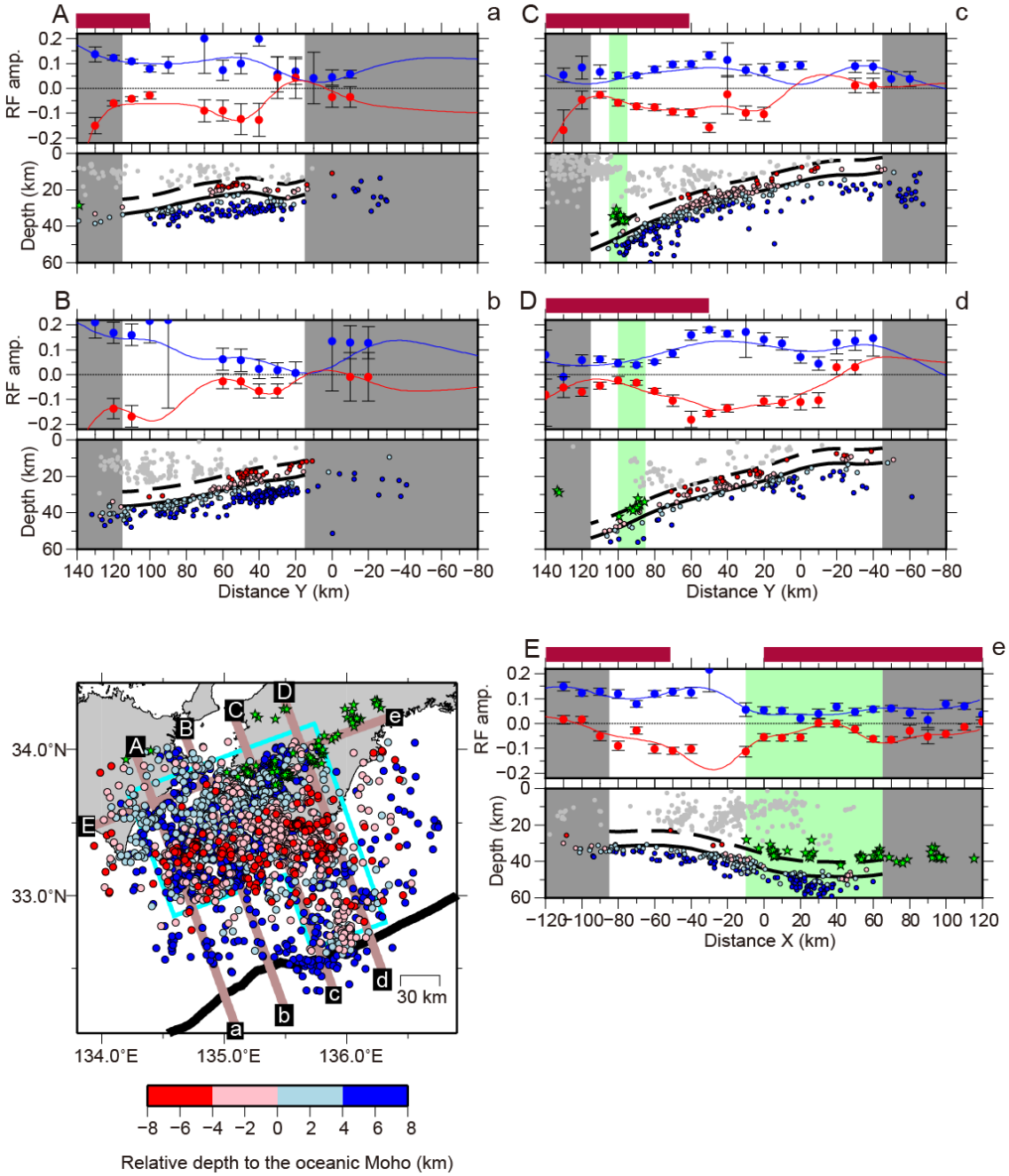
A
a
C
c
B
b
D
d
E
e
RF amp.
Depth (km)
Distance Y (km)
Distance X (km)
34.0°N
33.0°N
134.0°E
135.0°E
136.0°E
30 km
Relative depth to the oceanic Moho (km)

Figure 4.12. (opposite) Distribution of intraslab earthquakes, low-frequency earthquakes (LFEs), and receiver function (RF) amplitudes on the plate interface and oceanic Moho. Red and blue circles denote intraslab earthquakes occurring within the oceanic crust (red) and the oceanic Mantle (blue). Those earthquakes within 4 km distance from the oceanic Moho is discriminated by using pale color. Light-green stars represent LFEs. In the lower panel of each cross section, dashed and solid black curves indicate the plate interface and oceanic Moho modeled in this study, respectively. Earthquakes occurring above the plate interface are also indicated by gray circles. All hypocenters are located within 10 km from the profiles. In the upper panel of each cross section, red and blue circles show RF amplitudes on the plate interface and oceanic Moho along the profiles, respectively, while the red and blue curves show the laterally smoothed versions. Thick brown bars appearing above the upper panels show the extent of land area. Gray and green shaded areas correspond to the regions of the unconstrained tomography model and the range of LFE occurrences, respectively.

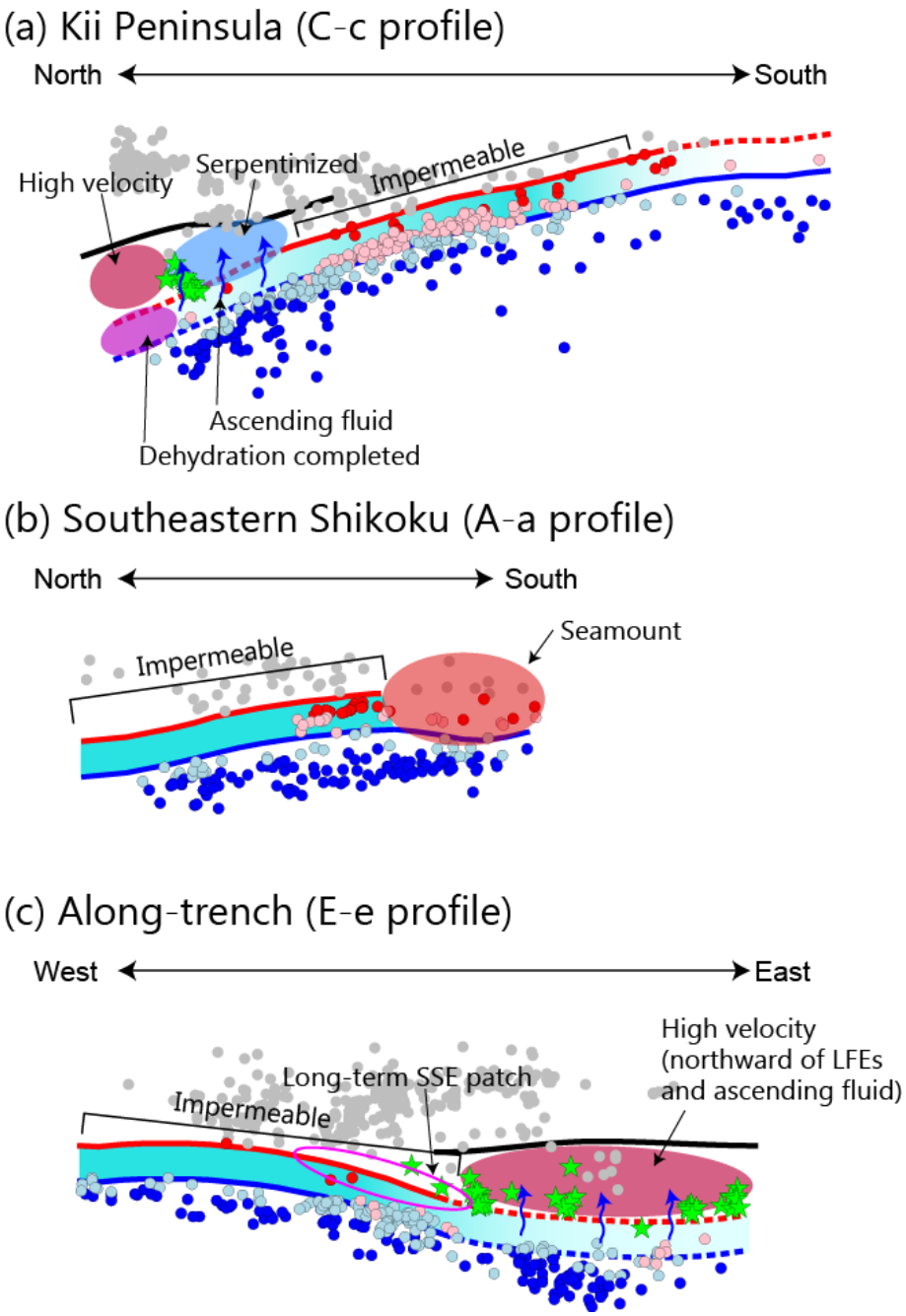

Figure 4.13. Schematic illustration of our interpretation along the profiles in Figure 4.12: (a) C–c, (b) A–a, and (c) E–e profiles. Circles and stars denote earthquakes and low-frequency earthquakes with the same color usage as Figure 4.12. Red, blue black curves show the plate interface, the oceanic Moho, and the island-arc Moho, respectively.

5. High-frequency receiver function inversion analysis to reveal fine structure around the plate interface

In the previous chapter, we found that the subducting plate interface was characterized by negative RF amplitudes even beneath offshore region. These negative amplitudes could support the existence of low-velocity zone (LVZ) right beneath the plate interface at seismogenic zone. A possible explanation for this LVZ is the hydrated oceanic crust, as we discussed in the last chapter. This interpretation partly originates from the thickness of the LVZ (~8 km, see Figure 4.5). Unfortunately, however, the thickness of the LVZ tends to be overestimated if the imaging process incorporates tomography model [*Audet et al.*, 2009]. That is because the tomographic method tends to underestimate velocity anomalies because of its smoothing constraint [e.g., *Song and Helmberger*, 2007].

Also in the last chapter, we evaluated the S-wave velocity of the LVZ beneath the land area of the Kii Peninsula from RF amplitudes. Such quantitative analysis is useful to make confident interpretation. In the case of OBSs, however, our empirical correction to the sediment amplification effects may not be sufficient for quantitative assessments.

With the points above considered, it is desirable to evaluate the physical properties and the thickness of the LVZ quantitatively by extracting as much information as possible from RF waveforms. In the case of OBS data, we have to pay careful attention to sediment reverberations in doing so. We also need high-frequency contents to isolate such reverberations. In this chapter, we first assess the physical properties of the sediment layer by the H-κ staking method [*Zhu and Kanamori*, 2000]. Then, we perform RF inversion analysis to investigate deeper subsurface structure, especially the LVZ.

5.1. Receiver function data

We calculated radial RFs of OBSs, employing the ETMTC and the IWLF method with low-pass filter to 4.0 Hz. Such high frequency contents were necessary to distinguish a number of sediment reverberations. The event records employed here is the same as those used in Chapter 4, but we discarded the data from deep earthquakes which occurred around Japan to suppress variations in ray parameters among events sharing similar back azimuths.

Out of 32 OBSs, we selected five OBSs, LS02, LS03, LS05, LS09, and LS11 for the following analysis (red circles in Figure 5.1). We selected these five OBSs because they exhibit distinct and coherent positive phase at 1-2 s after the direct P-wave arrivals (Figures 5.2a-e). We consider this phase as P-to-S (Ps) conversion phase from the bottom of the sediment layer. Note that no clear phase appears before these positive phases. From this character, we assume that the sediment layer beneath these OBSs has simple structure enough to be approximated by a single flat layer. Unexpectedly, the all selected OBSs are located at northward edge of the OBS network (Figure 5.1), probably because the dipping angle of the seafloor is small and because the forearc basin does not experience severe deformation at these places [*Tsuji et al.*, 2015]. For comparison, we also show radial RFs where no such simple sediment layer is expected in Figure 5.2f, where we see no clear positive phase around 1-2 s after the direct P-wave arrivals.

In the following analyses, we set narrow back azimuth range (40° at most) for each OBS, and search for 1-D velocity structure that can best explain the observed RFs therein (black rectangles in Figure 5.2). These back azimuth ranges were chosen by trial and error so that the following H-κ stacking and inversion analyses can produce converged solutions. For the other back azimuth ranges, we could not obtain converged solutions mainly because of their insufficient SNR. We could assure two back azimuth ranges for LS11, which are helpful to valid the stability of our analysis. We refer to

these two datasets as LS11S and LS11N, hereafter (Figure 5.2e). For the other OBSs, LS02, LS03, LS05, and LS09, we could set only a single back azimuth range (Figures 5.2a-d).

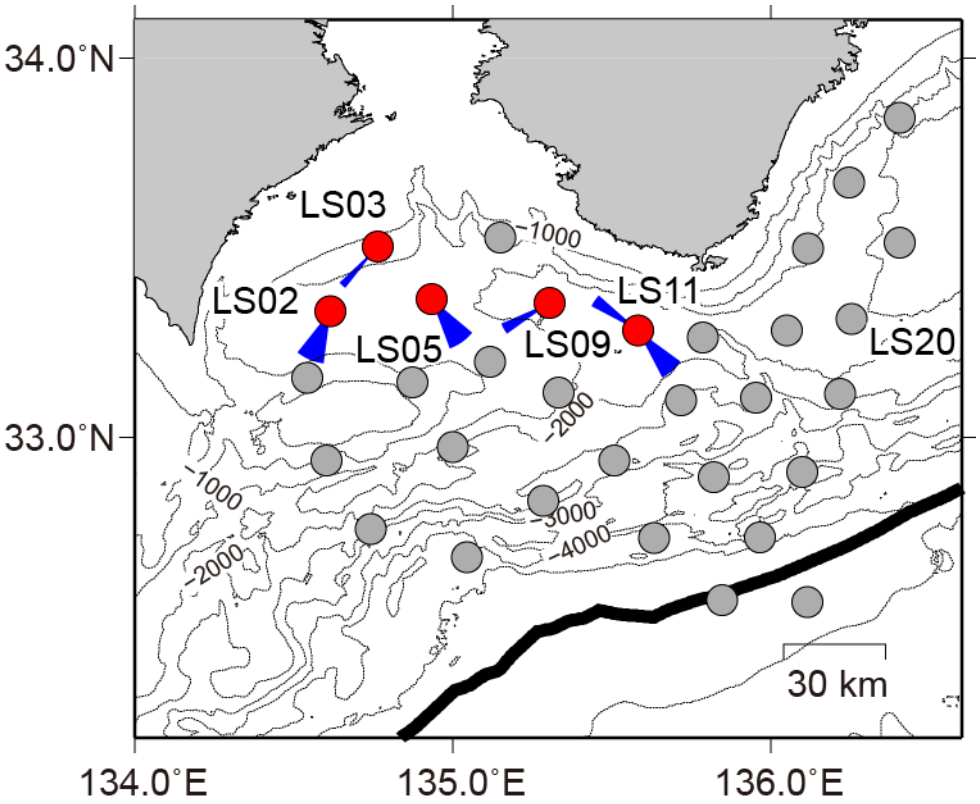

Figure 5.1. Distribution of ocean-bottom seismometers (OBSs). Five OBSs, LS02, LS03, LS05, LS09, and LS11, used for analyses in this section are shown with red. The selected back azimuth ranges for inversion analysis is represented by blue sectors. Black solid curve shows the Nankai Trough. Thin contour lines represent water depth.

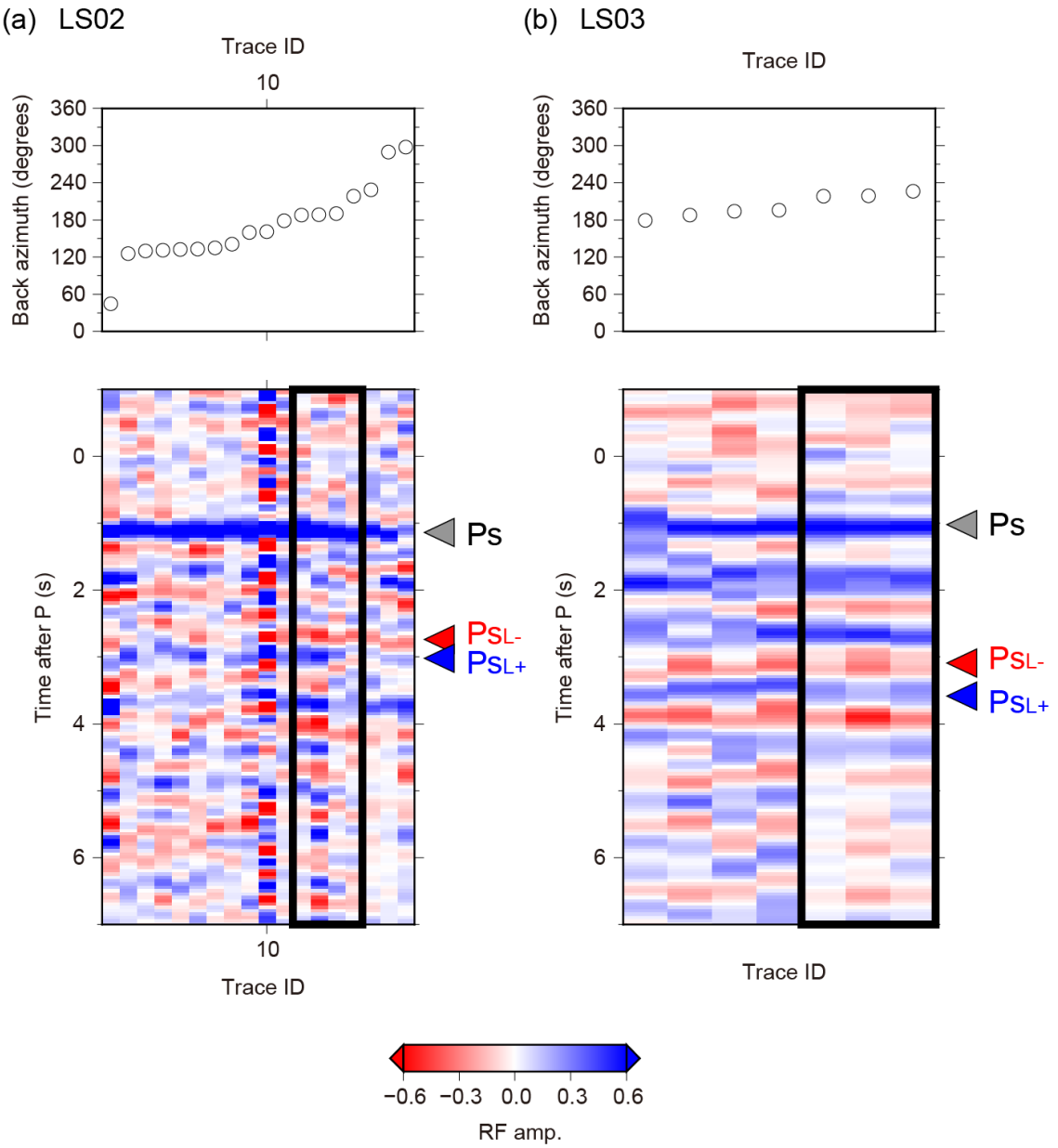

Figure 5.2. Radial receiver functions (RFs) of each ocean-bottom seismometer aligned in order of their back azimuths. Upper panels show the back azimuth of each RF. Thick black lines enclose the RFs analyzed in this section. Gray, red, and blue triangles show the delay times of P-to-S conversion phases from the bottom of the sediment layer (Ps phase), top of low-velocity zone (LVZ) along the plate interface (Ps_{L-} phase), and the bottom of the LVZ (Ps_{L+} phase), respectively.

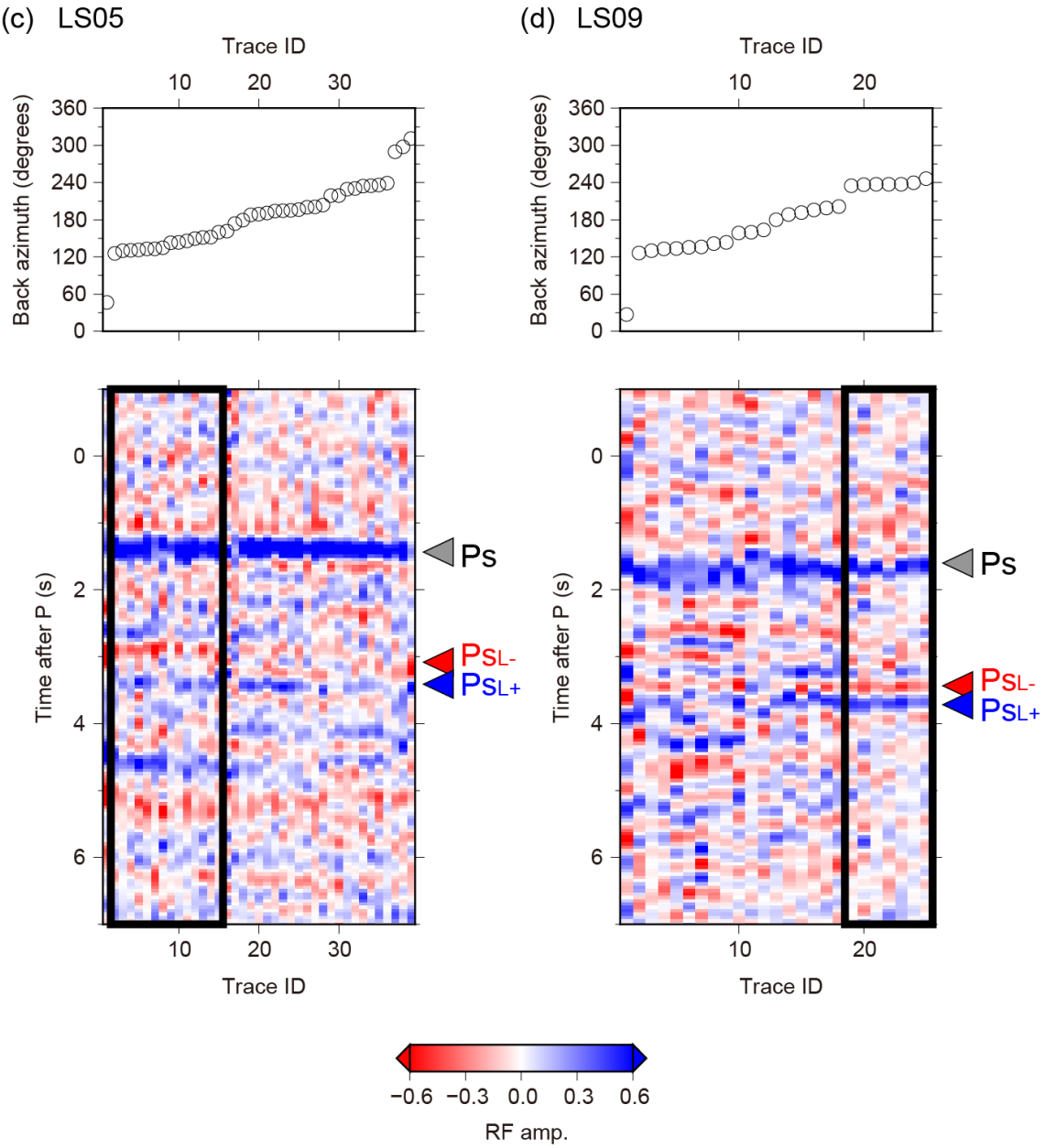

Figure 5.2. (Continued)

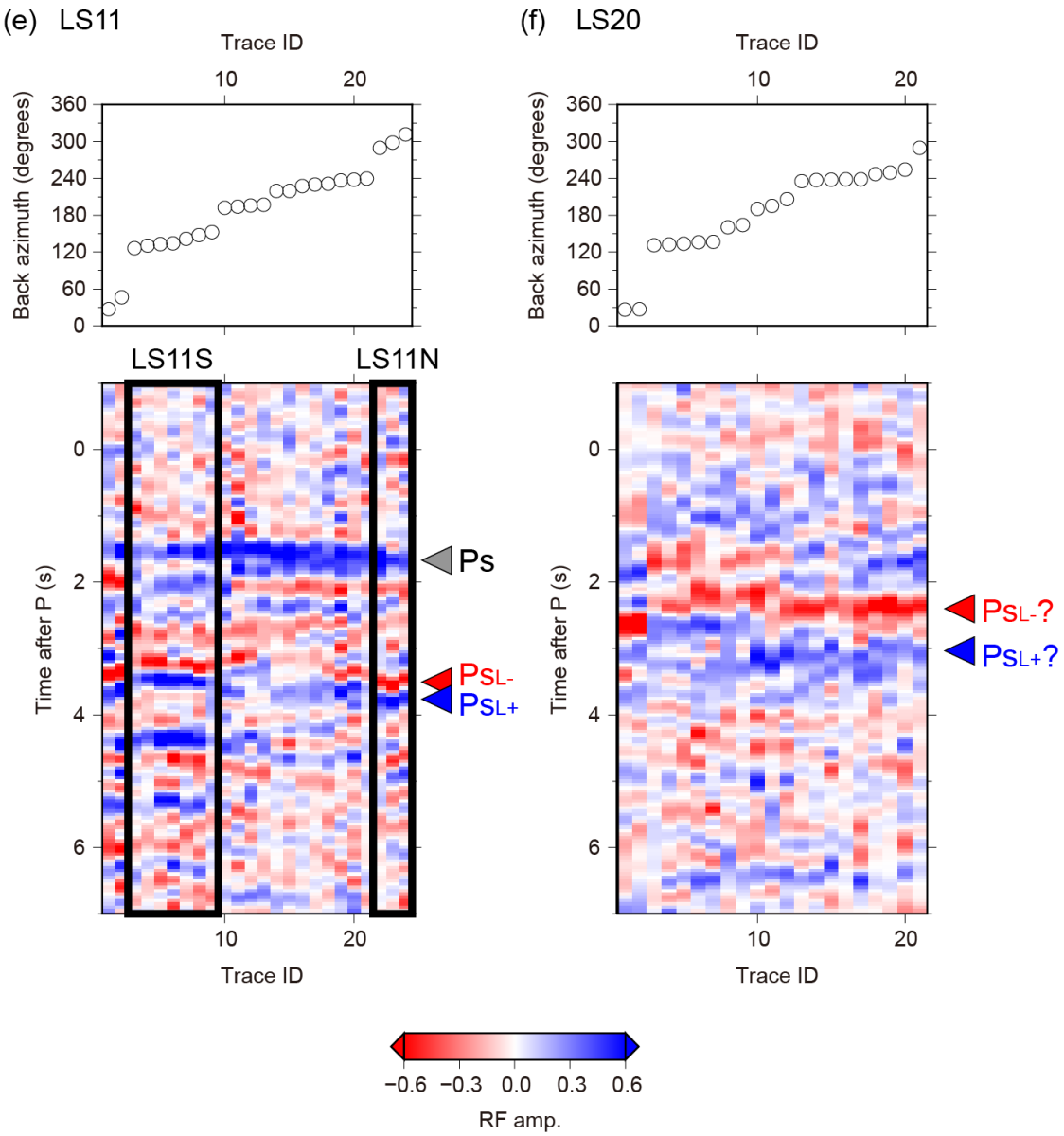

Figure 5.2. (Continued)

5.2. Estimation of sediment property by H-κ stacking method

5.2.1. Method

We performed the H-κ stacking method to investigate the properties of sediment layer beneath the seafloor. In this method, thickness (h) and Vp/Vs ratio (κ) of a homogeneous layer is determined via grid search so that theoretical timings of conversion and reflection phases can point to large RF amplitudes. Although the original method proposed by *Zhu and Kanamori* [2000] makes use of three phases, Ps, PpPs, and PpSs (or PsPs), we use additional two phases, PsSs and PpSs+w, which tend to be dominant on OBS records (see Figure 2.4 for the definition of these phase names). The delay times of these pahses from direct P-wave can be expressed as follows:

$$\Delta T_{Ps} = h\left(\sqrt{\left(\frac{\kappa}{V_P}\right)^2 - p^2} - \sqrt{\frac{1}{V_P^2} - p^2}\right),$$

$$\Delta T_{PpPs} = h\left(\sqrt{\left(\frac{\kappa}{V_P}\right)^2 - p^2} + \sqrt{\frac{1}{V_P^2} - p^2}\right),$$

$$\Delta T_{PpSs} = 2h\sqrt{\left(\frac{\kappa}{V_P}\right)^2 - p^2}, \qquad (15)$$

$$\Delta T_{PsSs} = h\left(3\sqrt{\left(\frac{\kappa}{V_P}\right)^2 - p^2} - \sqrt{\frac{1}{V_p^2} - p^2}\right),$$

and

$$\Delta T_{PpPs+w} = h\left(\sqrt{\left(\frac{\kappa}{V_P}\right)^2 - p^2} + \sqrt{\frac{1}{V_P^2} - p^2}\right) + \tau,$$

where V_P, p, and τ represent the P-wave velocity of the sediment layer, ray parameter,

and two-way travel time within the water layer, respectively. If we assume V_P to be 1.7 km/s [*e.g., Hamilton*, 1978] and fix τ value at the estimated value in Section 3.1, then only h and κ are left as unknown parameters.

Using Eq. (15), we performed grid search on h-κ space so that the following stacked amplitude could be maximum:

$$s = \sum_{i=1}^{N} \{ w_1 r_i(\Delta T_{Ps}) + w_2 r_i(\Delta T_{PpPs}) - w_3 r_i(\Delta T_{PpSs}) - w_4 r_i(\Delta T_{PsSs}) + w_5 r_i(\Delta T_{PpPs+w}) \}, \quad (16)$$

where $r_i(t)$ represents receiver function of the ith trace out of N traces, and $w_1, w_2, \ldots, w_5$ denote weighting factors assigned for each phase type. In this study, we set $w_1 = 0.4$, $w_2 = w_3 = 0.1$, and $w_4 = w_5 = 0.2$ so that phases with larger amplitudes could have more significant influences on the estimation.

5.2.2. Results and discussion

Figure 5.3 shows the summary of the H-κ stacking analysis for each OBS. We can see that the best results with the maximum stacked amplitudes well explain the peaks of RFs. The large stacked amplitudes draw a hyperbola-like curve in h-κ space, as is often the case with the H-κ stacking analysis. Although there are other local maxima out of this main curve (e.g., κ~3, h~0.7 km of LS11N), we confirmed that phase identification obviously failed in such cases. Two different datasets from a single OBS (LS11S and LS11N) produce similar results, suggesting the stability of our analysis.

The estimated thickness and Vp/Vs ratio considerably differed among OBSs: thickness ranged from ~0.5 km to ~1.1 km, and Vp/Vs ratio from ~3 to ~7. Such variations may not be surprising, considering that the separation distance of OBSs (~20

km) is larger than, or comparable at least with, the typical length scale in undulation of the sediment thickness in this region (~10 km) [*Tsuji et al.*, 2015]. A previous reflection survey identified clear reflectors at the bottom of the forearc basin in this region, and the reflectors were characterized by 0.5-2.0 s two-way traveltime from the seafloor [*Tsuji et al.*, 2015]. This two-way traveltime corresponds to 0.4-1.7 km thick if we assume its P-wave velocity to be 1.7 km/s, roughly consistent with the thickness we estimated. In addition, the estimated Vp/Vs ratio also agree with a typical value for terrigeneous sediment (Vp/Vs~2.6-13, varying with depth) [*Hamilton*, 1979]

To further evaluate our results, we computed synthetic RFs for LS11S and LS11N using three-layered model composed of water and sediment layers, and a half-space (Table 5.1). First, we calculated both radial and vertical synthetic waveforms using the reflectivity method[*Haskell*, 1953; *Kumar et al.*, 2011], and then computed radial RFs with removal of water reverberations using IWLF (red curves in Figure 5.4). We stacked observed RFs in the frequency domain, using the frequency-dependent uncertainties as weighting factors [*Park and Levin*, 2000] (black curves in Figure 5.4). In addition, we estimated standard error by the jackknife resampling method. For this error estimation, we followed the method of *Leahy and Collins* [2009] (see Appendix A for more details).

As a result, the amplitudes of the direct P-phases and later Ps and PpPs phases were generally reproduced, verifying the results of the H-κ stacking analysis. More delayed phases, PpPs+w of LS11N and PsSs of LS11S, did not show good agreement, probably because their larger delay time enhances the chance of contamination by other unmodeled phases. Around 3-4 s, observed RFs exhibited dominant negative and positive peaks which could not be explained by the synthetic RFs (shown with triangles in Figure 5.4).

We interpret these peaks as P-to-S conversion phases at the top and the bottom of LVZ located at the top of subducting plate. Hereafter, we refer to these negative and positive peaks as Ps_{L-} and Ps_{L+}, respectively. The first reason of this interpretation is that

the delay time of the negative phase corresponds to the depth of the plate interface. The second reason is that the both negative and positive peaks show sinusoidal moveout patterns in terms of event back azimuths, implying the existence of northward dipping layer (Figure 5.5). Similar negative and positive phase sets can be seen at other OBSs, though less clear than those of LS11 (Figures 5.2a-d).

Table 5.1. Parameters used in three-layered model

	Thickness	Vp (km/s)	Vs (km/s)	Density (g/cm^3)
Water layer	*1	1.5	-	1.0
Sediment layer	*2	1.7	*2	1.8
Half-space	-	*3	*3	*4

*1: OBS depth

*2: from the results of the H-κ analysis (Section 5.2)

*3: from the tomography model [*Akuhara et al.*, 2013]

*4: from the empirical relationship with P-wave velocity [*Birch*, 1961]

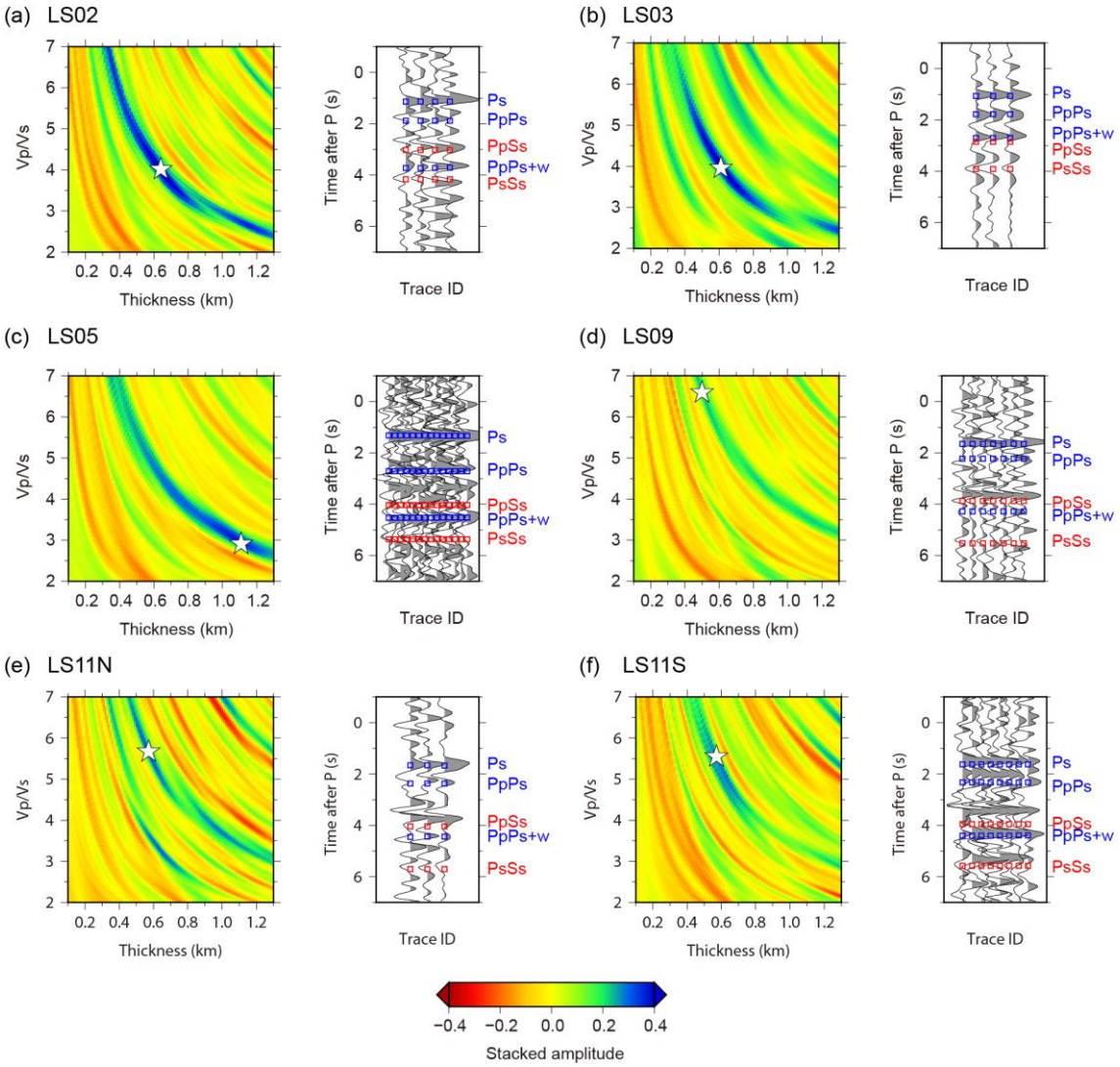

Figure 5.3. Results of H-κ stacking analysis for each station. Each left panel shows stacked receiver function (RF) amplitudes. White stars denote the best results that produce maximum stacked amplitudes. Each right panel shows observed RFs with positive amplitudes shaded. Blue and red squares denote the theoretical timings of positive and negative phases, respectively, corresponding to the best results. The phase names used here were defined in Figure 2.4.

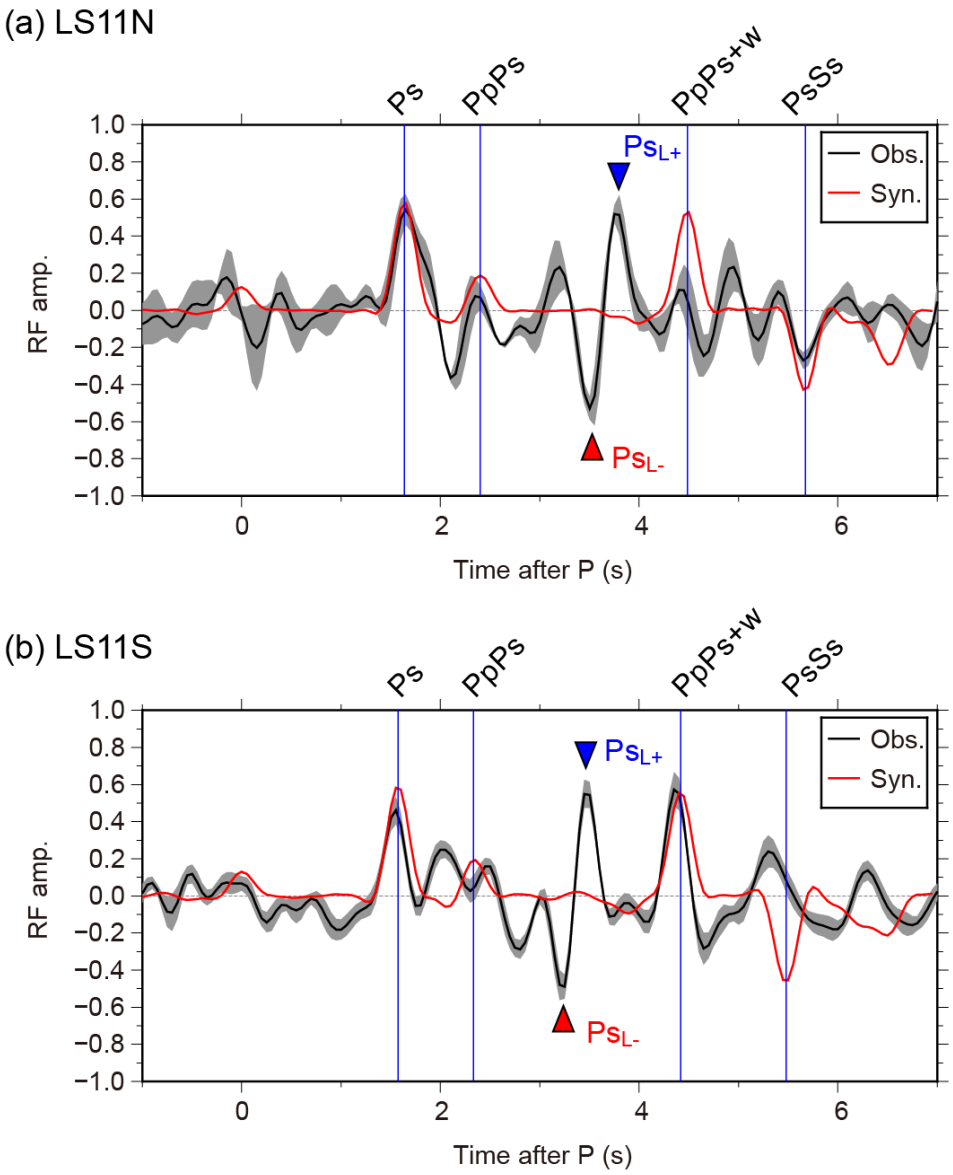

Figure 5.4. Synthetic (red) and stacked observed (black) receiver fucntions (RFs) calculated with the three-layered models for (a) LS11N and (b) LS11S. Gray shaded zone represent standard errors of the stacked RFs. Blue vertical bars indicate the delay times of major phases predicted from the best-fit results of the H-κ stacking analysis. The phase names are the same as Figure 2.4b. Red and blue triangles indicate dominant negative and positive phases, which cannot be explained well by the three-layered model.

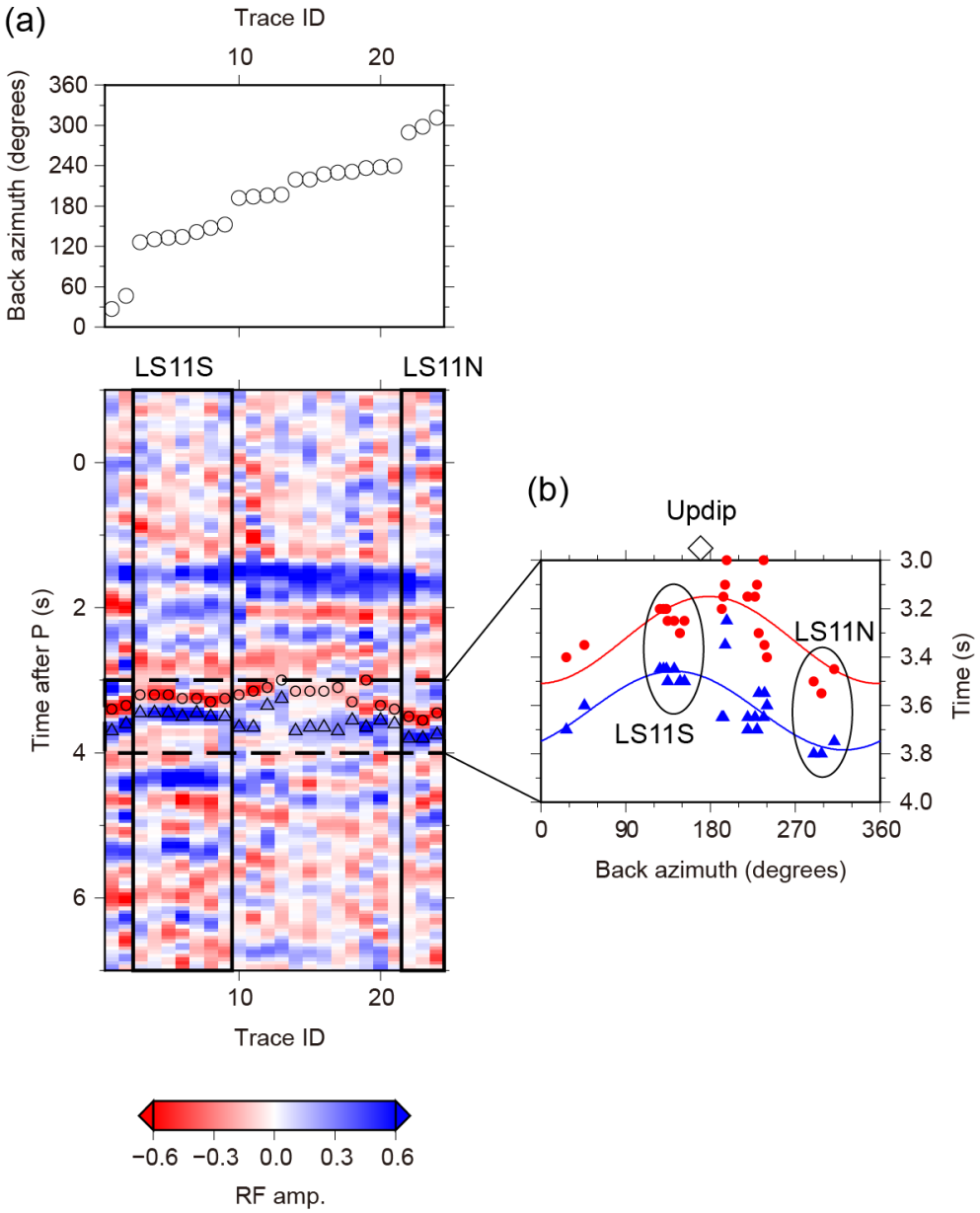

Figure 5.5. (a) The same as Figure 5.2e but the negative and positive peaks showing moveout are marked with circles and triangles, respectively. (b) Delay times of the marked negative (red circles) and positive peaks (blue triangles) are plotted with sinusoidal fitting curves. Diamond represent the updip direction of the subducting Philippine Sea plate beneath LS11 inferred from the 3-D geometry model of the subducting Philippine Sea plate (Chapter 4).

5.3. Receiver function inversion

5.3.1. Model parameters

Our inversion aims to search for the 1-D layered structure model which can best predict observed RFs including higher frequencies up to 4 Hz. To fully describe arbitrary 1-D velocity models, we need to know thickness (h), density (ρ), and P- and S-wave velocities (V_P and V_S) of each layer. For each OBS, we assumed 1-D layered structure composed of five homogeneous layers and a half space which represent the seawater, sediment, overriding plate, LVZ along the plate interface, oceanic crust, and oceanic mantle, from top to bottom (Figure 5.6). In the followings, we describe the detailed setting of model parameters for each layer. Basically, our setting for model parameters intended to widen search ranges of parameters for the LVZ and to restrict search ranges of the other parameters using prior information. Such restricted search ranges were necessary to overcome the non-uniqueness of RF inversion [e.g., *Ammon et al.*, 1990].

<Water layer>

The P-wave velocity and density were fixed at typical values (V_P=1.5 km/s and ρ=1.0 g/cm^3), and the thickness was fixed to be OBS depth. No unknown parameter was assigned to this layer.

<Sediment layer>

All parameters ($h, V_P, V_S,$ and ρ) were fixed at the values which had been used or estimated by the H-κ stacking analysis (Chapter 5.2). No unknown parameter was assigned to this layer.

<Overriding plate and oceanic crust layers>

We set bottom depth (z_1 and z_2 in Figure 5.6) and V_P/V_S ratio (κ_1 and κ_2 in

Figure 5.6) of these layers as unknown parameters. The search range of the bottom depth were $\pm$2 km width around the depth of the plate interface and the oceanic Moho which we estimated in Chapter 4, and the search ranges of Vp/Vs ratio were from 1.6 to 1.8 for the overriding plate and from 1.6 to 2.0 for the oceanic crust. However, we slightly adjusted these search ranges if the result did not show good fit for either Ps_{L-} or Ps_{L+} phases. We extracted P-wave velocity from the tomography model [*Akuhara et al.*, 2013]. In addition, we calculated density using empirical relationship to P-wave velocity [*Birch*, 1961] as follows:

$$\rho = 0.328V_P + 0.613 \tag{17}$$

<LVZ layer>

We embedded this LVZ layer at the top of the oceanic crust layer. We assigned three unknown parameters, δ_h, δ_{V_P}, and δ_{V_S} to this layer, which represent the percentage of thickness and P- and S-wave velocities of this layer relative to those of the oceanic crust layer, respectively. That is, the absolute thickness and P- and S-wave velocities of this layer is given by $\delta_h(\mathrm{z}_2 - \mathrm{z}_1)$, $\delta_{V_P}V_{P_c}$, and $\delta_{V_S}\kappa_2 V_{P_c}$, respectively, where V_{P_c} represent P-wave velocity of the oceanic crust (Figure 5.6). Their search ranges were 0.0-0.7 for δ_h and 0.1-0.7 for δ_{V_P} and δ_{V_S}. In some cases, however, we were forced to limit the search range of Δh to avoid unlikely results such as thickened LVZ (>5 km) with extremely low velocity (ΔV_S~1 km/s). Density was calculated by using the empirical relationship to P-wave velocity [*Birch*, 1961].

<Oceanic mantle layer>

All parameters were fixed at typical values (V_P=8.1 km/s, V_S=4.7 km/s, and ρ=3.4 g/cm^3).

5.3.2. Inversion scheme

To search for optimized parameter set, we employed the neighborhood algorithm [*Sambridge*, 1999]. The algorithm first randomly generates N_s samples in the multi-dimensional parameter space, and evaluates misfit values of these samples. At every iteration step, the algorithm selects top N_r samples with the lowest misfit values out of all samples so far generated. Then, new N_s/N_r samples are randomly generated around each of the selected samples. This random sampling is executed with random walk within a Voronoi cell whose centroid is located at the selected sampling point (see *Sambridge* [1999] for more detailes). This procedure is repeated until the solution is converged. In this study, we set $N_s = 40$ and $N_r = 20$, and the process were repeated 800 times, so 32,000 models were evaluated in total.

We defined the misfit values using cross-correlation coefficients as follows:

$$misfit = 1 - \sum_t \frac{u_{syn}(t) \cdot u_{obs}(t)}{\sqrt{u_{syn}^2(t)} \cdot \sqrt{u_{obs}^2(t)}} \tag{18}$$

where u_{syn}, u_{obs}, represent synthetic and observed RFs, and their sampling interval, respectively. We used 8-s-long time windows starting 1 s before the direct P-wave arrival to the misfit measurements. This window length were chosen so that the PsSs phase could be included. The observed and synthetic RFs were stacked and computed, respectively, in the same way as described in Section 5.2.2.

5.3.3. Results

Figure 5.7 shows the results of LS11S and LS11N, where we can see great improvement in waveform fitting from what is shown in Figure 5.4 in spite of the tight constraints imposed on our inversion. Note that we obtained good fits for Ps_{L-} and Ps_{L+} phases. As expected, these phases can be explained by the P-to-S conversion phases at

both sides of the LVZ around the plate interface. In addition, we can see good reproducibility about the other phases such as Ps, PpPs, PsPs+w, PsSs, and P-to-S conversion phase from the oceanic Moho (Ps_M). The results show that the LVZ is characterized by considerably low velocity and thin thickness (V_P=2.3 km/s, V_S=1.2 km/s and h= 0.8 km for LS11N, and V_P=1.9 km/s, V_S=1.4 km/s and h= 1.2 km for LS11S).

To confirm the reliability of such a thin LVZ, we checked the distribution of misfit values which had been evaluated for all sampled models during the inversion. We divided these misfit values into bins based on V_P, V_S and h values of the LVZ layer and displayed the minimum value of each bin (lower panels of Figures 5.7a and b). From the figure, we judged that the velocities and thickness of the LVZ were well constrained; we will discuss what contributes to such good constrains later in detail. We defined the confidential regions of these estimated values from these misfit value distributions so that the region could include all misfit values less than 1.2 times of the minimum misfit value.

The results of other OBSs, LS02, LS03, LS05, and LS09, show similar thin low-velocity layer around the plate interface, although there are some variations in their thickness and velocities (Figures 5.8 and 5.9). The averaged P- and S-wave velocities and thickness among all OBSs were ~3 km/s, ~2 km/s, and ~2 km, respectively (Figure 5.10). Although we did not directly solve for the Vp/Vs ratio of the LVZ, its averaged value marked 1.5 with considerable large uncertainties. Roughly speaking, OBSs in the east tend to exhibit low velocities.

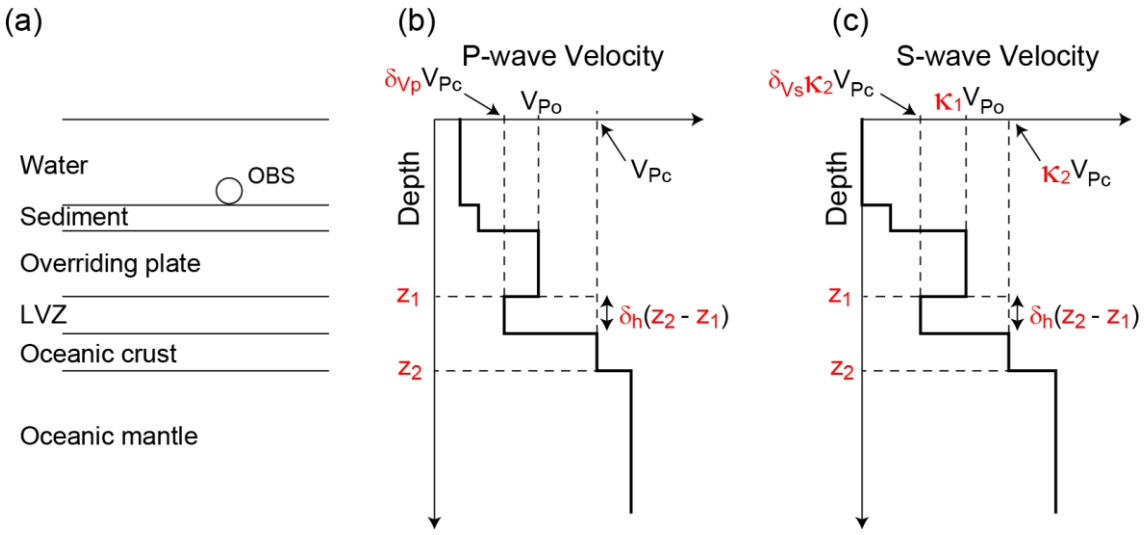

Figure 5.6 Schematic illustration of layered structure with depth-velocity diagrams. Seven parameters shown with red colors (z_1, z_2, κ_1, κ_2, δ_h, δ_{V_P}, and δ_{V_S}) are model parameters of our inversion analysis. The other parameters were fixed by using prior information. P-wave velocities of the overriding plate and the oceanic crust are denoted by V_{P_o} and V_{P_c}, respectively. Note that P- and S-wave velocities and thickness of the low-velocity zone are represented by $\delta_{V_P}V_{P_c}$, $\delta_{V_S}\kappa_2 V_{P_c}$, and $\delta_h(z_1 - z_2)$, respectively.

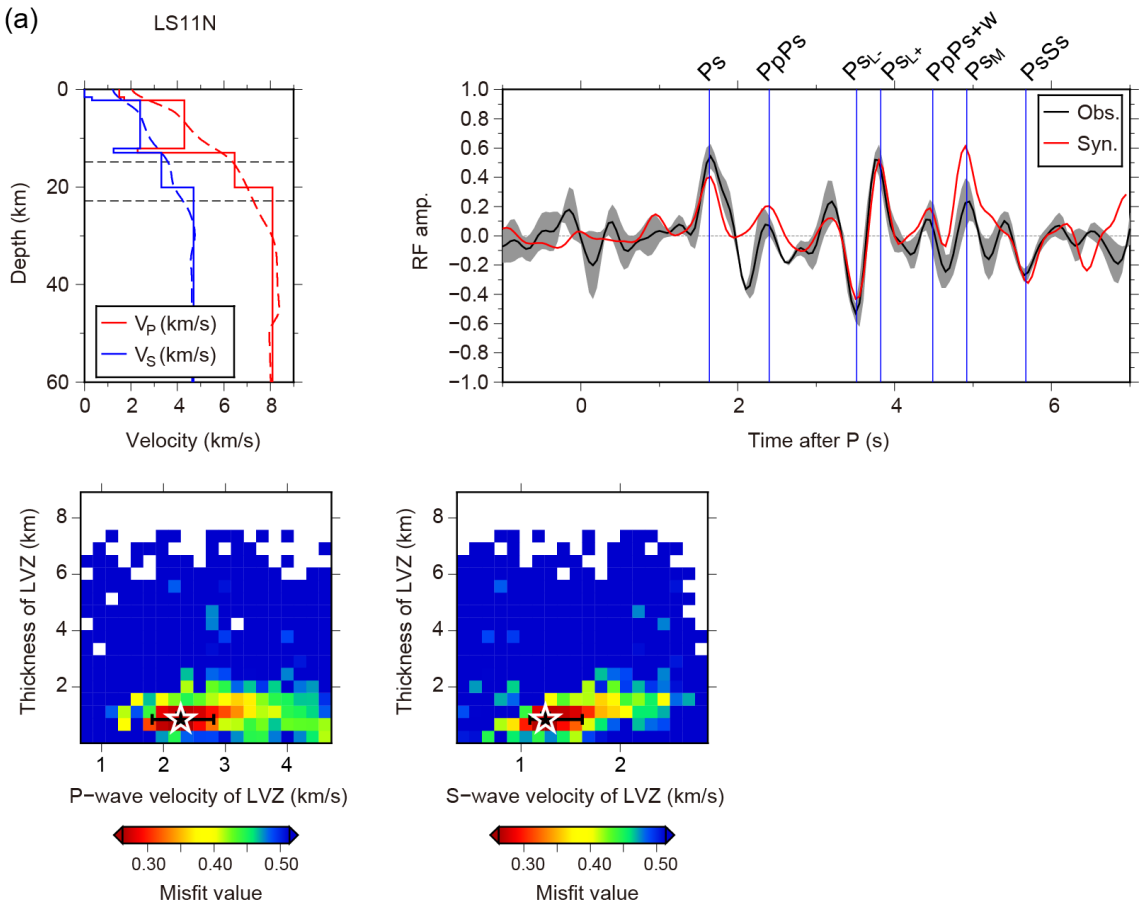

Figure 5.7. Results of receiver function (RF) inversion for (a) LS11N and (b) LS11S. Upper left panel shows the resultant best-fit velocity models (solid lines) and the previous tomography models (dashed curves) [*Akuhara et al.*, 2013]. Dashed horizontal lines denote the depth of plate interface and the oceanic Moho determined in Chapter 4. Upper right panel shows observed (black) and synthetic RFs (red). Blue vertical lines denote predicted arrivals of major phases. The other notations in this panel is the same as Figure 5.4. Lower panels show misfit value distributions binned by parameters of low-velocity zone (LVZ). White stars represent the best-fit model with confidential regions represented by black bars.

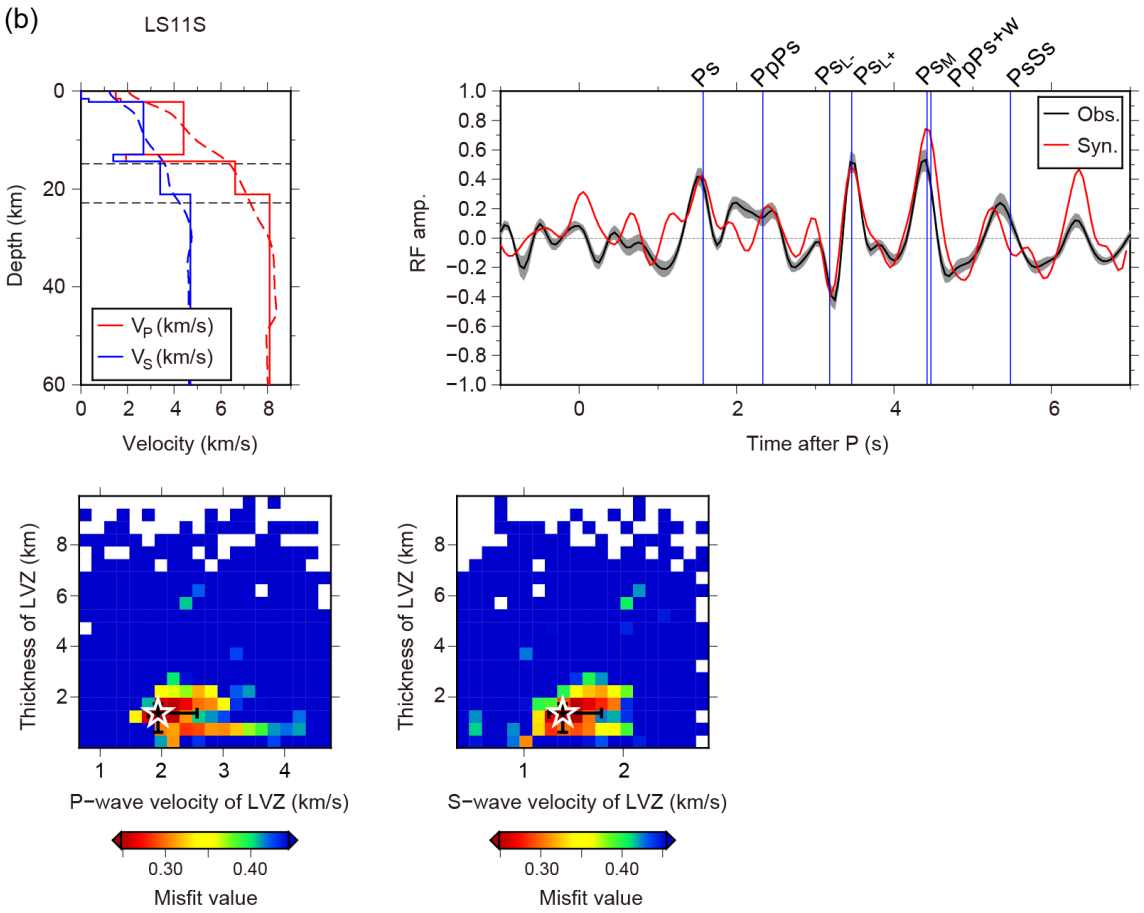

Figure 5.7. (Continued)

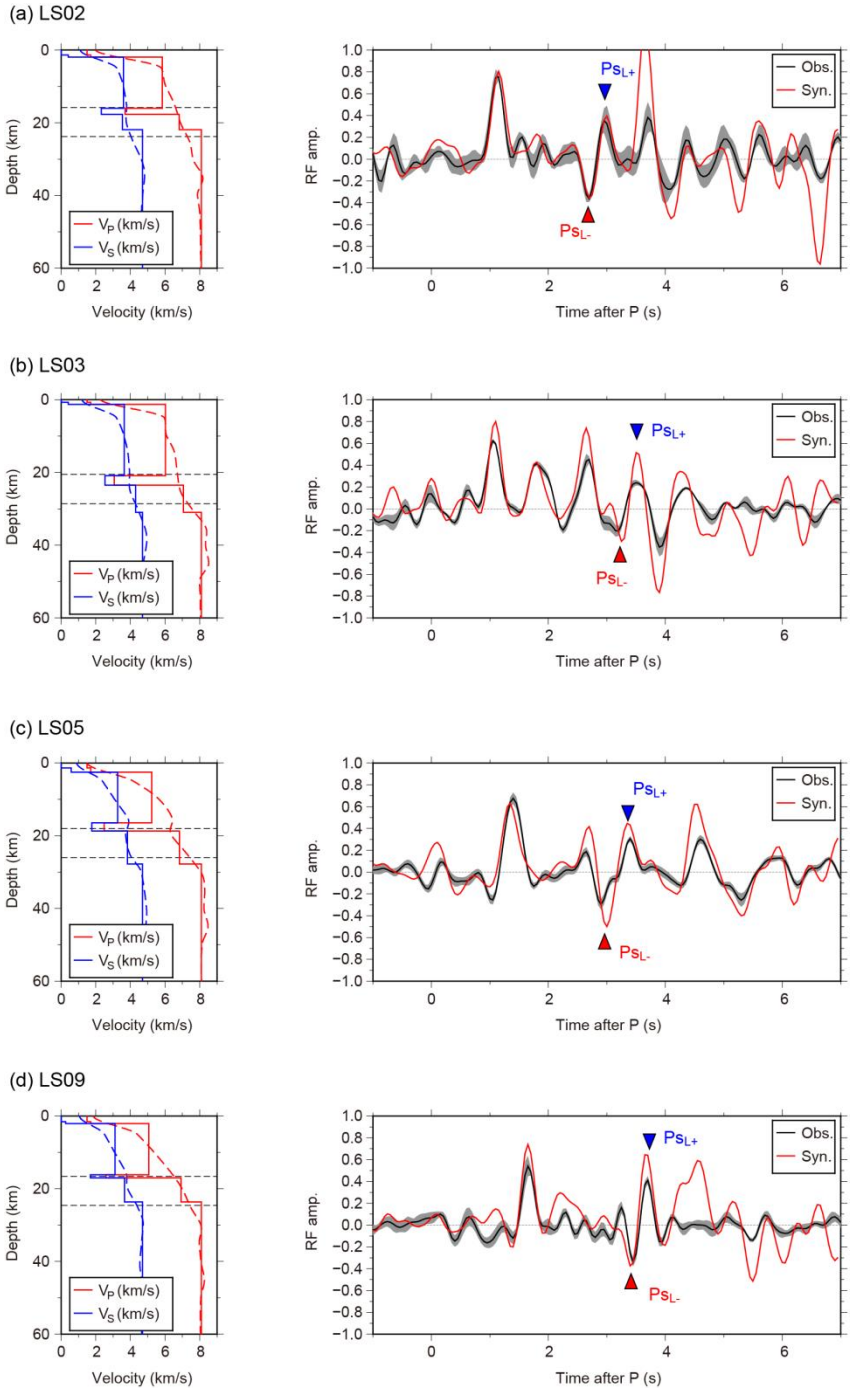

Figure 5.8. Best-fit models and synthetic and observed receiver functions for (a) LS02, (b) LS03, (c) LS05, and (d) LS09. The notations are the same as Figure 5.7. Red and blue triangles indicate Ps_{L-} and Ps_{L+} phases, respectively.

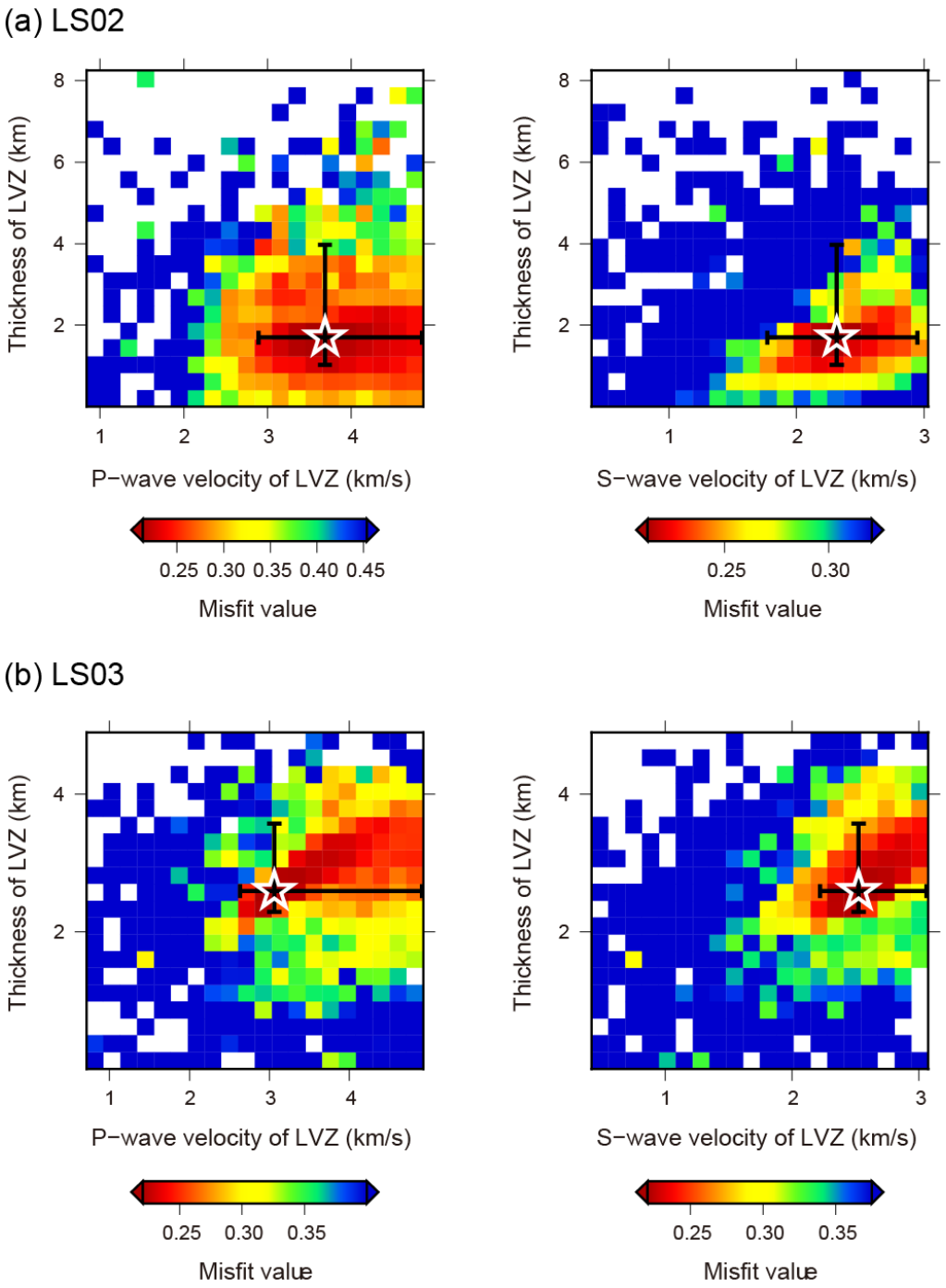

Figure 5.9. Misfit value distributions binned by parameters of low-velocity zone. The notations are the same as the lower panels of Figure 5.7. Note that the scales are different among OBSs.

(c) LS05

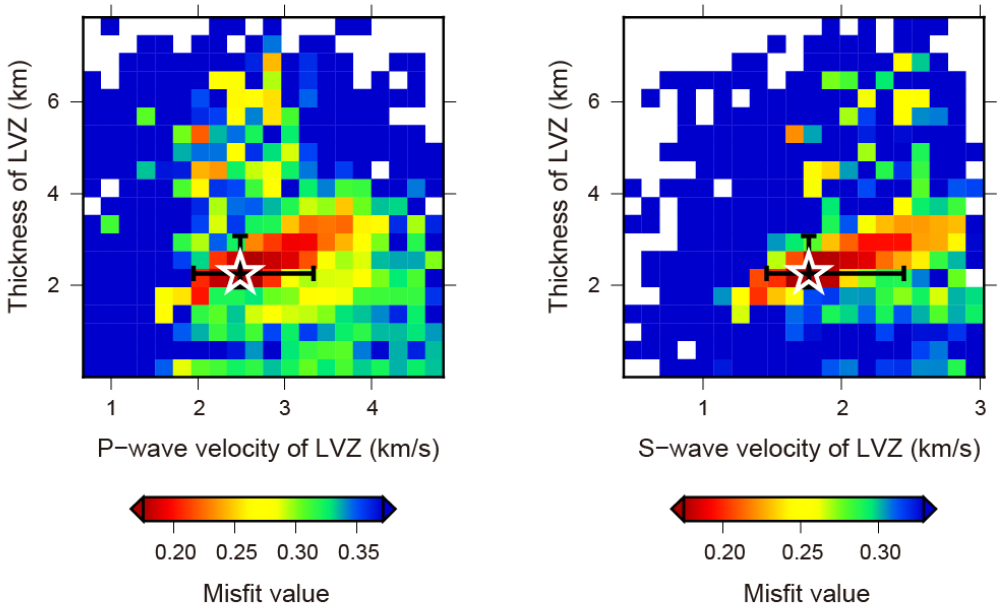

(d) LS09

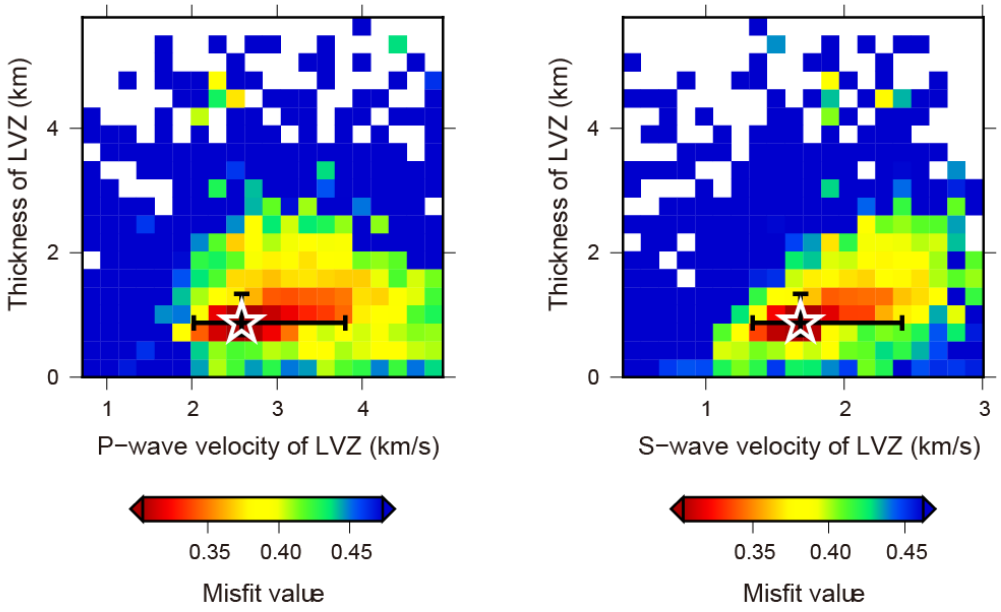

Figure 5.9. (Continued)

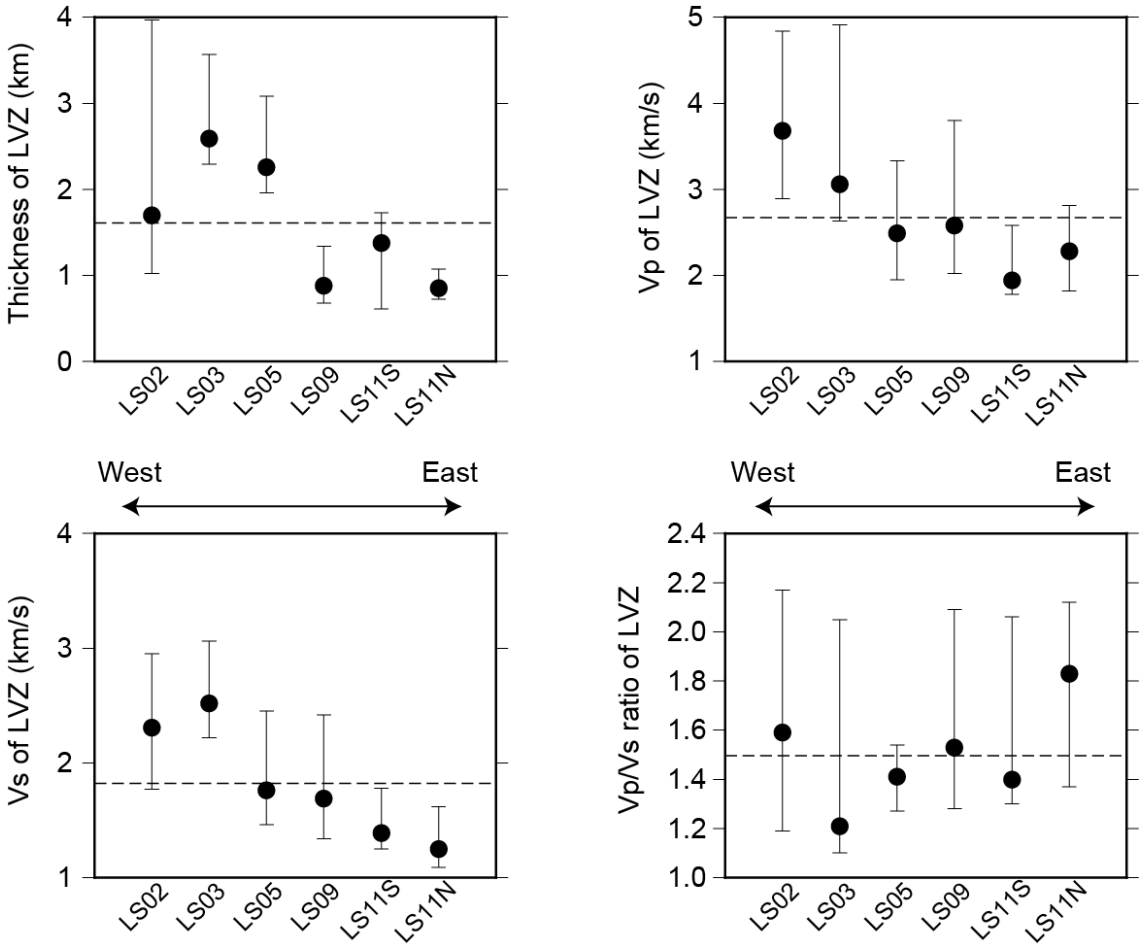

Figure 5.10. Summary of the estimated parameters for low-velocity zone. In each panel, horizontal dashed line shows averaged value of all OBSs. The OBSs listed on horizontal axis is sorted by their locations: OBSs in the west appear on the left side of these panels.

5.4. Discussion

5.4.1. How does inversion analysis constrain parameters of low-velocity zone?

In general, RF amplitude of the P-to-S conversion phase is significantly sensitive to S-wave velocity contrast [*Julià*, 2007]. In addition, the time interval of two P-to-S conversion phases is sensitive to Vp/Vs ratio (especially to S-wave velocity) and layer thickness [*Zhu and Kanamori*, 2000]. In our case, the amplitudes of Ps_{L-} and Ps_{L+} phases may put constraints on S-wave velocity of the LVZ, and a tradeoff between its thickness and P-wave velocity seems to remain. Nevertheless, our results show well-constrained P- and S-waves velocities and thickness. It is worth clarifying what constrains the P-wave velocity.

Before addressing this issue, we reexamined the stability of our results in more strict way. We repeated the inversion for LS11N by fixing the parameters except for the LVZ layer at values of the best-fit result, and widen the search range of the parameters for the LVZ layer (0.0-1.0 for δ_h, δ_{V_P}, and δ_{V_S}). Moreover, we repeated this modified inversion ten times to increase the number of sampled models. We finally obtained 320,000 models by this process, which increased the chance of detecting other local maxima. As a result, the misfit value distributions still showed well-constrained feature (Figure 5.11), so we concluded that the results of the inversion was robust and it constrained these parameters truly for some reasons.

To investigate the reason, we calculated synthetic RFs of LS11N by changing the P-wave velocity (and density which were scaled to the P-wave velocity) of the LVZ from the best-fit result, and measured maximum amplitudes around the Ps_{L-}, Ps_{L+}, PpPs+w, and Ps_M phases. We found that these amplitudes varied significantly in response to the changes of P-wave velocity and density, contrary to our expectations (Figure 5.12). We recognized that this is in part due to hidden multiple reflections within the LVZ (phases A–D in Figure 5.13). Three of these four phases includes P-to-P

reflection, so their amplitudes are sensitive to both P-wave velocity and density. This sensitivity should aid to constrain the P-wave velocity and density of the LVZ in our inversion problem. We show a synthetic RF calculated with a three-layered model consisted of water, sediment layers, and a half space, for comparison (green curve in Figure 5.12a). We can see that the genuine amplitude of the PpPs+w phase, which appears in the case of the three-layered model, is larger than that of the best-fit model. We consider that this amplitude reduction is a consequence of the overlapping reflection phases A and/or B.

It may not be clear why Ps_{L-} phase is also affected by the P-wave velocity change despite this phase is apart in time from the reflection phases A-D (see Figure 5.12a). In decreasing the P-wave velocity of the LVZ, the maximum amplitude of the Ps_{L-} phase was constant at high P-wave velocity, but suddenly decreased below V_P=2.2 km/s (red circles in Figure 5.12b). We consider that this sudden decrease is attributed to the interference from the following Ps_{L+} phase which occurs in the presence of extremely thin LVZ. We show theoretical time interval between Ps_{L-} and Ps_{L+} phases and the amplitude of Ps_{L-} phase together in Figure 5.14. From this figure, it is shown that such interference occur if the time interval become smaller than 0.3 s, which is fairly reasonable for the frequency range employed here (< 4 Hz). This phenomena may also contribute to constraining the P-wave velocity of the LVZ.

To summarize this section, our inversion problem can constrain not only S-wave velocity of the LVZ, but also its P-wave velocity and density with the aid of hidden reflection phases. In this situation, time interval between Ps_{L-} and Ps_{L+} phases will determine the thickness of the LVZ.

5.4.2. Possible interpretations of low-velocity zone

As we have seen, we revealed that a LVZ (V_P~3 km/s, V_S~2 km/s, and ~2 km thick in average) along the plate interface beneath offshore region at seismogenic zone

depth. Obviously, its thickness is much thinner to be interpreted as the whole oceanic crust. One possible explanation for this LVZ is the hydrated oceanic crust Layer 2 (i.e., pillow basalts and sheeted dikes), whose typical thickness and P-wave velocity has been reported to be ~1-2 km and ~5 km/s, respectively, before subduction [*Christensen and Salisbury*, 1975]. The estimated P-wave velocity in this study is much lower than this typical velocity, suggesting that the LVZ must be hydrated considerably. In this case, major source of fluid is considered to be progressive dehydration of the oceanic crust as we stated in Chapter 4. This interpretation agrees with that of *Hansen et al.* [2012], who investigated the property of similar LVZ beneath the land area of the Cascadia subduction zone by RF analysis. They estimated the Vp/Vs ratio of the LVZ to be 2.8 on average, which is corresponding to ~2 km/s of S-wave velocity with the assumption of the typical P-wave velocity. Their estimated thickness was 3.4 km on average, somewhat thicker than that of our study. However, we must be careful whether this difference is true or not because there should be a systematic difference between these two estimations due to the difference in analysis methods (e.g., the treatment of dip angle and P-wave velocity).

Another possible interpretation is that the LVZ reflects subducting sediment located above the oceanic crust. Subducting sediment have been well identified in the Kumano region, east and outside of our study area, continuing in down-dip direction to about 10 km depth at least [e.g., *Moore et al.*, 2009]. The thickness of the subducting sediment has been estimated to be 1-2 km and is considered to be fluid-rich and unconsolidated [*Bangs et al.*, 2009; *Tsuji et al.*, 2014]. Its P-wave velocity has been estimated to be 1.8-2.6 km/s from core sample measurements at 5 km depth [e.g., *Hoffman and Tobin*, 2004]. Although there is no conclusive evidence for the existence of such a sediment layer at the place where we identified the LVZ (15-20 km depth), *Kodaira et al.* [2002] has inferred its existence from the intense amplitudes of reflection phases at similar depth off the Eastern Shikoku. They have roughly estimated the

P-wave velocity of the sediment layer to be ~3 km/s, which agrees with our estimation.

We must be aware of systematic biases imposed on our estimations. The great assumption we used is the 1-D layered structure without any dipping interface. Under the existence of a dipping layer, both RF amplitudes and phase onsets vary with their event back azimuths sinusoidally with period 2π. Other systematic biases might originate from attenuation structures, imperfectly-welded interfaces [e.g., *Schoenberg*, 1980], and incorrectness of the empirical relation between density and P-wave velocity, and attenuation effects. All of them have potential to affect RF amplitudes of Ps_{L+} and Ps_{L-} phases directly, or indirectly through the amplitudes of reflected phases (phases A-D in Figure 5.13). We presume that such systematic biases are responsible of extremely low Vp/Vs ratio which is somewhat difficult to be interpreted.

Trapped fluid, or high reflectivity which has potential to be interpreted as fluid, along the plate interface of seismogenic zone is becoming a popular observation in many subduction zones in the world [*Husen and Kissling*, 2001; *Kodaira et al.*, 2002; *Nedimović et al.*, 2003; *Mochizuki et al.*, 2005; *Bell et al.*, 2010; *Li et al.*, 2015]. Such fluid-rich layer has been considered to influence the rupture propagation of the megathrust earthquakes and been investigated by mainly active source surveys. Our study provides additional way to investigate the detailed properties of the plate interface which can constrain S-wave velocity and potentially anisotropic structure. By promoting this new-type survey and combining their results with those from active source surveys, we should acquire advanced knowledge about the physical properties of subducting plate interface.

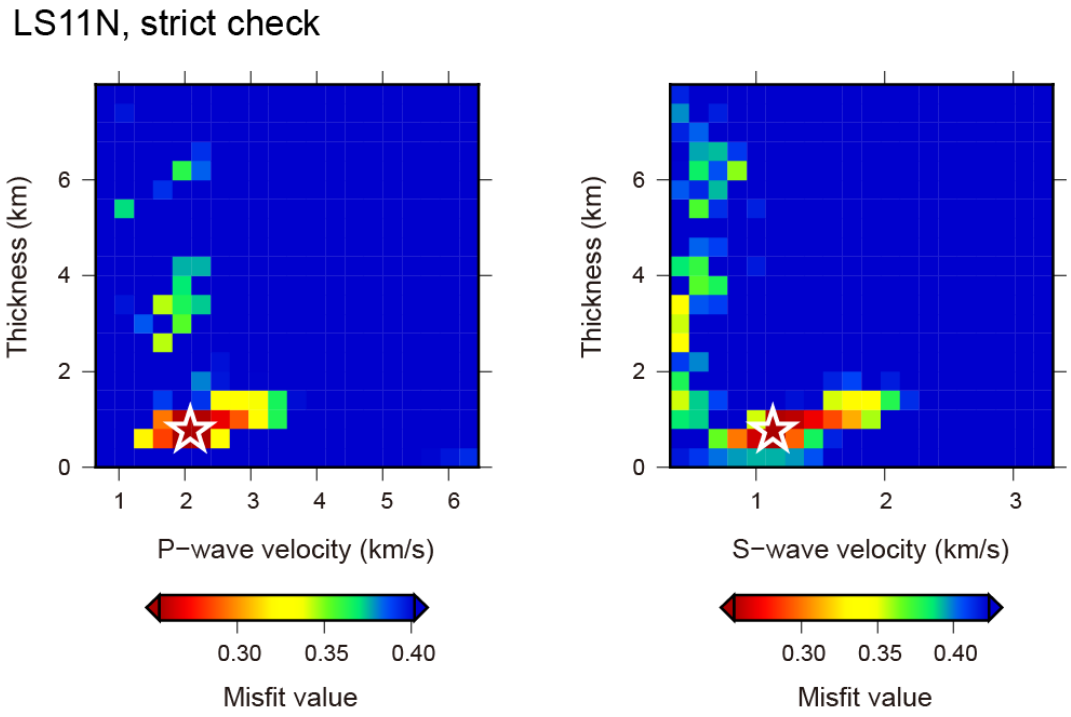

Figure 5.11. Misfit value distributions for LS11N. These distributions were obtained from the results of 10 inversions to increase the number of sampled models. In addition, the inversions solved only parameters of low-velocity zone for larger search ranges. The other parameters were fixed at the values of the best-fit result. All notations are the same as Figure 5.9.

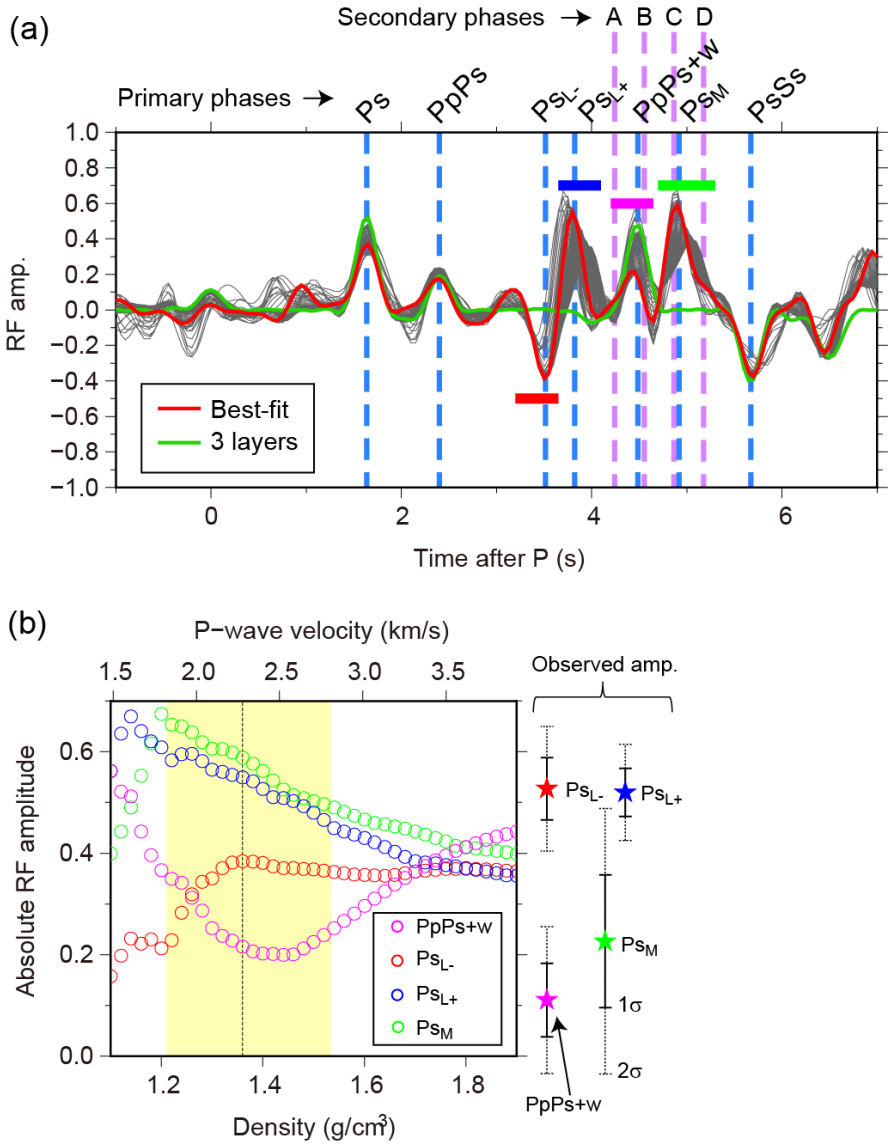

Figure 5.12. (a) Synthetic receiver functions (RFs) obtained by changing the P-wave velocity (and density) of the LVZ for LS11N (gray curves). Red curve denote the original best-fit result. Green curve is synthetic RF of three-layered model. Colored horizontal bars denote time windows to measure the maximum amplitudes plotted in Figure 5.12b. Arrivals of later phases are indicated by dashed lines. (b) Maximum RF amplitudes around Ps, Ps_{L-}, Ps_{L+}, and Ps_M phases. Dotted vertical line indicates the P-wave velocity of the best-fit result, and yellow-shaded area represent its uncertainty. Stars appearing on the right side of the panel denote observed amplitudes.

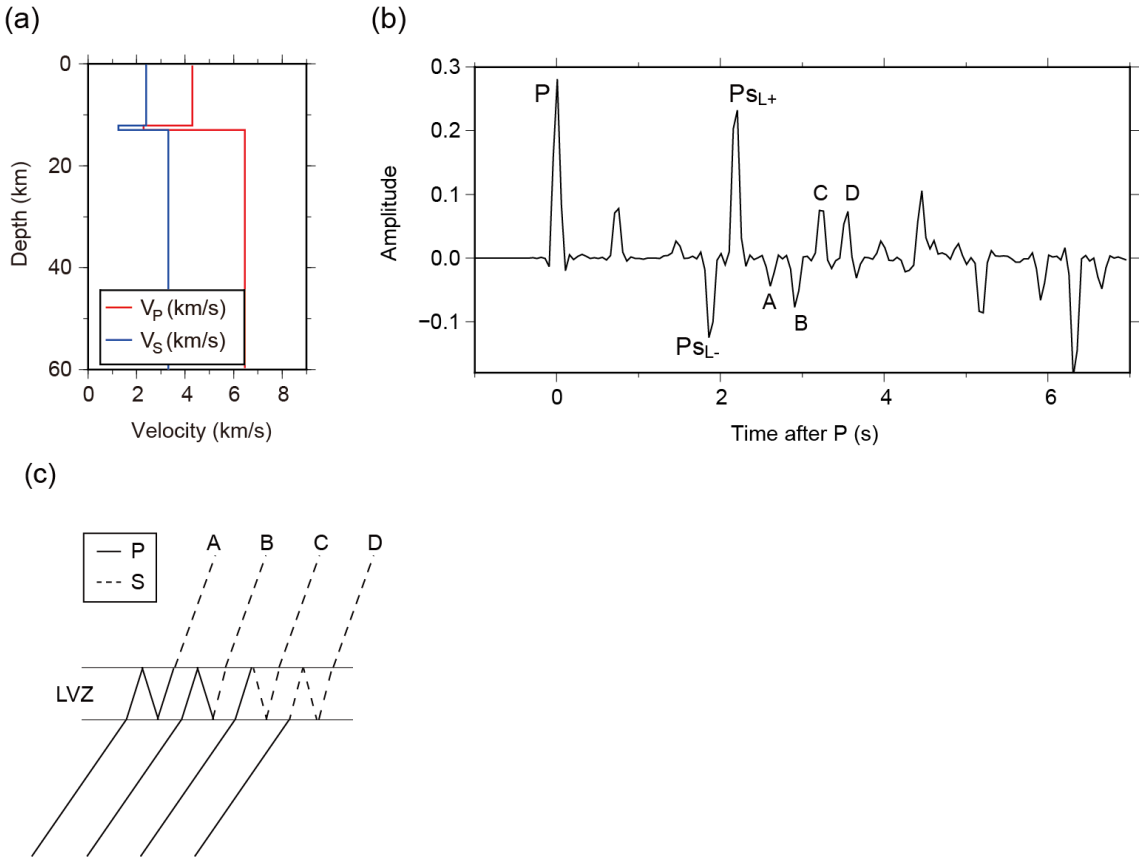

Figure 5.13. Impulse response of radial component to low-velocity zone. (a) P- and S-wave velocity models employed for synthetic calculations. (b) Synthetic impulse response of radial component. (c) Schematic illustration of secondary phases reverberated within the LVZ.

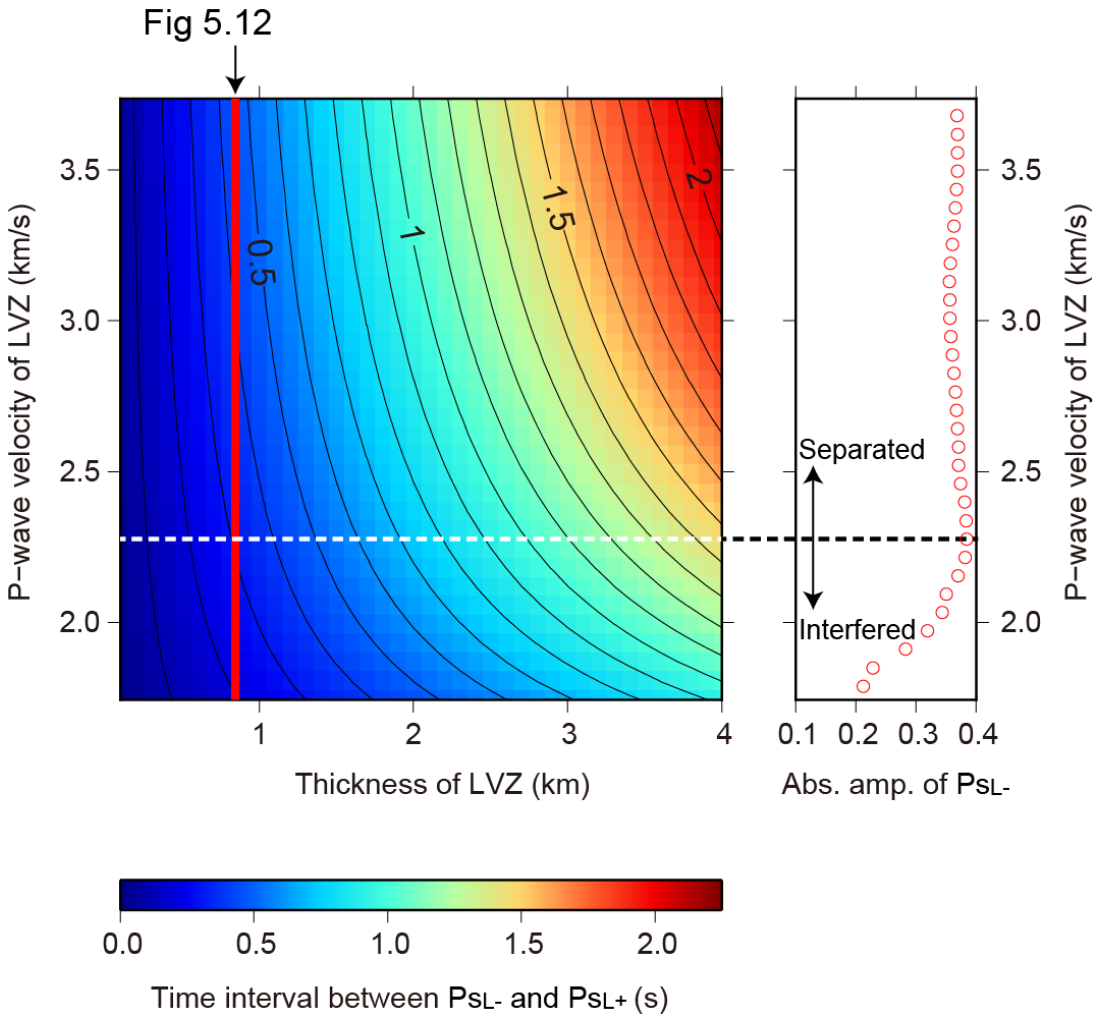

Figure 5.14. Left panel shows synthetic time interval between Ps_{L-} and Ps_{L+} phases. We calculated this intervals by changing the thickness and P-wave velocity of low-velocity zone of the best-fit result of LS11N. Absolute amplitudes of Ps_{L-} phase (right panel) were estimated along the thick red line in the left panel.

6. General Discussion

6.1. Variation in low-velocity zone thickness along-dip direction

So far we have investigated hydrous state of the Philippine Sea plate using two different methods: RF imaging (Chapter 4) and RF inversion (Chapter 5). The major advantage of the imaging method is its relatively easy application. Though this method, we acquired intuitive insight about the geometry of the subducting structure and its hydrous state with only moderate quality control of the observed data. However, the imaging methods may not put strict constraints on the LVZ properties, due to the lack in high-frequency contents, contamination by free surface multiples, and errors in the reference velocity model. Especially, problems of underestimating the LVZ thickness due to smoothed reference velocity model has been ignored until recently. This problem has been drawing more attention since pointed out by *Audet et al.* [2009] and its related studies [e.g., *Hansen et al.*, 2012; *Bostock*, 2013].

Our RF imaging identified an 8 km thick LVZ extending widely beneath both the onshore and offshore regions. This results, however, should be tested using another method more independent from the tomography model. That is because the tomography model we used in this study has smooth velocity change in depth, which probably leads to the underestimation of low-velocity anomaly. In addition to our study, quite a few studies have been conducted RF analysis in southwestern Japan [e.g., *Shiomi et al.*, 2008; *Kato et al.*, 2014], and they also employed smooth velocity models. We, therefore, consider that the accurate thickness of the LVZ beneath southwestern Japan still requires further investigations. Our RF inversion analysis, in this sense, provided more accurate LVZ thickness (~2 km) at the specific part of the southwestern Japan subduction zone. Here, we does not consider that this thickness is constant throughout the entire subduction zone. In fact, *Nedimović et al.* [2003] has reported that the LVZ

thickness increases as the slab subducts deeper in the Cascadia subduction zone.

We may barely recognize the spatial variation of the LVZ thickness in our study area from the time intervals between Ps_{L-} and Ps_{L+} phases. Figure 6.1 show radial RFs of two OBSs and two on-land stations, where the time intervals between the two phases tend to be longer at on-land stations than OBSs. We consider this reflects the increase in the thickness of LVZ with slab subduction. From Figure 6.1, we evaluated the typical time intervals are ~0.5 s beneath offshore region and ~1.0 s beneath onshore region. If we assume constant seismic velocities and dip angle of the LVZ for simplicity, the thickness of the LVZ becomes proportional to the time interval difference; the LVZ is twice as thick beneath on-land stations as beneath OBSs.

We may attribute this increasing LVZ thickness with its depth to the layered structure of the oceanic crust where a facies with lower metamorphic degree is located at its upper portion [e.g., *Christensen*, 1978]. In general, dehydration reactions due to metamorphic phase changes begin in the upper part of the oceanic crust and then gradually the location transfers to the lower part as the slab subducts. This, in turn, would lead to increase in the thickness of the LVZ. In accordance with this speculation in our study area, we conjecture that the onset of a metamorphic phase change from greenschist to epidote-amphibolite facies thickens the LVZ beneath the inland area (Figure 6.2).

Although this interpretation is based on the rough estimate, more detailed analysis using both OBS and on-land station data will allow us to understand spatial distribution of fluid from seismogenic to transition zones. Such knowledge should provide constraints on the dehydration process of the subducting plates and the rupture zones of future megathrust earthquakes.

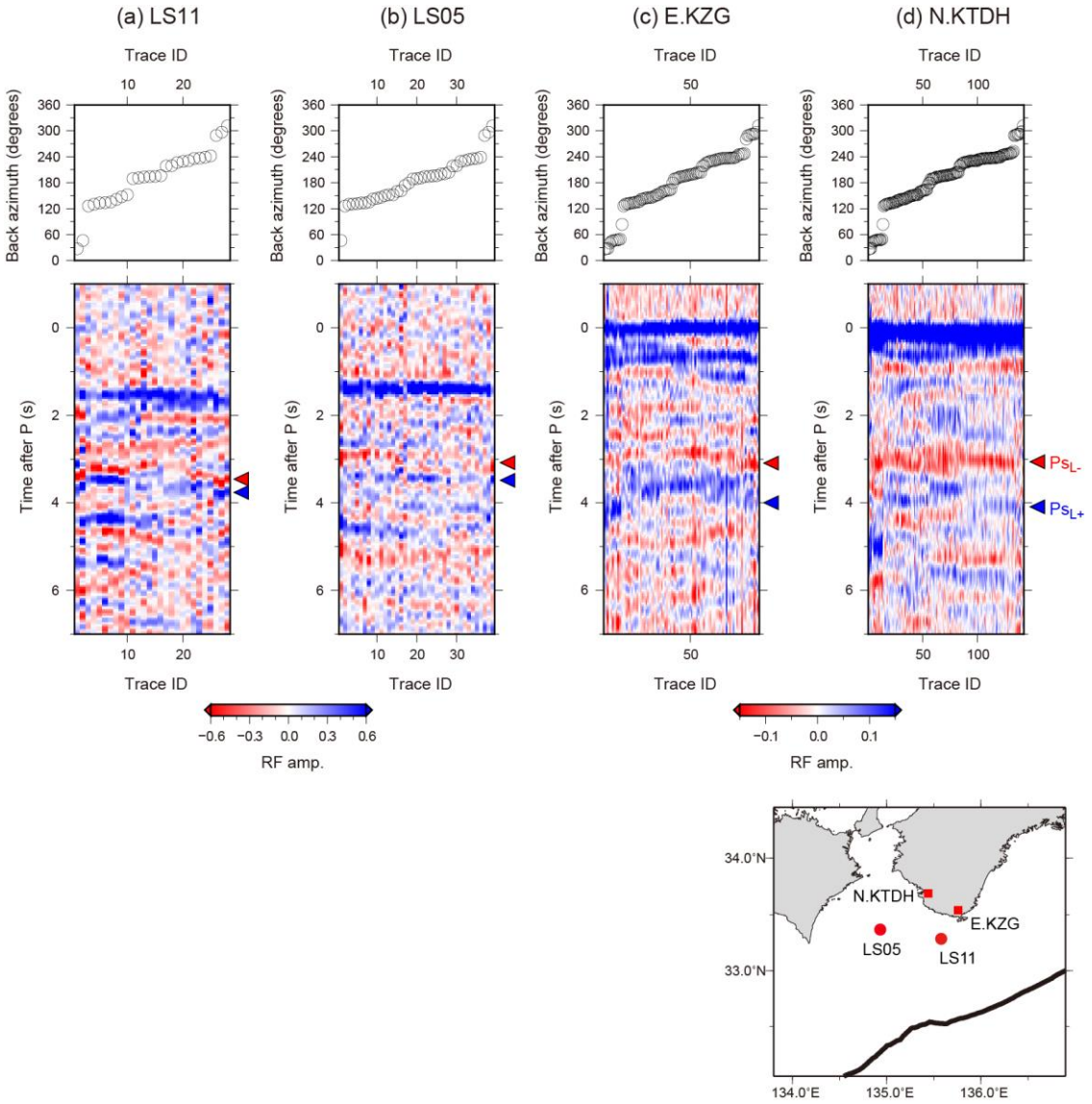

Figure 6.1. Radial receiver functions (RFs) of (a, b) ocean-bottom seismometers (OBSs) and (c, d) on-land stations plotted along their back azimuths. The notations are the same as Figure 5.2 (red and blue triangles indicate Ps_{L-} and Ps_{L+} phases, respectively). Note that time interval between Ps_{L-} and Ps_{L+} phases tend to be longer at on-land stations than OBSs. The locations of stations are shown in the bottom inset.

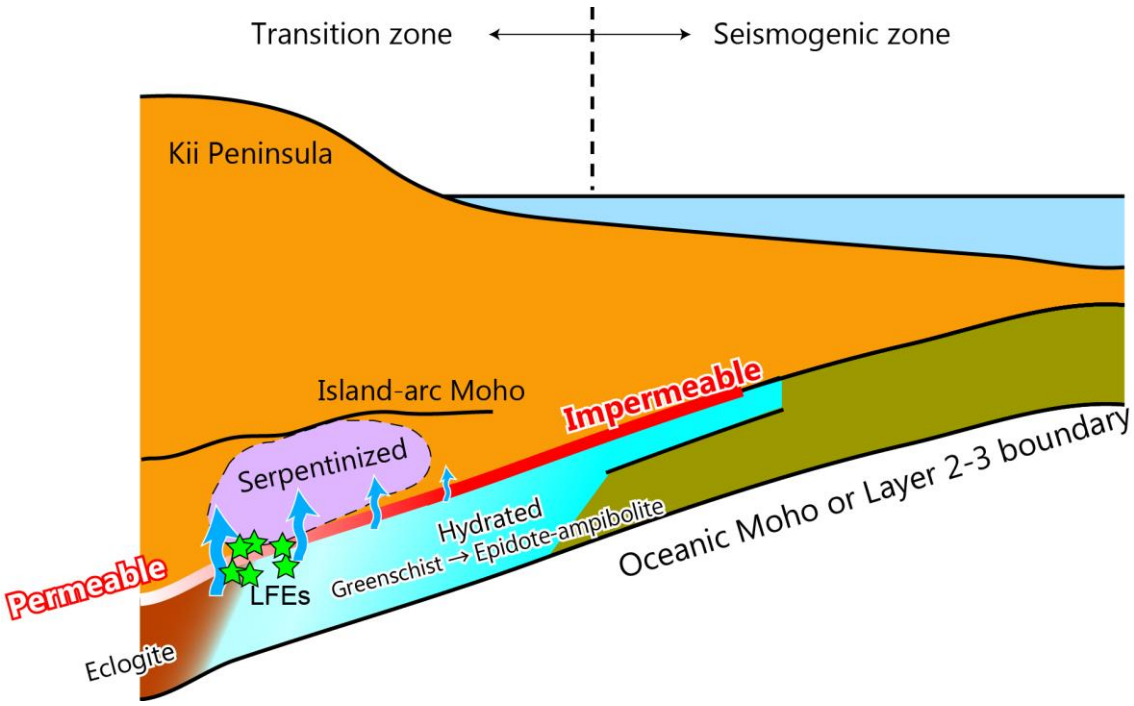

Figure 6.2. Schematic illustration of southwestern subduction zone around the Kii Peninsula with some interpretations made by this study. The sky blue color beneath the plate interface shows the area which we consider to be hydrated, namely low-velocity zone (LVZ). Difference in LVZ thicknesses beneath offshore and onshore regions reflects the difference in the time intervals between Ps_{L-} and Ps_{L+} phases (Figure 6.1).

6.2. Along-strike variation of fluid distribution

Knowledge of along-strike variation of fluid distribution is also important because it may affect rupture propagation of megathrust earthquakes. In Figure 6.3, we show the locations of the LVZ identified in Chapter 5 and high-reflectivity zones which are interpreted as fluid-rich layer along the plate interface by previous active source surveys [*Kodaira et al.*, 2002; *Park et al.*, 2014]. The region we found the LVZ is around 15-20 km depth, located at seismogenic zone depth (i.e., the rupture zone of the Nankai earthquake), spanning ~100 km in along-strike direction. The western edge of this region corresponds to the survey line of *Kodaira et al.* [2002], along which the intense P-to-P reflection phase has been detected. If we assume that the LVZs identified by our study and high-reflectivity zone by *Kodaira et al.* [2002] represent the same phenomena, the LVZ will extend over a wide area in terms of both along-dip and along-strike directions.

Our estimated P- and S-wave velocities of the LVZ indicate their maximum values at the eastern-most site, LS11 (Figure 5.10), where strong RF amplitudes are also mapped by the imaging method (Figure 4.7e). This makes the interpretation more confident that strong RF amplitude reflects fluid-rich plate interface compared with surrounding region. As stated in Section 4.3.3, this fluid-rich zone seems to extend further seaward where *Park et al.* [2014] has identified fluid-rich décollement (Figure 6.3).

We can see that the regions where we identified the LVZ and the strong RF amplitudes are complementary to the regions of large coseismic slip (> 5 m) during the 1946 Nankai earthquakes [*Murotani et al.*, 2015] (Figure 6.3). We consider that, in the LVZ and the strong RF amplitudes area, excess pore fluid pressure results in weak coupling between the subducting and overriding plates, leading to less amount of coseismic slip. Hence, the zone of high RF amplitudes might be a cause of the rupture

area boundary between the 1944 Tonankai and 1946 Nankai earthquakes. While seismogenic zones are often associated with less-fluid character compared with updip and downdip transition zones [e.g., *Saffer and Tobin*, 2011], our interpretation suggests that fluid-rich part exists in the seismogenic zone. Similar observation has been obtained in the Alaska subduction zone, where fluid-rich layer exists in the updip part of the seismogenic area [*Li et al.*, 2015]. RF inversion analysis as conducted in Chapter 5 should be applied to other global regions to understand relationship between fluid distribution and rupture area of megathrust earthquakes.

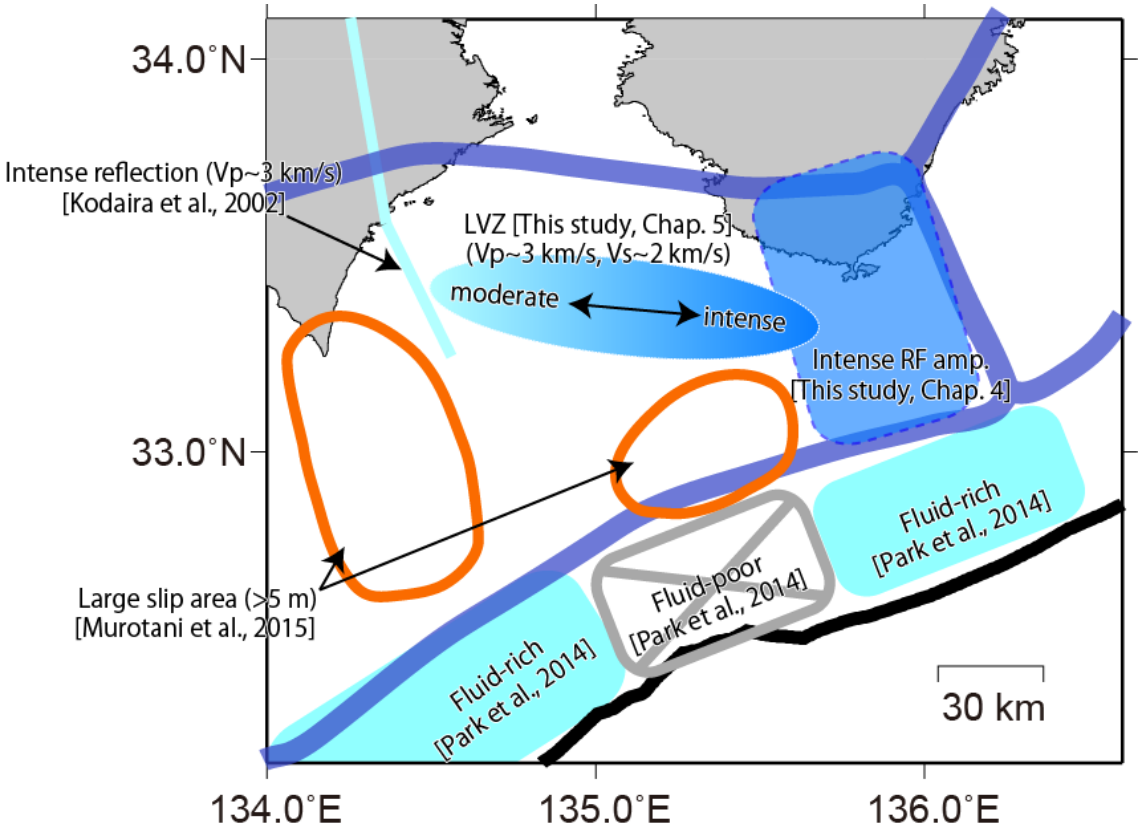

Figure 6.3. Schematic map of fluid-related features along the plate interface identified by this study and previous active source seismic surveys [*Kodaira et al.*, 2002; *Park et al.*, 2014]. Thick black line represents the Nankai Trough. Thick blue lines roughly enclose whole rupture area of the Tonankai and Nankai earthquakes [e.g., *Baba et al.*, 2002, 2006]. Orange lines enclose areas where coseismic slip larger than 5 m is estimated during the 1946 Nankai earthquake [*Murotani et al.*, 2015].

6.3. Suggestions for future studies

Comparison with other subduction zones is important to deepen our understanding. For example, in Chapter 4, we interpreted that non-volcanic tremors beneath the Kii Peninsula occur along the permeable plate interface. In fact, consistent results have been acquired in the Tokai region [*Kato et al.*, 2010] and southern Mexico [*Song et al.*, 2009], whereas the situation seems different in Cascadia where tremors are considered to occur at impermeable plate interface [*Peacock et al.*, 2011]. Such a difference should be studied in detail, which could lead to better understanding of difference in behavior of tremors among subduction zones (recurrence interval, downdip width of tremor belt, and migration pattern). The updip limit of LVZ is also different between our results (<5 km depth, inferred from Figure 4.7) and that from the Cascadia (~15 km depth; *Nedimović et al.* [2003]). Further studies are necessary because our station network cover a small area near the trench. These differences may give some implication about slip patterns of megathrust earthquakes, which is worth investigating in the future.

Another missing aspect in our analysis is anisotropic structure, which can be constrained from RFs theoretically [e.g., *Frederiksen and Bostock*, 2000; *Shiomi and Park*, 2008; *Song and Kim*, 2012]. Investigation into anisotropic structure may help understand the rheology of the shear zone [*Song and Kim*, 2012]. Additive model parameters for anisotropic structure will make inversion analysis more challenging. The usage of transverse component records and longer time windows on RFs can help solve the problem. This is worth tackling because anisotropic structure cannot be constrained from conventional active source surveys.

Nowadays, the number of passive seismic monitoring in offshore regions is increasing, not only in Japan, but also in the world. In this sense, our attempt to better analyze OBS data employing RF methods will become more useful on future studies,

using such datasets. The method we developed in this study can be applied to various data and may be further developed so that more detailed structure can be revealed (dipping angle, anisotropy, etc.).

7. Conclusion

In this thesis, we first developed a method to calculate RFs from OBS data, where water reverberations on vertical component records were efficiently removed by applying a frequency domain filter. The filter can be expressed with two parameters, two-way traveltime within the water layer and reflection coefficient on the seafloor, which we determined through waveform inversion analysis. Then, applying this method, we investigated the hydrous state of the subducting Philippine Sea plate around the Kii Peninsula, southwestern Japan.

We performed time-to-depth conversion of radial RFs to create image of the subsurface structure with the aid of a previous tomography model. We obtained 3-D geometry of the subducting plate from the image with the clue of the positive and negative phases, which we interpreted as P-to-S conversion phases from the oceanic Moho and the plate interface, respectively. We confirmed that the negative RF peaks along the plate interface extends to beneath the offshore region. We consider that these negative amplitudes imply the existence of the LVZ just beneath the plate interface.

RF amplitudes along the plate interface and the oceanic Moho gradually decrease as the slab subducts deeper beneath the Kii Peninsula. This phenomena may be explained by the dehydration reactions of the oceanic crust; eclogitization increases the seismic velocity of the oceanic crust, and accompanying densification leads to fracturing of the sealed plate interface which allows fluid to ascend into the overriding plate. An important suggestion here is that the non-volcanic tremors in this region would be characterized by the permeable plate interface. This contrasts to an established idea that a long-term SSEs occur at impermeable plate interface.

To further constrain the property of LVZ along the subducting plate, we performed RF waveform inversion including high frequency contents for several OBSs. We found that the thickness of the LVZ is extremely thin (~2 km) and its P- and S-wave

velocities are quite low (~3 km/s and ~2 km/s, respectively). We interpreted this as a fluid-rich layer located at the top of the subducting plate. The location where we identified the LVZ is in the seismogenic zone depth, but is complementary to zones with large coseismic slip during the 1944 Nankai earthquakes. The fluid-rich interface may cause weak coupling between the subducting and overriding plates. Although our analysis was limited in terms of spatial extent so far, future investigations into the spatial variations of the LVZ properties would help us better understand fluid distribution along the megathrust fault.

Acknowledgment

The first and foremost, I would like to show my greatest appreciation to Associate Professor Kimihiro Mochizuki who offered continuing support and constant encouragement throughout my PhD course. This thesis would not have been possible without his help. My thanks also go to my defense committee members: Professors Satoshi Ide, Hitoshi Kawakatsu, Masanao Shinohara, and Associate Professors Takashi Iidaka and Jin-Oh Park. In addition, Professor Hitoshi Kawakatsu gave me insightful suggestions on my research and provided a code for computing seismograms.

I owe a very important debt to Professor Dr. Takashi Tonegawa whose guidance, comments and suggestions made enormous contribution to my work. I would also like to express my gratitude to Professor Associate Professor Nozomu Takeuchi and Dr. Ryohei Iritani for providing a code of waveform inversion.

I would like to express my gratitude to Professor Takuo Shibutani and Drs. Katsuhiko Shiomi, Ayako Nakanishi, Masaru Nakano, and Yojiro Yamamoto for useful discussions about the study area. Professor Michael Bostock gives me constructive comments on this study. Advice and comments given by the member of Seismogenic-zone Physical-properties and Structure Seminar, at Earthquake Research Institute, university of Tokyo, have helped me improve this thesis. I also thank laboratory members and colleagues for their sincere support.

I appreciate Professors Masanao Shinohara, Hiroshi Shimizu, and Shin'ichi Sakai and Drs. Kazuo Nakahigashi, Toshihiko Kanazawa, and Kenji Uehira for data acquisition. I thank the Japan Meteorology Agency, National Research Institute for Earth Science and Disaster Prevention, University of Tokyo, Kochi University, and Kyoto University for providing continuous waveform data.

We used The Generic Mapping Tools [*Wessel and Smith*, 1991] for drawing figures. This thesis also makes use of the computer package NA which was made

available with support from the Inversion Laboratory (ilab). Ilab is a program for construction and distribution of data inference software in the geosciences supported by AuScope Ltd, a non-profit organization for Earth Science infrastructure funded by the Australian Federal Government. This work was supported by JSPS KAKENHI Grant Number 26-10221.

Last but not least, I would also like to express my gratitude to my family for their moral support and warm encouragements.

Appendix A. Error estimation for receiver function stacking

Multitaper correlation (MTC) method has been devised to calculate receiver functions (RFs) stably even in high frequency range [*Park and Levin*, 2000]. One of the advantages of this MTC method is the capability of estimating frequency-dependent uncertainties regarding RF estimation. These estimated uncertainties can be used as weighting factors when stacking RFs in the frequency domain, but there is no formula to convert the frequency-dependent uncertainties into the time domain. We, therefore, take the advantage of jackknife resampling method to compute time-dependent uncertainties, generally following the method of *Leahy and Collins* [2009]. We will introduce the method briefly below.

Let us assume we have N teleseimic event records to calculate RFs. Using the MTC method, we can estimate the RF and its uncertainties of the jth event in frequency domain, which are denoted by $H_j(\omega)$ and $\Delta H_j(\omega)$, repectively. Then, the stacked RFs over the N events, $H(\omega)$, is computed using weighted average:

$$H(\omega) = \sum_{j=1}^{N} \frac{H_j(\omega)}{\Delta H_j(\omega)} \left(\sum_{j=1}^{N} \frac{1}{\Delta H_j(\omega)} \right)^{-1}. \quad \text{(A1)}$$

With the inverse Fourier transformation of $H(\omega)$, we can obtain a stacked RF in the time domain,

$$h(t) = \mathcal{F}^{-1}\{H(\omega)\}, \quad \text{(A2)}$$

where $\mathcal{F}^{-1}\{\cdot\}$ represents inverse Fourier transform.

To estimate time-dependent uncertainties of the stacked RFs, we apply jackknife resampling method as follows. At first, we estimate N types of stacked RFs, $\hat{h}_{\mathrm{j}}(t)$,

from $N-1$ events by skipping the jth event:

$$\widehat{H}_j(\omega) = \sum_{k\neq j}^{N} \frac{H_k(\omega)}{\Delta H_k(\omega)} \left(\sum_{k\neq j}^{N} \frac{1}{\Delta H_k(\omega)} \right)^{-1}, \tag{A3}$$

$$\hat{h}_j(t) = \mathcal{F}^{-1}\{\widehat{H}_j(\omega)\}, \tag{A4}$$

Then, time-domain uncertainty, $\Delta h(t)$ is estimated from the N sets of RFs as follows:

$$\bar{h}(t) = \frac{1}{N}\sum_{j=1}^{N} \hat{h}_j(t)\,, \tag{A5}$$

$$\Delta h(t) = \sqrt{\frac{N-1}{N}\sum_{j=1}^{N}\{\bar{h}(t) - \hat{h}_j(t)\}^2}\,. \tag{A6}$$

The resultant uncertainties in this way is more plausible than standard error calculated in normal way, in that we can take the frequency-dependent uncertainties into consideration through Eq. (A3).

References

Abe, Y., T. Ohkura, K. Hirahara, and T. Shibutani (2013), Along-arc variation in water distribution in the uppermost mantle beneath Kyushu, Japan, as derived from receiver function analyses, *J. Geophys. Res. Solid Earth*, *118*(7), 3540–3556, doi:10.1002/jgrb.50257.

Abers, G. A., J. Nakajima, P. E. van Keken, S. Kita, and B. R. Hacker (2013), Thermal–petrological controls on the location of earthquakes within subducting plates, *Earth Planet. Sci. Lett.*, *369-370*, 178–187, doi:10.1016/j.epsl.2013.03.022.

Abt, D. L., K. M. Fischer, S. W. French, H. A. Ford, H. Yuan, and B. Romanowicz (2010), North American lithospheric discontinuity structure imaged by Ps and Sp receiver functions, *J. Geophys. Res.*, *115*(B9), B09301, doi:10.1029/2009JB006914.

Akuhara, T., and K. Mochizuki (2014), Application of cluster analysis based on waveform cross-correlation coefficients to data recorded by ocean-bottom seismometers: results from off the Kii Peninsula, *Earth, Planets Sp.*, *66*(1), 80, doi:10.1186/1880-5981-66-80.

Akuhara, T., K. Mochizuki, K. Nakahigashi, T. Yamada, M. Shinohara, S. Sakai, T. Kanazawa, K. Uehira, and H. Shimizu (2013), Segmentation of the Vp/Vs ratio and low-frequency earthquake distribution around the fault boundary of the Tonankai and Nankai earthquakes, *Geophys. Res. Lett.*, *40*(7), 1306–1310, doi:10.1002/grl.50223.

Ammon, C. J., G. E. Randall, and G. Zandt (1990), On the nonuniqueness of receiver function inversions, *J. Geophys. Res.*, *95*(B10), 15303, doi:10.1029/JB095iB10p15303.

Ando, M. (1975), Source mechanisms and tectonic significance of historical earthquakes along the nankai trough, Japan, *Tectonophysics*, *27*(2), 119–140, doi:10.1016/0040-1951(75)90102-X.

Audet, P., and S. Y. Schwartz (2013), Hydrologic control of forearc strength and seismicity in the Costa Rican subduction zone, *Nat. Geosci.*, *6*(10), 852–855, doi:10.1038/ngeo1927.

Audet, P., M. G. Bostock, N. I. Christensen, and S. M. Peacock (2009), Seismic evidence for overpressured subducted oceanic crust and megathrust fault sealing, *Nature*, *457*(7225), 76–78, doi:10.1038/nature07650.

Baba, T., Y. Tanioka, P. R. Cummins, and K. Uhira (2002), The slip distribution of the 1946 Nankai earthquake estimated from tsunami inversion using a new plate model, *Phys. Earth Planet. Inter.*, *132*(1-3), 59–73, doi:10.1016/S0031-9201(02)00044-4.

Baba, T., P. R. Cummins, T. Hori, and Y. Kaneda (2006), High precision slip distribution of the 1944 Tonankai earthquake inferred from tsunami waveforms: Possible slip on a splay fault, *Tectonophysics*, *426*(1-2), 119–134, doi:10.1016/j.tecto.2006.02.015.

Backus, M. M. (1959), WATER REVERBERATIONS—THEIR NATURE AND ELIMINATION, *Geophysics*, *24*(2), 233–261, doi:10.1190/1.1438579.

Baker, G. E., and J. L. Stevens (2004), Backazimuth estimation reliability using surface wave polarization, *Geophys. Res. Lett.*, *31*(9), L09611, doi:10.1029/2004GL019510.

Bangs, N. L. B., G. F. Moore, S. P. S. Gulick, E. M. Pangborn, H. J. Tobin, S. Kuramoto, and A. Taira (2009), Broad, weak regions of the Nankai Megathrust and implications for shallow coseismic slip, *Earth Planet. Sci. Lett.*, *284*(1-2), 44–49, doi:10.1016/j.epsl.2009.04.026.

Bell, R., R. Sutherland, D. H. N. Barker, S. Henrys, S. Bannister, L. Wallace, and J. Beavan (2010), Seismic reflection character of the Hikurangi subduction interface, New Zealand, in the region of repeated Gisborne slow slip events, *Geophys. J. Int.*, *180*(1), 34–48, doi:10.1111/j.1365-246X.2009.04401.x.

Birch, F. (1961), The velocity of compressional waves in rocks to 10 kilobars: 2., *J. Geophys. Res.*, *66*(7), 2199–2224, doi:10.1029/JZ066i007p02199.

Bostock, M. G. (2013), The Moho in subduction zones, *Tectonophysics, 609*, 547–557, doi:10.1016/j.tecto.2012.07.007.

Bostock, M. G., and A. M. Trehu (2012), Wave-Field Decomposition of Ocean Bottom Seismograms, *Bull. Seismol. Soc. Am.*, *102*(4), 1681–1692, doi:10.1785/0120110162.

Calahorrano, A., V. Sallarès, J. Y. Collot, F. Sage, and C. R. Ranero (2008), Nonlinear variations of the physical properties along the southern Ecuador subduction channel: Results from depth-migrated seismic data, *Earth Planet. Sci. Lett.*, *267*(3-4), 453–467, doi:10.1016/j.epsl.2007.11.061.

Chevrot, S. (2002), Optimal measurement of relative and absolute delay times by simulated annealing, *Geophys. J. Int.*, *151*(1), 164–171, doi:10.1046/j.1365-246X.2002.01755.x.

Christensen, N. I. (1978), Ophiolites, seismic velocities and oceanic crustal structure, *Tectonophysics*, *47*(1-2), 131–157, doi:10.1016/0040-1951(78)90155-5.

Christensen, N. I. (1984), Pore pressure and oceanic crustal seismic structure, *Geophys. J. Int.*, *79*(2), 411–423, doi:10.1111/j.1365-246X.1984.tb02232.x.

Christensen, N. I. (1996), Poisson's ratio and crustal seismology, *J. Geophys. Res.*, *101*(B2), 3139–3156, doi:10.1029/95JB03446.

Christensen, N. I. (2004), Serpentinites, Peridotites, and Seismology, *Int. Geol. Rev.*, *46*(9), 795–816, doi:10.2747/0020-6814.46.9.795.

Christensen, N. I., and M. H. Salisbury (1975), Structure and constitution of the lower oceanic crust, *Rev. Geophys.*, *13*(1), 57–86, doi:10.1029/RG013i001p00057.

Clayton, R. W., and R. A. Wiggins (1976), Source shape estimation and deconvolution of teleseismic bodywaves, *Geophys. J. Int.*, *47*(1), 151–177, doi:10.1111/j.1365-246X.1976.tb01267.x.

Dueker, K. G., and A. F. Sheehan (1997), Mantle discontinuity structure from midpoint stacks of converted P to S waves across the Yellowstone hotspot track, *J. Geophys. Res.*, *102*(B4), 8313–8327, doi:10.1029/96JB03857.

Fagereng, Å., and J. F. A. Diener (2011), Non-volcanic tremor and discontinuous slab dehydration, *Geophys. Res. Lett.*, *38*(15), L15302, doi:10.1029/2011GL048214.

Frederiksen, a. W., and M. G. Bostock (2000), Modelling teleseismic waves in dipping anisotropic structures, *Geophys. J. Int.*, *141*(2), 401–412, doi:10.1046/j.1365-246x.2000.00090.x.

Hacker, B. R. (2003), Subduction factory 2. Are intermediate-depth earthquakes in subducting slabs linked to metamorphic dehydration reactions?, *J. Geophys. Res.*, *108*(B1), 2030, doi:10.1029/2001JB001129.

Hamilton, E. L. (1978), Sound velocity–density relations in sea-floor sediments and rocks, *J. Acoust. Soc. Am.*, *63*(2), 366–377, doi:10.1121/1.381747.

Hamilton, E. L. (1979), Vp/Vs and Poisson's ratios in marine sediments and rocks, *J. Acoust. Soc. Am.*, *66*(4), 1093–1101, doi:10.1121/1.383344.

Hansen, R. T. J., M. G. Bostock, and N. I. Christensen (2012), Nature of the low velocity zone in Cascadia from receiver function waveform inversion, *Earth Planet. Sci. Lett.*, *337-338*, 25–38, doi:10.1016/j.epsl.2012.05.031.

Haskell, N. A. (1953), The dispersion of surface waves on multilayered media, *Bull. Seismol. Soc. Am.*, *43*(1), 17–34.

Hirose, F., J. Nakajima, and A. Hasegawa (2008), Three-dimensional seismic velocity structure and configuration of the Philippine Sea slab in southwestern Japan estimated by double-difference tomography, *J. Geophys. Res.*, *113*(B9), B09315, doi:10.1029/2007JB005274.

Hoffman, N. W., and H. J. Tobin (2004), An empirical relationship between velocity and porosity for underthrust sediments in the Nankai Trough accretionary prism, in *Proceedings of the Ocean Drilling Program, Scientific Results*, vol. 190/196, pp. 1–23.

Husen, S., and E. Kissling (2001), Postseismic fluid flow after the large subduction earthquake of Antofagasta, Chile, *Geology*, *29*(9), 847–850, doi:10.1130/0091-7613(2001)029<0847:PFFATL>2.0.CO;2.

Hyndman, R. D., and S. M. Peacock (2003), Serpentinization of the forearc mantle, *Earth Planet. Sci. Lett.*, *212*(3-4), 417–432, doi:10.1016/S0012-821X(03)00263-2.

Ide, S., K. Shiomi, K. Mochizuki, T. Tonegawa, and G. Kimura (2010), Split Philippine Sea plate beneath Japan, *Geophys. Res. Lett.*, *37*(21), L21304, doi:10.1029/2010GL044585.

Idehara, K., S. Yabe, and S. Ide (2014), Regional and global variations in the temporal clustering of tectonic tremor activity, *Earth, Planets Sp.*, *66*(1), 66, doi:10.1186/1880-5981-66-66.

Iritani, R., N. Takeuchi, and H. Kawakatsu (2010), Seismic attenuation structure of the top half of the inner core beneath the northeastern Pacific, *Geophys. Res. Lett.*, *37*(19), L19303, doi:10.1029/2010GL044053.

Iritani, R., N. Takeuchi, and H. Kawakatsu (2014), Intricate heterogeneous structures of the top 300 km of the Earth's inner core inferred from global array data: I. Regional 1D attenuation and velocity profiles, *Phys. Earth Planet. Inter.*, *230*, 15–27, doi:10.1016/j.pepi.2014.02.002.

Ishise, M., K. Koketsu, and H. Miyake (2009), Slab segmentation revealed by anisotropic P‐wave tomography, *Geophys. Res. Lett.*, *36*, doi:10.1029/2009GL037749.

Julià, J. (2007), Constraining velocity and density contrasts across the crust-mantle boundary with receiver function amplitudes, *Geophys. J. Int.*, *171*(1), 286–301, doi:10.1111/j.1365-2966.2007.03502.x.

Kamei, R., R. G. Pratt, and T. Tsuji (2012), Waveform tomography imaging of a megasplay fault system in the seismogenic Nankai subduction zone, *Earth Planet. Sci. Lett.*, *317-318*, 343–353, doi:10.1016/j.epsl.2011.10.042.

Kato, A. et al. (2010), Variations of fluid pressure within the subducting oceanic crust and slow earthquakes, *Geophys. Res. Lett.*, *37*(14), L14310, doi:10.1029/2010GL043723.

Kato, A., A. Saiga, T. Takeda, T. Iwasaki, and T. Matsuzawa (2014), Non-volcanic seismic swarm and fluid transportation driven by subduction of the Philippine Sea slab beneath the Kii Peninsula, Japan, *Earth, Planets Sp.*, *66*(1), 86, doi:10.1186/1880-5981-66-86.

Kawakatsu, H., and S. Watada (2007), Seismic evidence for deep-water transportation in the mantle., *Science (80-.).*, *316*, 1468–1471, doi:10.1126/science.1140855.

Kennett, B. L. N., and E. R. Engdahl (1991), Traveltimes for global earthquake location and phase identification, *Geophys. J. Int.*, *105*(2), 429–465, doi:10.1111/j.1365-246X.1991.tb06724.x.

Kim, Y., and R. W. Clayton (2015), Seismic properties of the Nazca oceanic crust in southern Peruvian subduction system, *Earth Planet. Sci. Lett.*, *429*, 110–121, doi:10.1016/j.epsl.2015.07.055.

Kim, Y., R. W. Clayton, and J. M. Jackson (2010), Geometry and seismic properties of the subducting Cocos plate in central Mexico, *J. Geophys. Res.*, *115*(B6), B06310, doi:10.1029/2009JB006942.

Kimura, G., S. Hina, Y. Hamada, J. Kameda, T. Tsuji, M. Kinoshita, and A. Yamaguchi (2012), Runaway slip to the trench due to rupture of highly pressurized megathrust beneath the middle trench slope: The tsunamigenesis of the 2011 Tohoku earthquake off the east coast of northern Japan, *Earth Planet. Sci. Lett.*, *339-340*, 32–45, doi:10.1016/j.epsl.2012.04.002.

Kirkpatrick, S., C. D. Gelatt, and M. P. Vecchi (1983), Optimization by Simulated Annealing, *Science (80-.).*, *220*(4598), 671–680, doi:10.1126/science.220.4598.671.

Kobayashi, A. (2014), A long-term slow slip event from 1996 to 1997 in the Kii Channel, Japan, *Earth, Planets Sp.*, *66*(1), 9, doi:10.1186/1880-5981-66-9.

Kodaira, S., N. Takahashi, A. Nakanishi, S. Miura, and Y. Kaneda (2000), Subducted Seamount Imaged in the Rupture Zone of the 1946 Nankaido Earthquake, *Science (80-.).*, *289*, 104–106, doi:10.1126/science.289.5476.104.

Kodaira, S., E. Kurashimo, J.-O. Park, N. Takahashi, A. Nakanishi, S. Miura, T. Iwasaki, N. Hirata, K. Ito, and Y. Kaneda (2002), Structural factors controlling the rupture process of a megathrust earthquake at the Nankai trough seismogenic zone, *Geophys. J. Int.*, *149*(3), 815–835, doi:10.1046/j.1365-246X.2002.01691.x.

Kodaira, S., T. Iidaka, A. Kato, J.-O. Park, T. Iwasaki, and Y. Kaneda (2004), High pore fluid pressure may cause silent slip in the Nankai Trough., *Science*, *304*, 1295–1298, doi:10.1126/science.1096535.

Kodaira, S., T. Hori, A. Ito, S. Miura, G. Fujie, J.-O. Park, T. Baba, H. Sakaguchi, and Y. Kaneda (2006), A cause of rupture segmentation and synchronization in the Nankai trough revealed by seismic imaging and numerical simulation, *J. Geophys. Res.*, *111*(B9), B09301, doi:10.1029/2005JB004030.

Kumar, P., H. Kawakatsu, M. Shinohara, T. Kanazawa, E. Araki, and K. Suyehiro (2011), P and S receiver function analysis of seafloor borehole broadband seismic data, *J. Geophys. Res.*, *116*(B12), B12308, doi:10.1029/2011JB008506.

Kurashimo, E. et al. (2013), Along-strike structural changes controlled by dehydration-related fluids within the Philippine Sea plate around the segment boundary of a megathrust earthquake beneath the Kii peninsula, southwest Japan, *Geophys. Res. Lett.*, *40*(18), 4839–4844, doi:10.1002/grl.50939.

Kuwatani, T., A. Okamoto, and M. Toriumi (2011), Thermodynamic forward modeling of progressive dehydration reactions during subduction of oceanic crust under greenschist facies conditions, *Earth Planet. Sci. Lett.*, *307*(1-2), 9–18, doi:10.1016/j.epsl.2011.01.027.

Leahy, G. M., and J. A. Collins (2009), Improved Statistical Processing for Common-Conversion-Point Stacked Receiver Functions, *Bull. Seismol. Soc. Am.*, *99*(2A), 914–921, doi:10.1785/0120080263.

Li, J., D. J. Shillington, A. Bécel, M. R. Nedimović, S. C. Webb, D. M. Saffer, K. M. Keranen, and H. Kuehn (2015), Downdip variations in seismic reflection character: Implications for fault structure and seismogenic behavior in the Alaska subduction zone, *J. Geophys. Res. Solid Earth*, *120*(11), 7883–7904, doi:10.1002/2015JB012338.

Matsubara, M., K. Obara, and K. Kasahara (2008), Three-dimensional P- and S-wave velocity structures beneath the Japan Islands obtained by high-density seismic stations by seismic tomography, *Tectonophysics*, *454*(1-4), 86–103, doi:10.1016/j.tecto.2008.04.016.

Miyazaki, S., and K. Heki (2001), Crustal velocity field of southwest Japan: Subduction and arc-arc collision, *J. Geophys. Res.*, *106*(B3), 4305–4326, doi:10.1029/2000JB900312.

Mochizuki, K., G. Fujie, T. Sato, J. Kasahara, R. Hino, M. Shinohara, and K. Suyehiro (1998), Heterogeneous crustal structure across a seismic block boundary along the Nankai Trough, *Geophys. Res. Lett.*, *25*(13), 2301–2304, doi:10.1029/98GL51867.

Mochizuki, K. et al. (2005), Intense PP reflection beneath the aseismic forearc slope of the Japan Trench subduction zone and its implication of aseismic slip subduction, *J. Geophys. Res.*, *110*(B1), B01302, doi:10.1029/2003JB002892.

Mochizuki, K., K. Nakahigashi, A. Kuwano, T. Yamada, M. Shinohara, S. Sakai, T. Kanazawa, K. Uehira, and H. Shimizu (2010), Seismic characteristics around the fault segment boundary of historical great earthquakes along the Nankai Trough revealed by repeated long-term OBS observations, *Geophys. Res. Lett.*, *37*(9), L09304, doi:10.1029/2010GL042935.

Moore, G. F. et al. (2009), Structural and seismic stratigraphic framework of the NanTroSEIZE Stage 1 transect, in *Proceedings of the Integrated Ocean Drilling Program*, vol. 314/315/31, Integrated Ocean Drilling Program Management International, Inc., Washington, DC.

Murotani, S., K. Shimazaki, and K. Koketsu (2015), Rupture process of the 1946 Nankai earthquake estimated using seismic waveforms and geodetic data, *J. Geophys. Res. Solid Earth*, *120*(8), 5677–5692, doi:10.1002/2014JB011676.

Nedimović, M. R., R. D. Hyndman, K. Ramachandran, and G. D. Spence (2003), Reflection signature of seismic and aseismic slip on the northern Cascadia subduction interface, *Nature*, *424*(6947), 416–420, doi:10.1038/nature01840.

Obara, K., H. Hirose, F. Yamamizu, and K. Kasahara (2004), Episodic slow slip events accompanied by non-volcanic tremors in southwest Japan subduction zone, *Geophys. Res. Lett.*, *31*(23), L23602, doi:10.1029/2004GL020848.

Okino, K., Y. Ohara, S. Kasuga, and Y. Kato (1999), The Philippine Sea: New survey results reveal the structure and the history of the marginal basins, *Geophys. Res. Lett.*, *26*(15), 2287–2290, doi:10.1029/1999GL900537.

Park, J., and V. Levin (2000), Receiver Functions from Multiple-Taper Spectral Correlation Estimates, *Bull. Seismol. Soc. Am.*, *90*(6), 1507–1520, doi:10.1785/0119990122.

Park, J.-O., H. Naruse, and N. L. Bangs (2014), Along-strike variations in the Nankai shallow décollement properties and their implications for tsunami earthquake generation, *Geophys. Res. Lett.*, *41*(20), 7057-7064, doi:10.1002/2014GL061096.

Peacock, S. M. (1993), The importance of blueschist → eclogite dehydration reactions in subducting oceanic crust, *Geol. Soc. Am. Bull.*, *105*(5), 684–694, doi:10.1130/0016-7606(1993)105<0684:TIOBED>2.3.CO;2.

Peacock, S. M., and K. Wang (1999), Seismic Consequences of Warm Versus Cool Subduction Metamorphism: Examples from Southwest and Northeast Japan, *Science (80-.).*, *286*, 937–939, doi:10.1126/science.286.5441.937.

Peacock, S. M., N. I. Christensen, M. G. Bostock, and P. Audet (2011), High pore pressures and porosity at 35 km depth in the Cascadia subduction zone, *Geology*, *39*(5), 471–474, doi:10.1130/G31649.1.

Reyners, M., and D. Eberhart-Phillips (2009), Small earthquakes provide insight into plate coupling and fluid distribution in the Hikurangi subduction zone, New Zealand, *Earth Planet. Sci. Lett.*, *282*(1-4), 299–305, doi:10.1016/j.epsl.2009.03.034.

Saffer, D. M., and H. J. Tobin (2011), Hydrogeology and Mechanics of Subduction Zone Forearcs: Fluid Flow and Pore Pressure, *Annu. Rev. Earth Planet. Sci.*, *39*(1), 157–186, doi:10.1146/annurev-earth-040610-133408.

Sambridge, M. (1999), Geophysical inversion with a neighbourhood algorithm-I. Searching a parameter space, *Geophys. J. Int.*, *138*(2), 479–494, doi:10.1046/j.1365-246X.1999.00876.x.

Schoenberg, M. (1980), Elastic wave behavior across linear slip interfaces, *J. Acoust. Soc. Am.*, *68*(5), 1516–1521, doi:10.1121/1.385077.

Scholz, C. (1998), Earthquakes and friction laws, *Nature*, *391*, 37–42, doi:10.1038/34097.

Screaton, E., D. Saffer, P. Henry, and S. Hunze (2002), Porosity loss within the underthrust sediments of the Nankai accretionary complex: Implications for overpressures, *Geology*, *30*(1), 19–22, doi:10.1130/0091-7613(2002)030<0019:PLWTUS>2.0.CO;2.

Shelly, D. R., G. C. Beroza, S. Ide, and S. Nakamula (2006), Low-frequency earthquakes in Shikoku, Japan, and their relationship to episodic tremor and slip., *Nature*, *442*, 188–191, doi:10.1038/nature04931.

Shelly, D. R., G. C. Beroza, and S. Ide (2007), Non-volcanic tremor and low-frequency earthquake swarms., *Nature*, *446*(7133), 305–307, doi:10.1038/nature05666.

Shibutani, T., T. Ueno, and K. Hirahara (2008), Improvement in the Extended-Time Multitaper Receiver Function Estimation Technique, *Bull. Seismol. Soc. Am.*, *98*(2), 812–816, doi:10.1785/0120070226.

Shiomi, K., and J. Park (2008), Structural features of the subducting slab beneath the Kii Peninsula, central Japan: Seismic evidence of slab segmentation, dehydration, and anisotropy, *J. Geophys. Res.*, *113*(B10), B10318, doi:10.1029/2007JB005535.

Shiomi, K., H. Sato, K. Obara, and M. Ohtake (2004), Configuration of subducting Philippine Sea plate beneath southwest Japan revealed from receiver function

analysis based on the multivariate autoregressive model, *J. Geophys. Res.*, *109*(B4), B04308, doi:10.1029/2003JB002774.

Shiomi, K., M. Matsubara, Y. Ito, and K. Obara (2008), Simple relationship between seismic activity along Philippine Sea slab and geometry of oceanic Moho beneath southwest Japan, *Geophys. J. Int.*, *173*(3), 1018–1029, doi:10.1111/j.1365-246X.2008.03786.x.

Sibson, R. H. (2013), Stress switching in subduction forearcs: Implications for overpressure containment and strength cycling on megathrusts, *Tectonophysics*, *600*, 142–152, doi:10.1016/j.tecto.2013.02.035.

Skarbek, R. M., and D. M. Saffer (2009), Pore pressure development beneath the décollement at the Nankai subduction zone: Implications for plate boundary fault strength and sediment dewatering, *J. Geophys. Res. Solid Earth*, *114*(7), B07401, doi:10.1029/2008JB006205.

Smith, W. H. F., and P. Wessel (1990), Gridding with continuous curvature splines in tension, *Geophysics*, *55*(3), 293–305, doi:10.1190/1.1442837.

Song, T. A., and D. V. Helmberger (2007), Validating tomographic model with broad-band waveform modelling: an example from the LA RISTRA transect in the southwestern United States, *Geophys. J. Int.*, *171*(1), 244–258, doi:10.1111/j.1365-246X.2007.03508.x.

Song, T. A., and Y. Kim (2012), Localized seismic anisotropy associated with long-term slow-slip events beneath southern Mexico, *Geophys. Res. Lett.*, *39*(9), L09308, doi:10.1029/2012GL051324.

Song, T. A., D. V. Helmberger, M. R. Brudzinski, R. W. Clayton, P. Davis, X. Perez-Campos, and S. K. Singh (2009), Subducting slab ultra-slow velocity layer coincident with silent earthquakes in southern Mexico, *Science (80-.).*, *330*(5926), 502–506, doi:10.1126/science.1167595.

Thorwart, M., and T. Dahm (2005), Wavefield decomposition for passive ocean bottom seismological data, *Geophys. J. Int.*, *163*(2), 611–621, doi:10.1111/j.1365-246X.2005.02761.x.

Tonegawa, T., R. Iritani, and H. Kawakatsu (2013), Extraction of Moho-Generated phases from vertical and radial receiver functions of a seismic array, *Bull. Seismol. Soc. Am.*, *103*(3), 2011–2024, doi:10.1785/0120120295.

Tsuji, T., R. Kamei, and R. G. Pratt (2014), Pore pressure distribution of a mega-splay fault system in the Nankai Trough subduction zone: Insight into up-dip extent of the seismogenic zone, *Earth Planet. Sci. Lett.*, *396*, 165–178, doi:10.1016/j.epsl.2014.04.011.

Tsuji, T., J. Ashi, M. Strasser, and G. Kimura (2015), Identification of the static backstop and its influence on the evolution of the accretionary prism in the Nankai Trough, *Earth Planet. Sci. Lett.*, *431*, 15–25, doi:10.1016/j.epsl.2015.09.011.

Tsuji, Y., J. Nakajima, and A. Hasegawa (2008), Tomographic evidence for hydrated oceanic crust of the Pacific slab beneath northeastern Japan: Implications for water transportation in subduction zones, *Geophys. Res. Lett.*, *35*(14), L14308, doi:10.1029/2008GL034461.

Yamasaki, T., and T. Seno (2003), Double seismic zone and dehydration embrittlement of the subducting slab, *J. Geophys. Res.*, *108*(B4), 2212, doi:10.1029/2002JB001918.

Zhao, D., Z. Huang, N. Umino, A. Hasegawa, and H. Kanamori (2011), Structural heterogeneity in the megathrust zone and mechanism of the 2011 Tohoku-oki earthquake (Mw 9.0), *Geophys. Res. Lett.*, *38*(17), L17308, doi:10.1029/2011GL048408.

Zhu, L., and H. Kanamori (2000), Moho depth variation in southern California from teleseismic receiver functions, *J. Geophys. Res.*, *105*(B2), 2969–2980, doi:10.1029/1999JB900322.